Evidence for the Continental Origin of Pliocene Sediments in the Central Baja California Peninsula, Mexico, and the Geometric Classification of Tidal, Fluvial, and Relict Channels Using a Trained Random Forest Classifier

by

Kevin Kortum Gardner

A dissertation accepted and approved in partial fulfillment of the

requirements for the degree of

Doctor of Philosophy

in Earth Sciences

Dissertation Committee:

Rebecca J. Dorsey, Chair/Advisor

Joshua Roering, Core Member

Leif Karlstrom, Core Member

Mark Fonstad, Institutional Representative

University of Oregon

Winter 2026

DISSERTATION ABSTRACT

Kevin Kortum Gardner

Doctor of Philosophy in Earth Science

Title: Evidence for the Continental Origin of the Pliocene Sediments in the Central Baja California Peninsula, Mexico, and the Geometric Classification of Tidal, Fluvial, and Relict Channels Using a Trained Random Forest Classifier

The co-evolution of earth's topography, depositional environments, and tectonics and the genetics of terrestrial plants and animals over the past 6 million years is poorly understood, particularly in the Baja California peninsula where genetic divergence within present-day species produces northern and southern populations, for which a trans-peninsular seaway has been hypothesized. Similarly, uplifted relict tidal channels have enormous potential for use as paleo-sea level indicators, potentially providing valuable constraints on changes in sea level, which impact both the evolution of earth's surface and terrestrial organisms. However, there are no methods of determining the origin of relict channels based on their planform geometries, as studies of modern tidal and fluvial channels have revealed remarkable similarities in their evolution and geometry despite forming under vastly different flow conditions. In this dissertation, I address these gaps in our understanding through a stratigraphic, paleopedological, ichnological study of Pliocene sediments in the central Baja California Peninsula and geomorphic studies of a global dataset of tidal, fluvial, and relict channels. The first portion of this work is focused on testing the trans-peninsular seaway hypothesis for genetic divergence along the Baja California Peninsula. Analyses of the depositional environments, paleosols, and trace fossils of the Pliocene San Regis beds, alongside existing work on younger and older stratigraphy, reveal long-lived terrestrial conditions in the mid-peninsular region that preclude a marine setting, and refute the trans-peninsular seaway hypothesis for the observed genetic divergence. The next chapter focuses on the classification of modern tidal and fluvial channel planforms, a necessary step for classifying relict channels observed in Baja California Sur and elsewhere. I compiled datasets of 103 modern tidal and fluvial channels and tested the efficacy of three machine learning classifiers across 69 trials of 23 metric configurations and data scaling methods. The results reveal that a random forest classifier applied to subdivisions of channel reaches

is capable of reliably classifying all tested modern tidal and fluvial channels using the relationship between local channel width and local radius of curvature. The analysis also reveals that the relationship between radius of curvature and width in tidal channels is much simpler than in fluvial channels. In the following chapter, the geometric analysis shifts from modern channels to relict channels and their potential for use as paleo-sea level indicators. I compiled a dataset of 14 relict channels that include both channels of unknown/potentially tidal origin and those with a likely fluvial origin. I then classified their planforms using the trained random forest classifier from the previous study. The results indicate that relict channels that were considered likely fluvial were classified as fluvial alongside one relict channel of unknown origin. 8 channels that were considered unknown/potentially tidal were classified as tidal, with varying degrees of confidence. Analysis of probability scores of relict channels and mixed-energy channels reveals that four of the 14 relict channels had distributions that suggested borderline tidal/fluvial geometries that stem from natural non-uniqueness between channel types, mixed-energy origins, post-abandonment hillslope processes, or channels forming in one domain and being later modified in another. These three chapters present a comprehensive investigation into the geologic drivers of genetic differentiation in the Baja California Peninsula, and the potential for relict surface features to be used as constraints for depositional environments and changes in relative sea level. The results suggest changes in climate or habitat quality and quantity are the likely drivers of genetic differentiation, provide insight into the differences between tidal and fluvial channels, and present a novel method of using relict channels as paleo-sea level indicators.

This chapter includes previously published, in review, and unpublished co-authored material, with electronic data tables, code, and trained classifier the supplemental files.

CURRICULUM VITAE

NAME OF AUTHOR: Kevin Kortum Gardner

GRADUATE AND UNDERGRADUATE SCHOOLS ATTENDED:

University of Oregon, Eugene, OR

Whitman College, Walla Walla, WA

DEGREES AWARDED:

Doctor of Philosophy, Earth Science, 2026, University of Oregon

Master of Science, Earth Science, 2019, University of Oregon

Bachelor of Arts, Geology, 2016, Whitman College

AREAS OF SPECIAL INTEREST:

Sedimentology and Stratigraphy

Surface Processes

Fluvial Geomorphology

Tidal Geomorphology

PROFESSIONAL EXPERIENCE:

Graduate Employee, University of Oregon, 2017-2026

Research Assistant and Teaching Assistant

GRANTS, AWARDS, AND HONORS:

Graduate Student Research Award, University of Oregon, 2025

Early Career Researcher Award, 10th International Congress of Tidal Sedimentology, 2022

Outstanding Teaching Assistant Award, University of Oregon, 2019

Graduate Student Research Grant, Geological Society of America, 2018

Dr. Albert Ripley Leeds Memorial Prize for Excellence in Geology, Whitman College, 2016

PUBLICATIONS:

In Preparation	**Gardner, K.K.,** Dorsey R.J., Identification of relict channels using a trained random forest classifier. *Earth Surface Process and Landforms*

In Review **Gardner, K.K.**, Hasiotis, S.T., Dorsey, R.J., Darin, M., Bennett, S.E.K., Heizler, M., Dolby, G.A., Hausback, B. Evidence for continental origin of Pliocene sediments in central Baja California Peninsula, Mexico and implications for controls on biodiversity. *Sedimentology*

2025 **Gardner, K. K.,** & Dorsey, R. J. (2025). Planform geometric classification of fluvial and tidal channels via machine learning. *Earth Surface Processes and Landforms*, *50*(4). e70010 https://doi.org/10.1002/ESP.70010

2021 **Gardner, K.K.,** & Dorsey, R. J. (2021). Mixed carbonate–siliciclastic sedimentation at the margin of a late Miocene tidal strait, lower Colorado River Valley, south-western USA. *Sedimentology,* 63, pp. 1893-1922. https://doi.org/10.1111/sed.12834

2021 Dorsey, R.J., O'Connell, B., **Gardner, K.K.**, Homan, M.B., Bennett, S.E., Thacker, J.O. and Darin, M.H., 2021. Tectonostratigraphic record of late Miocene–early Pliocene transtensional faulting in the Eastern California shear zone, southwestern USA. *Geosphere*, *17*(4), pp.1101-1125 https://doi.org/10.1130/GES02337.1

ACKNOWLEDGMENTS

Since my first geology class at Whitman College in 2013, I have developed a passion for learning about the Earth, and for working towards answering the many questions about our home that remain unresolved. In August 2017, I moved to Eugene to begin my master's degree at the University of Oregon. Now, in March 2026, I find myself at the finish line looking back at where I started and seeing the sinuous path that has brought me here. Although this marathon is my own, it would not be possible to be here without a community of people who have made this all possible, to whom I owe endless gratitude.

First and foremost, I would like to thank my advisor, Becky Dorsey. Since I first joined the department in 2017, and when you welcomed me back in 2020, your guidance has helped shape me into the scientist I am today. You taught me to think like a scientist, to ask the right questions, and to effectively communicate the answers we find. Your support over these past 9 years cannot be overstated, and I cannot thank you enough. To my committee members: Josh Roering, Leif Karlstrom, and Mark Fonstad, thank you for the guidance you have given me over the past 5 years about each of my projects. Your advice and questions have helped to shape these projects into what they are today. To my parents, Renee and Steve Gardner, you have always encouraged me to follow my passions and to do my best. You have always gone out of your way to ensure that I have what I need to succeed, and I can confidently say that I would not be where I am today without you. I love you both so much. To my undergraduate advisor, Grant Shimer, you taught the first geology class I ever took at Whitman College and in doing so sparked a ravenous curiosity that persists to this day. In your sedimentology and stratigraphy class, I found myself endlessly fascinated by our ability to connect process to product, and how we can use this information to reconstruct earth's evolution through time. The North Slope Alaska Keck project, on which I worked under your guidance, solidified my desire to pursue further geological research. Thank you for fostering that energy and your encouragement. To all my research collaborators, particularly Mike Darin, Scott Bennett, and Steve Hasiotis, my experiences in the field with you have taught me so much about not only your disciplines, but also how to be the best field scientist I can be. To Marla Trox, without you this department would fall into disarray. Thank you for all your work to make sure I was on track and meeting important deadlines. I always look forward to coming into the front office with Cooper (he is especially excited for it) to catch up. You make sure that the deadlines and important things never

pass me by. To all the field assistants I have had over the years: Anthony Downey, Steve Wainwright, Patrick Nonte, Gabe Mager and Zain Shamsuddin, your assistance in the field during extended 2-month field seasons was critical. The desert is harsh, but you all made it just a bit more like home. From finding the body of a missing person in the Mojave desert, discovering a mass grave in Mexico, or late night cribbage tournaments around the campfire, to summiting La Virgen volcano, accidentally attending a funeral thinking it was a quinceañera, or trying to beat offroad speed records from the highway to camp, I'm glad I had companions for the wild adventures the desert brings.

To Larry Lai, we started in the department together in 2017, and over the years your friendship, scientific guidance, and advice are things I have come to value immensely. When we would go and climb volcanoes, I knew we were in for a wild adventure (the Three-Fingered Jack death hike where we both almost lost the ability to walk comes to mind here). I must also express my gratitude to Adrian Broz. You have not only been a dear friend and a researcher to whom I look up, but alongside Larry and I, you were a part of the infamous 2019 Nankoweap Expedition incident in the Grand Canyon. Although the story of that time has been recounted on many occasions, only the three of us truly understand the events that transpired and the emotions involved. I'm not even sure the helicopter rescue crew really understood what went down. It's hard to believe that it has been almost 7 years since then, but I know that I consider you both to be brothers for life. Each September on the anniversary of the expedition, I think about how lucky I am to have had such responsible and capable teammates while handling a crisis. I am so proud of where you all are today, and I look forward to many more years of friendship.

Over the years at University of Oregon, I have found myself surrounded by an ever-growing community of friends. Although I cannot name all the people whom I consider to be friends and for whom I am immensely thankful, there are those who I especially consider to be family: Brennah, Gabbie, Tyler, Josh, Chelsea, Markus, Gordon, Amelia, Helena, and Alex. Some of you started with me in 2017, and others I met along the way over the years. Graduate school can be a long and arduous experience, and without a social support network it can be a lonely one. I have been fortunate enough to have had friends who are truly there for me when times get tough, and with whom I have been able to build so many positive memories. Whether it is tubing down the McKenzie, endless rounds of disc golf, summer whitewater rafting trips, camping on the coast, skiing at Willy P and Bachelor, dance parties at Sunriver, or simply grabbing a beer after (or before) department seminar, there are so many memories I will treasure. There is so much love I have for you all, and I look forward to continuing down the path of friendship with every one of you.

It has been incredibly important for me to pursue hobbies outside of research and school. I have been training Brazilian Jiu-Jistu for 6 years at Grey Wolf Brazilian Jiu-Jitsu. Over the past 6 years I have watched the gym grow from being mostly white belts training in a small space to a large, thriving gym with a team comprised of accomplished athletes from white to black belts. I have made a number of friends from my training partners, and whenever I walk into the gym I know I am surrounded by good people. I'd like to express my gratitude to four people in particular: Professor Mike Yi, Daniel E., Juan C., and Chris K. The Grey Wolf team has been solid community that I am so happy to have found during my time in graduate school. After a long day of writing, nothing beats going into the gym filled with friends who want to beat me up, where I can leave the outside stress behind.

Last, but most certainly not least, I am extremely grateful for my dog, Cooper. You are my boy, and without a doubt, my best friend. You have been by my side almost every single day since I started my doctorate in 2020. You came to me all the way from Texas with your brothers and sisters, as a 6 lb floppy bundle of cuteness with whom I fell in love immediately. You are so incredibly loyal, it almost seems impossible. While I was in desert for long field seasons, your presence and companionship are what I missed the most. Going on walks with you got me out of the house during long workdays, and each time feels like an opportunity to go on an adventure with my best friend. Like you have since day one, you are napping in your office chair next to mine as I write this. Thank you for everything. You are a companion like no other, and I only hope that I bring to your life even a fraction of the same joy and love that you bring to mine. I look forward to the many adventures that lie ahead of us and want you to know that I will always be there for you like you have for me. I love you, Cooper

DEDICATION

This work is dedicated to my best friend Cooper, all the people who have loved and supported me through this journey, and to all those who strive to better understand the world in which we live.

TABLE OF CONTENTS

LIST OF FIGURES

LIST OF TABLES

Table Page

CHAPTER I: INTRODUCTION

Phylogeographic studies on the Baja California Peninsula have observed within-species genetic divergence between northern and southern populations of terrestrial plants and animals, with the locus of the divergence within the San Ignacio trough in the mid-peninsular region. A trans-peninsular seaway connecting the Pacific Ocean to the Gulf of California has been proposed to explain the observed genetic divergence by acting as a physical barrier to gene flow and isolating the two populations. The existence of a seaway would require evidence of Pliocene or younger marine sedimentation in the San Ignacio trough at elevations of 450 m or greater for a complete marine connection between the Pacific Ocean and the Gulf of California. The trans-peninsular seaway hypothesis has not been tested, leaving uncertainty regarding the drivers of genetic divergence in the region.

Quaternary marine terraces have been documented at elevations up to 340 m above sea level along the length of the Baja California Peninsula. In the Laguna San Ignacio area, relict channels that appear to follow paleo-shorelines are observed at elevations consistent with those of marine terraces, however the origin of these relict channels is unknown. If the origin of these channels can be attributed to tides, then the channels can serve as paleo-sea level indicators, offering another constraint for paleogeographic reconstructions of the region. Despite forming under vastly different flow conditions, modern tidal and fluvial channels display remarkably similar planform evolutions and geometries. Although some differences have been recognized between the two channel types, there exists no methodology capable of classifying channel reaches as either tidal or fluvial. This inhibits our ability to classify relict channel reaches as tidal or fluvial using their planform geometries, consequently inhibiting our ability to identify relict tidal channels on uplifted-low relief surfaces and use them to reconstruct paleo-sea levels both in the central Baja California Peninsula and globally.

To address these gaps in our understanding of the controls on biodiversity on the Baja California Peninsula and the geometric distinction between tidal and fluvial channels, both modern and relict, I employ a multi-method approach. Through a field-based approach, I study the sedimentology, stratigraphy, ichnology, and paleopedology of Pliocene sediments in the San Ignacio trough to reconstruct the ancient depositional environments and climate to test the trans-peninsular seaway hypothesis. Using machine-learning algorithms, I develop a methodology for differentiating and classifying modern tidal and fluvial channel reaches, and apply the classification method to relict channels in the central Baja California Peninsula and from localities around the world

In Chapter II, I perform a detailed analysis of the sedimentary facies, stratigraphy, paleosols, and traces fossils of Pliocene-aged sediments exposed at Mesa San Regis, Baja California Sur, Mexico to test for evidence of a trans-peninsular seaway in the San Ignacio trough. Sedimentary structures preserved in the San Regis beds record the depositional processes that emplaced the sediment, and by documenting changes in depositional processes throughout the stratigraphy, I reconstruct the depositional environment and its changes through time. Throughout the San Regis beds, I identified numerous calcic paleosol horizons of varying stages of maturity that allow me to constrain paleoclimatic conditions in the central Baja California Peninsula. I apply known formation ages for analog quaternary calcic paleosols to the soil development stages of the San Regis paleosols and additional use Ar/Ar dates for the capping basaltic andesite and interbedded tephra to develop a timeline for sedimentation and estimate sedimentation rate throughout deposition of the San Regis beds. I also perform a detailed analysis of the trace fossil assemblage for the San Regis beds to provide additional constraints on paleoclimate and depositional environment reconstruction. The results of this study rule out the existence of marine conditions in the San Ignacio trough, and refute the seaway hypothesis, leaving variations in habitat quantity, quality, and climate as potential drivers of the observed genetic differentiation.

In Chapter III, I compiled training and testing datasets of modern tidal and fluvial channels reaches and test the efficacy of three machine-learning classifiers for differentiating between channel types using a segment-scale classification and classification thresholds for individual reaches. I test multi-layer perceptron, random forest, and logisitic regression algorithms using combinations of scaling methods and 145 variables that describe the planform geometries across 69 trials. The results of this study demonstrate that using dominant segment-type thresholds for individual channel reaches a random forest classifier correctly classifies 100% of test reaches as tidal or fluvial, and indicates that the relationship between the local channel width and the local radius of curvature is the most important factor for differentiating between the two channel types.

In Chapter IV, I compile a dataset of 14 relict channels from central Baja California and other localities around the world and apply the trained random forest classifier and classification method developed in Chapter III to these relict channels. The dataset of relict channels includes relict channels of both fluvial and unknown/potentially tidal origin. Relict channels of likely fluvial origin were all correctly classified as fluvial using this approach, while relict channels of unknown origin were assigned a tidal origin. The results of this study are the first time that relict channels of tidal origin have been recognized, and carry significant implications for paleo-sea level reconstructions in tectonically active coastal regions. The findings of this study suggest that relict channels can retain the characteristics of their domain of formation well enough to robustly classify them. However, some channels may display non-unique geometries that arise from natural overlap between the geometries of tidal and fluvial channels, simultaneous shaping by tidal and fluvial processes, post-abandonment modification, and re-shaping of channel planforms during changes in relative sea level.

Chapter II of this dissertation is co-authored with Rebecca J. Dorsey, Stephen T. Hasiotis, Scott E.K. Bennett, Michael Darin, José Luis Antinao, Greer Dolby, and Brian Hausback, and is in review in the journal *Sedimentology.* Chapters III and IV of this dissertation were co-authored with Rebecca J. Dorsey. Chapter III was published in *Earth Surface Processes and Landforms* and Chapter IV will be submitted to *Earth Surface Processes and Landforms*.

CHAPTER II: EVIDENCE FOR THE CONTINENTAL ORIGIN OF PLIOCENE SEDIMENTS IN THE CENTRAL BAJA CALIFORNIA PENINSULA, MEXICO AND IMPLICATIONS FOR CONTROLS ON BIODIVERSITY

This chapter includes unpublished, co-authored material that has been submitted for review in *Sedimentology*. I, Stephen T. Hasiotis, and Rebecca J. Dorsey performed field geologic surveys, sedimentologic and stratigraphic measurements, paleosol descriptions, and trace fossil identification. Scott E.K. Bennett, Michael Darin, and Brian Hausback performed sample collection for geochronological analyses conducted by Matthew Heizler. José Luis Antinao provided feedback for the analysis of soil ages. I am the first author on the paper which involved synthesis and analysis of data, preparation of figures and tables, and writing of the entire manuscript. Greer Dolby and all co-authors provided assistance in data interpretation relevant to their fields and provided editorial feedback for the manuscript and figures.

Introduction

Phylogeographic studies have long recognized a pattern of genetic divergence between northern and southern populations of terrestrial plants and animals along the Baja California peninsula, with the area of differentiation located in the center of the peninsula between N26° and N28° (Fig. 1, Upton & Murphy, 1997; Riddle et al., 2000; Nason et al., 2002; Crews & Hedin, 2006; Lindell et al., 2006; Wood et al., 2008; Dolby et al., 2015; Araya-Donoso et al., 2022). Hypotheses proposed to explain the observed genetic divergence include: (1) isolation of populations by an ancient transpeninsular seaway that crossed the central Baja California peninsula; (2) fragmentation of habitats into glacial refugia by glacial-interglacial climate cycles; and (3) latitudinal variations in the timing and amount of rainfall (Riddle *et al.*, 2000; Dolby *et al.*, 2022). The first hypothesis posits that a narrow seaway connected the Pacific Ocean to the Gulf of California across the center of the peninsula ca. 4–2 Ma, creating a physical barrier that prevented migration and gene transfer between northern and southern populations (Upton & Murphy, 1997; Riddle *et al.*, 2000). The second hypothesis suggests that glacial-interglacial cycles over the last 800 ka led to repeated changes in the spatial extent of plant and animal habitats. In this hypothesis, populations become isolated during interglacial periods as they retreat to colder, higher elevations, and they reconnect during glacial periods as cooler temperatures drive habitat expansion into lowlands. Changes in habitat range, local extinctions, and isolation of populations have all been documented and connected to glacial-interglacial cycles in this region (Graham et al., 2014; Wilder et al., 2014; Dolby et al., 2016, 2018; Valdivia-Carrillo et al., 2017). The third hypothesis suggests that observed north–south variations in seasonal rainfall patterns may have driven changes in the behavior, reproductive patterns, and adaptations of terrestrial plants and animals along the peninsula that have been documented to lead to genetic divergence (Coyne & Orr, 2004; Peñuelas *et al.*, 2004; Thomassen *et al.*, 2013; Shim *et al.*, 2014; Bhattacharya *et al.*, 2018).

In this study, transpeninsular seaway hypothesis is tested with a detailed analysis of Pliocene sedimentary rocks and paleoenvironments in the central Baja California peninsula (Fig. 1). The paleo-seaway hypothesis requires a topographically low area to connect the Gulf of California to the Pacific Ocean, and it predicts a sedimentary record of past marine processes and conditions. Sedimentary deposits provide a record of depositional processes that can be used to reconstruct ancient environments and paleoclimate. This study focused on a Pliocene sedimentary sequence at Mesa San Regis ~12 km east of the town of San Ignacio (Fig. 1). The results indicate the deposits formed in a continental (terrestrial, freshwater) fluvial setting with an arid to semiarid climate. Because older, middle Miocene marine deposits in the San Ignacio trough are too old to be related to the ~4–2 Ma estimates of genetic divergence, and all younger deposits in the San Ignacio region formed in continental environments, our findings clearly refute the transpeninsular seaway hypothesis. These results illustrate the importance of integrating geological tools and methods to test hypotheses for paleo-environments and landscape evolution over geologic timescales.

Geologic and Stratigraphic Framework

The San Ignacio trough is a topographically low region that trends NE across the central Baja California peninsula between flanking mountain ranges to the northwest and southeast (Fig. 1). This low-elevation trough coincides geographically with a hypothesized Pliocene or Pleistocene transpeninsular seaway that has been proposed as the locus of genetic divergence (Upton & Murphy, 1997; Riddle *et al.*, 2000; Dolby *et al.*, 2022). Cenozoic stratigraphy of the midpeninsular region is dominated by volcanic and volcaniclastic rocks that record tectonic evolution over the past 20–30 million years (Fig. 2). The Comondú Group is a sequence of lower to middle Miocene subduction-related volcanic and volcaniclastic rocks that formed above the subducting Farallon plate (Hausback, 1984; Umhoefer *et al.*, 2001; Carreño and Smith, 2007). A southward jump in the Rivera triple

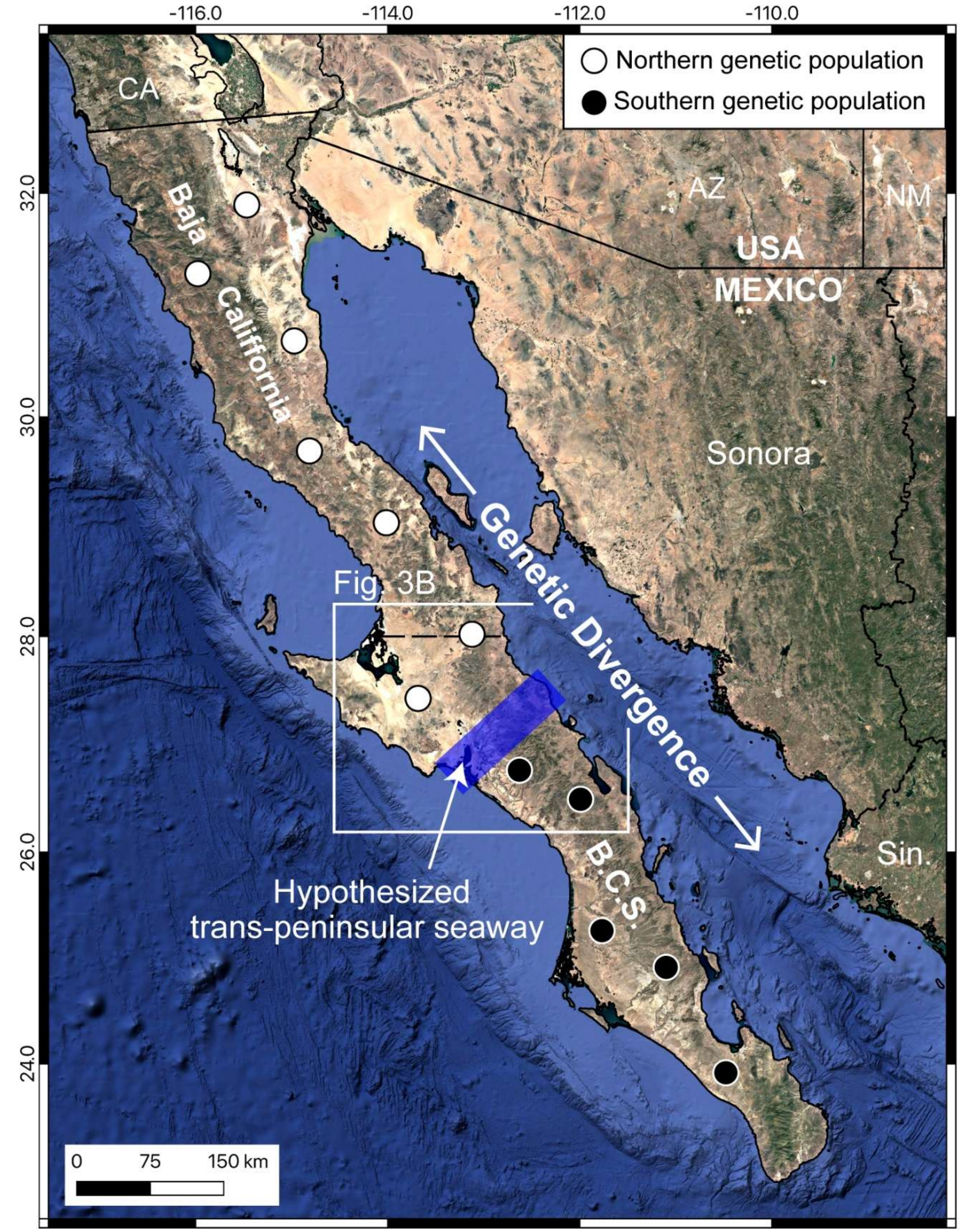

Figure 1. Map of the Baja California Peninsula, Mexico, showing schematic representations of within-species genetic divergence between northern and southern populations of land plants and animals along the peninsula. Blue band shows position of a hypothesized trans-peninsular seaway that is proposed to have acted as a barrier that isolated northern and southern populations. Abbreviations: B.C.S., Baja California Sur; Sin. Sinaloa; CA, California; AZ, Arizona; NM, New Mexico

junction at 12.3 Ma caused the end of subduction and incipient development of a distributed dextral transtensional plate boundary across northwest Mexico (Atwater & Stock, 1998). The Gulf Extensional Province underwent slow NE–SW extension until ~8–7 Ma when relative motion between the Pacific and North America plates rapidly localized into the Gulf of California (Stock & Hodges, 1989; Oskin & Stock, 2003; Bennett & Oskin, 2014; Bennett *et al.*, 2015; Darin *et al.*, 2016; Umhoefer *et al.*, 2018). In the central peninsular region, the San Ignacio Formation consists of tidal to shallow marine fossiliferous sandstone and diatomite that formed in a broad shallow marine shelf during the waning stages of subduction (McLean et al., 1985; Carreño & Smith, 2007), mostly between ca. 15 and 11 Ma (Bennett et al., 2025). The San Ignacio Formation is overlain by the late Miocene (ca. 12–8 Ma) Atajo Formation, composed of interbedded volcaniclastic sandstones, conglomerates and tuffs deposited in alluvial fans that prograded away from developing volcanic centers in the central peninsular region (McLean *et al.*, 1985; Carreño & Smith, 2007; Bennett *et al.*, 2025).

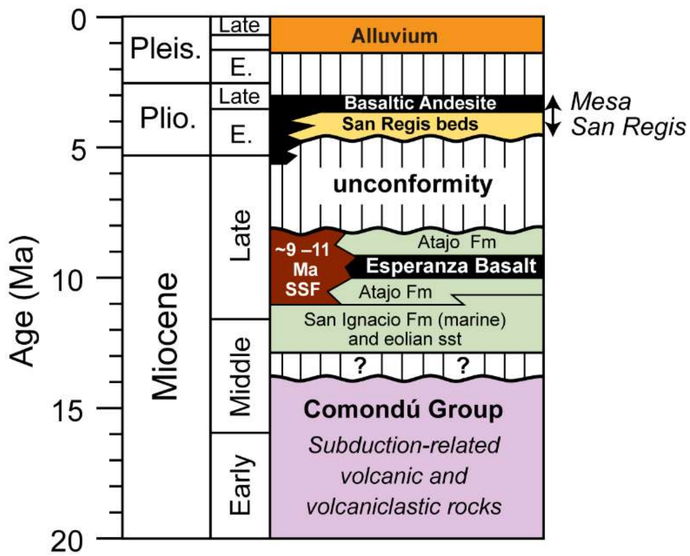

Figure 2: Generalized stratigraphy of the central Baja California peninsula in the San Ignacio area (McFall, 1968; Hausback, 1984; Umhoefer *et al.*, 2001; Schmitt *et al.*, 2006, 2010; Carreño & Smith, 2007; García Sánchez *et al.*, 2019). Pliocene sediments of the San Regis beds are informally named and described for the first time in this study. SSF is volcanic rocks of the Sierra San Francisco, located north of the study area.

The ca. 9.8 Ma Esperanza Basalt is a widespread tholeiitic basalt exposed in the San Ignacio trough and in a belt parallel to the modern Pacific coastline from San Ignacio south to San Juanico (Sawlan & Smith, 1984; Sawlan, 1991; Carreño & Smith, 2007; Bennett et al., 2025). It is overlain by a thin interval of volcaniclastic deposits that represent an upper, post-Esperanza portion of the Atajo Formation (Fig. 2). The San Regis beds are up to ~32-m thick and overlie late Miocene volcaniclastic deposits of the Atajo Formation along an unconformity that spans up to ca. 4 Ma (Bennett *et al.*, 2025). The San Regis beds are overlain by a basaltic andesite lava flow that belongs to a regional system of Pliocene high-Mg basaltic andesite lavas ('bajaites') in the central Baja peninsula (Sawlan & Smith, 1984; Benoit *et al.*, 2002; Calmus *et al.*, 2003; Pallares *et al.*, 2007). Pleistocene and younger units in the region include volcanic deposits of the Tres Vírgenes volcanos and La Reforma caldera, and discontinuous Quaternary alluvial fan and fluvial deposits (Figs. 2, 3; Hausback, 1984; Schmitt et al., 2006; Avellán et al., 2019; Bennett et al., 2025). Mesa San Regis (Figs. 3, 4) is a small feature located ~12 km ENE of the town of San Ignacio. Exposures of the San Regis beds are limited due to weathering of overlying basaltic andesite

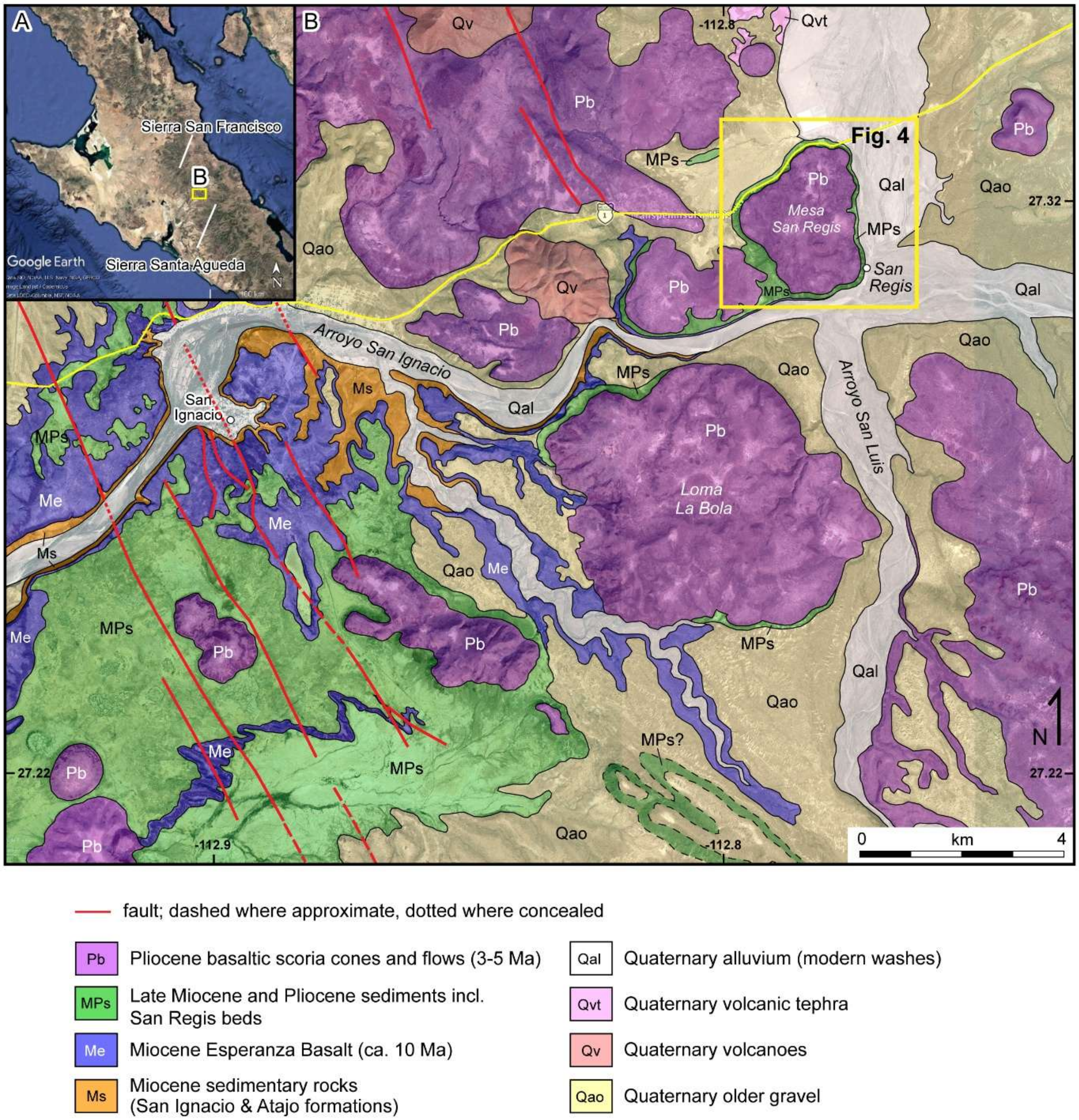

Figure 3. A) Inset map shows topography of the central Baja California peninsula and location of the map area (red box); B) Geologic map of the San Ignacio area showing major volcanic and sedimentary units (see also Fig. 2) and location of Figure 4 Abbreviations: A., Arroyo; G.N., Guererro Negro; S.I.,San Ignacio; S.R., Santa Rosalía.

that has formed a well-cemented carapace of basaltic talus cover. The best exposures of the San Regis beds at Mesa San Regis occur in ~10–15 m-high roadcuts along the northern side of the mesa, and in 20–25 m-high exposures in Arroyo San Ignacio along the eastern side of the mesa. This study is based on observations recorded at these exposures and construction of four stratigraphic sections that comprise nearly the entire thickness of this unit.

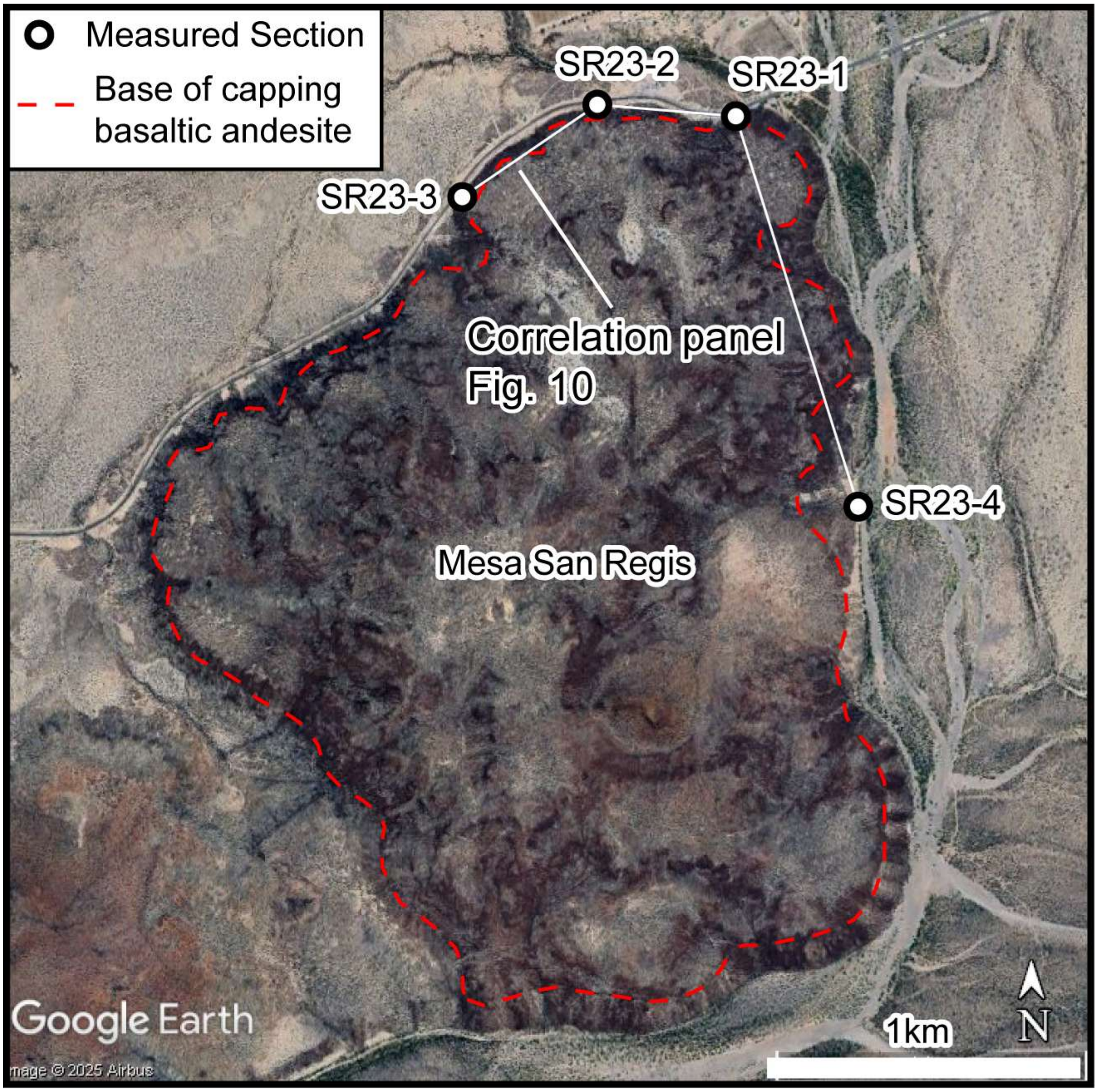

Figure 4. Satellite imagery of Mesa San Regis showing the location of measured sections within the San Regis beds. Red line shows contact of the capping Mg-andesite and the underlying San Regis beds.

Methods

Process sedimentology, stratigraphy, paleopedology (study of ancient soils), and ichnology were applied to determine the origins of the San Regis beds. $^{40}Ar/^{39}Ar$ geochronology methods were used to date an interbedded tephra and capping basaltic andesite lava flow. Lithofacies and stratigraphic analyses were used to reconstruct depositional processes and environments and their changes through time (e.g., Miall, 2022). Stratigraphic sections were measured at cm to m scale to identify spatiotemporal patterns in lithofacies and were combined with paleosol and trace-fossil analyses to refine paleoenvironmental reconstructions. Trace fossils were described by their architectural and surficial morphologies and fill patterns for assignment to an ichnotaxon (Hasiotis & Mitchell, 1993; Bromley, 1996). Paleopedological analyses were used to identify soil horizons and paleosol types and combined with trace fossil interpretations to reconstruct paleoclimate (Hasiotis, 2004; Smith *et al.*, 2008b; Hasiotis & Platt, 2012; Counts & Hasiotis, 2014; Fischer & Hasiotis, 2018; Hanneman *et al.*, 2022; Hasiotis *et al.*, 2025). The amount of pedogenic modification was determined by the amount of disruption of bedding, degree and depth of bioturbation, development of pedogenic features (e.g., massive, granular, blocky textures) and horizonation, and association of redoximorphic mottling (Birkeland, 1999; Brady & Weil, 2002; Hasiotis *et al.*, 2007). Paleosols were classified using the U.S. Soil Taxonomy system (Soil Survey Staff, 1999). Comparison of observed paleosol horizon development in the San Regis beds to a Pleistocene paleosol chronosequence in the Santa Rosalia Basin Baja California (Schorr *et al.*, 2018) allows interpretation of paleoclimatic conditions, estimates of sediment accumulation rates, and an estimate of time span represented by the San Regis beds.

$^{40}Ar/^{39}Ar$ step-heating analyses were conducted on two groundmass concentrates from a mafic tephra (SB19bg-123) and a basaltic andesite (BH20bg-132), and the data, along with analytical details, are provided in the Supplementary File S1. Sample preparation involved crushing and sieving to obtain ca. 1-mm rock fragments that were reacted with dilute HCl in an ultrasonic bath to remove any calcite. Following rigorous rinsing in distilled water, groundmass fragments free of visible phenocrysts were hand-picked while viewed under a binocular microscope. The samples were irradiated for 16 hours in the central thimble at the USGS reactor in Denver, CO, along with flux monitor Fish Canyon Tuff sanidine (FC-2) with an assigned age of 28.201 Ma (Kuiper *et al.*, 2008) to determine J-factors. The irradiation also contained K-glass and CaF_2 to determine interfering reaction parameters. After irradiation, approximately 15 mg of groundmass was loaded into stainless steel trays and evacuated and baked for 4 hours at 150°C. Twelve heating steps using a defocused diode laser were used to construct age spectra and isochron diagrams. Argon isotopes were measured on a ThermoFisher Helix MC mass spectrometer. Plateau ages are determined from selected heating steps and are inverse variance weighted mean dates (c.f Taylor, 1982)and the error is the square root of the sum of $1/\sigma^2$ values. The error is also multiplied by the square root of the

MSWD (Mean Square Weighted Deviation) for MSWD greater than 1. Isotope correlation data yield isochron ages based on regression of selected steps using the weighted linear regression equations of York (1968). All dates are based on a total ^{40}K decay constant of 5.463 x 10-10 /a (Min *et al.*, 2000). Irradiation correction factor and J-error uncertainties are included for the plateau and isochron ages and are reported at 1σ.

Results

Facies Analysis

Seven lithofacies are identified in the San Regis beds (Fig. 5). Sedimentary textures and structures are summarized in Table 1 and interpreted for their corresponding depositional processes. All lithofacies other than the stratified basaltic tephra are immature volcaniclastic sandstone composed of angular plagioclase and volcanic lithic fragments with minor amounts clinopyroxene and little to no quartz. The sandstones could be classified either as lithic arkose or feldspathic litharenite, depending on variations in the ratio of lithic fragments to plagioclase feldspar. The stratified basaltic tephra facies is composed entirely of fresh basaltic andesite fragments reworked from nearby eruption centers.

Paleopedology

Abundant calcic paleosols are identified based on the presence of diagnostic soil horizons (Fig. 6) and pedological structures (Fig. 7). The dominant soil features are carbonate-rich horizons that overprint either the full thickness or upper 5–30 cm of discrete beds. Following well-established carbonate soil classification systems (Gile *et al.*, 1965; Monger *et al.*, 2009), stages I, II, and III calcic (Bk) soil horizons are identified that record varying degrees of soil development in the San Regis beds (Fig. 6). Stage I calcic horizons (Fig. 6A) are weakly carbonate cemented with calcite partially coating the grains and rare calcite nodules (e.g., Gile *et al.*, 1965). In the San Regis beds, calcite nodules are typically present in the upper 5 cm of sandstone beds and recognized by a subtle color change due to calcite cementation. Stage II calcic horizons (Fig. 6B, C) are more strongly cemented and distinguished from Stage I by the common development of strongly cemented calcite nodules and discontinuous carbonate horizons. Distinguishing between Stage I and Stage II horizons is often difficult in the San Regis beds because some Stage I horizons display rare calcite nodules. Therefore, these horizons are grouped into a single category, Stage I–II, which comprise the most common

Facies Name	Facies Code	Description	Interpretation
Normally-graded sandstone (Fig. 5A)	Sng/Sngc	Normally graded, moderately sorted very coarse- to very fine-grained sandstone and minor siltstone. Individual beds range from 0.2 to 0.6 m thick and display sharp basal contacts. Vertical trends in grain size are more subtle in fine-grained variants and better developed in coarse variants. Weak horizontal stratification is rarely preserved in the upper 2–5 cm of individual beds, may have weakly preserved crossbedding (*Sngc*) particularly in upper 15 m of the San Regis beds. Normally graded sandstone (*Sng*) beds typically have 10s of meters lateral extent, and less commonly occur as 60-cm-thick channelized sandstone. The upper 5–30 cm of normal-graded sandstone beds commonly host Bk soil horizons with abundant root traces.	Facies Sng/Sngc formed by lateral accretion on channel bars, levees, and crevasse splays. The upward decrease in grain size records waning-flow conditions during deposition, as indicated by poorly preserved crossbedding and channel geometries. Massive, laterally extensive sheet-like variants were deposited from waning-flow crevasse splays during floods. Numerous sandstone beds with Bk horizons and abundant root traces record soil formation and vegetation growth during periods of bar abandonment, nondeposition, and vadose zone conditions.
Massive sandstone (Fig. 5B)	Ssm	Poorly sorted, structureless fine- to coarse-grained sandstone with common root traces and Bk soil horizons and no visible grading or sedimentary structures. Massive sandstone is observed in paleochannels 20–30 cm thick and 1–5 m across. Nonchannelized variants are up to 1.2 m thick and resemble sheetlike variants of normally graded sandstone (Facies Sng/Sngc) but with no grading.	The *Ssm* facies is interpreted as channel-fill or crevasse-splay deposits that accumulated in overbank areas and bar tops. Channelized sandstone packages record rapid accumulation during floods. Sheetlike variants are interpreted as crevasse splays or broad, shallow channel fills where rapid accumulation prevented development of grading. Common root traces and Bk horizons suggest vegetation growth and soil formation on bar tops and overbank areas during periods of nondeposition and vadose zone conditions.
Cross-bedded pebbly sandstone/sandstone (Fig. 5C)	Spc/Ssc	Medium- to very coarse-grained, moderately to poorly sorted, cross-bedded pebbly sandstone and sandstone with rounded to subrounded pebbles in the pebbly variant *(Spc),* and no pebbles in the sandstone variant *(Ssc)*. Beds of Spc are 1–1.2 m thick, while Ssc beds range from ~10 to 20 cm. Low-angle tabular crossbedding is highlighted by alternating pebble-dominant and sand-dominant foreset strata, or as weakly preserved low angle laminations with rhizotubules aligned with foreset surfaces. Bk horizons are absent in this facies, though root traces from overlying paleosols locally extend downward into this lithofacies in lowermost San Regis beds.	Facies Spc/Ssc is inferred to record deposition by lateral accretion on channel bars and levees. Planar crossbedding provides evidence for bedform migration. Alternating pebble-dominant and sand-dominant foresets likely record fluctuations in flow, potentially related to seasonal flood events. The absence of soil horizons suggests rapid deposition that did not allow time for soil formation, even in vadose zone conditions.

Facies Name	Facies Code	Description	Interpretation
Horizontally-stratified sandstone (Fig. 5D)	Ssh	Well-sorted, fine-grained sandstone to silty sandstone with weak horizontal stratification, uncommon in the San Regis beds. Individual beds 5–10 cm thick occur in intervals 0.5–3.5 m thick. Weak ped structures locally preserved in upper cm.	Facies *Ssh* is interpreted to record deposition under lower plane bed conditions on bar tops, islands, and overbank areas. The fine grain size suggests deeper and/or slower, subcritical flow. Deposition took place during floods under slackwater conditions produced by high flow depth and low velocity.
Interbedded sandstone and conglomerate (Fig. 5E)	SCi	Medium- to coarse-grained sandstone interbedded with granule to sandy cobble conglomerate. Beds range from 5 to 15 cm thick. Bases of conglomerate interbeds are sharp and irregular, whereas bases of sandstone interbeds are typically gradational and transitional from underlying conglomerate. Commonly structureless, weak horizontal stratification rarely observed in sandstone interbeds. This facies is observed in broad, shallow (20–50 cm) channels 5 m to 8 m across. No pedogenic structures or soil horizons are observed.	Facies SCi formed by episodic deposition in shallow river channels. Alternation of conglomerate and sandstone records pulses of deposition over multiple floods. Sharp erosional bases of conglomerate interbeds record scouring during initial high energy floods, whereas the gradational transition to overlying sandstone records continued lower-energy flood deposition. The general absence of sedimentary structures suggests rapid deposition.
Stratified basaltic tephra (Fig. 5F)	Tbs	Moderately to well-sorted, horizontally stratified, granule conglomerate and medium- to very coarse-grained sandstone composed of basaltic tephra with common rhizohaloes, preserved in shallow channels (20–60 cm deep, 5–20 m wide) and adjacent overbank areas. Channel axes oriented North-South. Basaltic tephra occurs at two stratigraphic intervals in roadcuts along the northern margin of Mesa San Regis, and as a reworked tephra-rich sandstone outside of paleochannel margins (Fig. 10). Beds typically 2–8 cm thick display subtle normal grading and inverse-to-normal grading.	This facies records deposition from migrating 2D bedforms in shallow channels. Normal and inverse-to-normal grading was produced by sediment avalanching down lee side of bedforms. Deposition took place in shallow channels and intervening overbank areas. The pure basaltic composition of this facies is interpreted to record transport and deposition of reworked detritus from nearby basaltic andesite eruptions.
Massive Conglomerate (Figs. 5G, 5H)	Cgm	Poorly sorted, unstratified pebble to cobble conglomerate with rounded to subrounded clasts in a sandy matrix. Beds are 25–110 cm thick. At 1 m in measured section SR23-4 (Fig. 10) sedimentary texture is highly modified by a well-developed Stage III Bk horizon with large root traces penetrating 1.5 m downward into underlying deposit.	Facies Cgm formed by rapid deposition during high-energy floods, within channels and as gravelly overbank or bar top deposits. Stage III Bk horizons and well-developed root traces suggest prolonged periods of nondeposition to facilitate mature soil formation and establishment of robust vegetation on bar-top surfaces in vadose zone conditions.

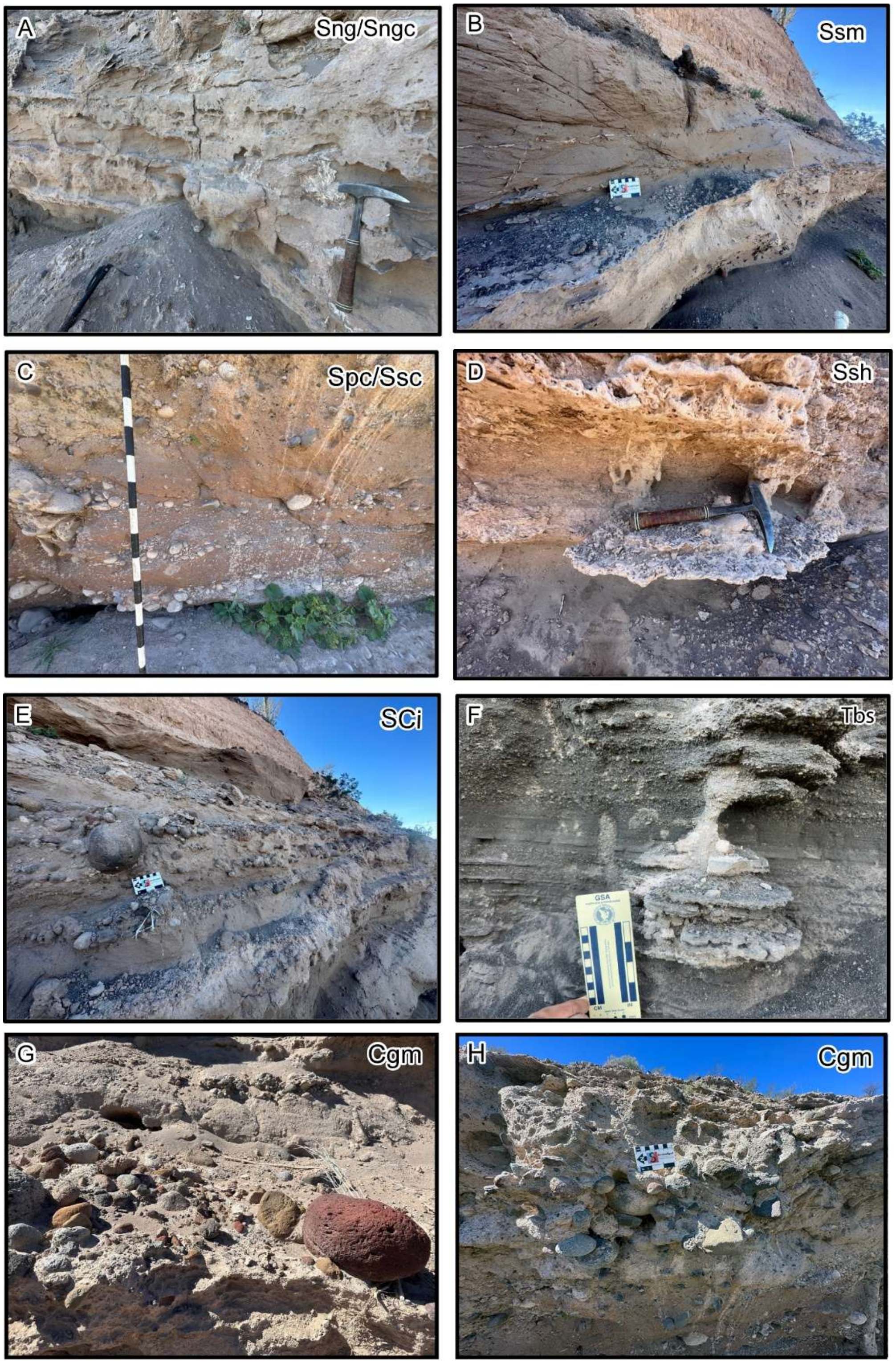

Figure 5. Representative photos of facies present in the San Regis Beds; (A) Normally graded sandstone, with preserved crossbedding; (B) Massive sandstone within a channel; (C) Pebbly sandstone with gravelly crossbedding and lenticular gravel bodies; (D) Horizontally stratified sandstone with weakly preserved bedding planes highlighted by pedogenic carbonate; (E) Interbedded sandstone and conglomerate; (F) Stratified basaltic tephra with weak rhizohaloes present; (G, H) Massive pebble to small boulder conglomerate. Clasts are coated with pedogenic carbonate in a Stage III carbonate horizon.

horizons make up ~35% of the 20 soil horizons observed in the San Regis beds, and stage I–II calcic horizons make up the remaining 65%. Pedogenic carbonate occurrence observed in this study has been attributed to arid or semiarid climates where evaporation is greater than precipitation, and precipitation is seasonal (Hasiotis *et al.*, 2007).

Figure 6. Examples of Bk horizon development in the San Regis beds. (A) Stage I Bk horizon with weak cementation and rare nodules; (B) Stage II Bk horizon with abundant nodules, displacement of clods, discontinuous cementation, and rhizocretions; (C) Stage II Bk Horizons with abundant rhizocretions and discontinuous carbonate cementation; (D) Stage III Bk horizon with well-developed carbonate cementation forming a continuously cemented layer. Large (1-1.5 m) rhizocretions present. Rock hammer 32.5 cm long, staff 1.5 m tall

Facies of the San Regis beds display additional pedogenic structures that record calcic soil development (Fig. 7). The most prevalent soil structures are rhizoliths (root traces) that reflect varying timespans of vegetation growth. Rhizoliths in the San Regis beds may be considered rhizolites because the textures and internal fabrics are pervasively those of root traces (e.g., Klappa, 1980), although this term is rarely used. The most common root traces observed in this study are rhizocretions (Fig. 7A), very well-cemented columnar structures ranging from ~5 to >150 cm deep

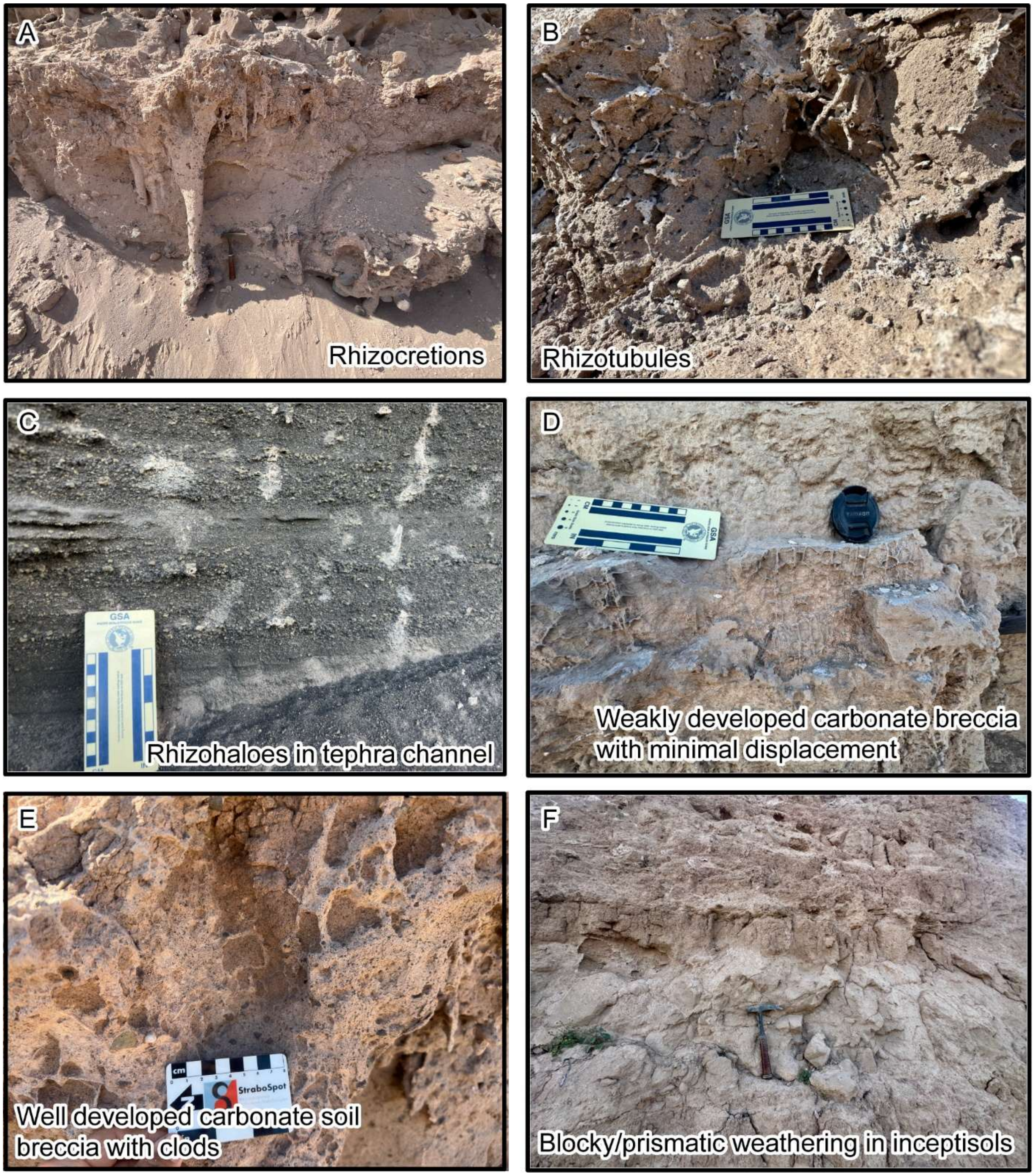

Figure 7. Common pedogenic structures in paleosols of the San Regis beds. (A) Well-developed rhizocretions in sandstone; (B) Rhizotubules in sandstone; (C) Rhizohaloes developed in a stratified basaltic tephra; (D) Weakly developed carbonate soil breccia, with minimal displacement of soil clods; (E) Well-developed carbonate soil breccia with displaced soil clods; (F) Blocky weathering seen in inceptisols of the upper San Regis beds; Rock hammer 32.5-cm long

that penetrate down from calcic paleosol horizons. They locally exhibit a texture like that of root bundles near the calcic horizons from which the structures originate. Columnar structures do not preserve hollow tubes in the center and are instead filled by calcite cement. The advanced degree of cementation suggests that the original root was present long enough for pedogenic mineralization to extend up to 10 cm away from the root.

The second most common root traces observed in the San Regis beds are rhizotubules (Fig. 7B), recognized in the San Regis beds as individual or masses of weakly to moderately cemented hollow tubes with walls <2-mm thick. Unlike rhizocretions, rhizotubules are exceptionally fragile. Rhizotubules are interpreted to record shorter lived development than the rhizocretions, as pedogenic mineralization only occurs 1–2 mm away from the original root, precipitating cement only during the lifespan of the plant (e.g., Klappa, 1980).

The least common root traces in the San Regis beds are rhizohaloes expressed as narrow (2–5-cm wide) vertical zones (3–15-cm deep) of light carbonate coating on the grains surrounding a very weakly cemented root cast (if present) (Fig. 7C). Rhizohaloes are observed only in a highly permeable basaltic tephra-filled channel. They represent weakly developed root traces where very weak pedogenic mineralization occurs around root hairs during the lifespan of the plant.

Calcic paleosols also display carbonate soil breccias and blocky or prismatic ped structures in Bk horizons accentuated by weathering (Fig. 7D, E). Carbonate breccias appear as clods of sand and/or silt ranging from a few mm to 3 cm diameter, with carbonate cement between the clods. Weak breccias display minimal displacement between the clods (1–2 mm) (Fig. 7D), whereas well-developed breccia often exhibits up to several centimeters of displacement between clods (Fig. 7E). While the degree of brecciation increases with increasing calcic horizon stage, not all calcic horizons have breccias. Blocky and prismatic structure is sometimes present in weakly developed Stage I Bk and AB horizons (Fig. 7F), suggesting formation of soil peds and pedogenic mineralization.

Ichnology

Ten trace fossils were identified in the San Regis beds, providing additional context for interpreting depositional environments, paleosol formation, and paleoclimate.

Fictovichnus isp.

Fictovichnus is a highly abundant trace fossil observed throughout the San Regis beds. They are observed as individual cells or clusters of cells with oblong and equant morphologies. Oblong varieties (Fig. 8A) are 2–3 cm tall with a diameter approximately 1 cm, while equant varieties (Fig. 8B) are 2 cm tall with a diameter of 1.5–2 cm. Oblong forms are poorly cemented and display open chambers where the terminus of the cell has been eroded or opened by the tracemaker. Equant

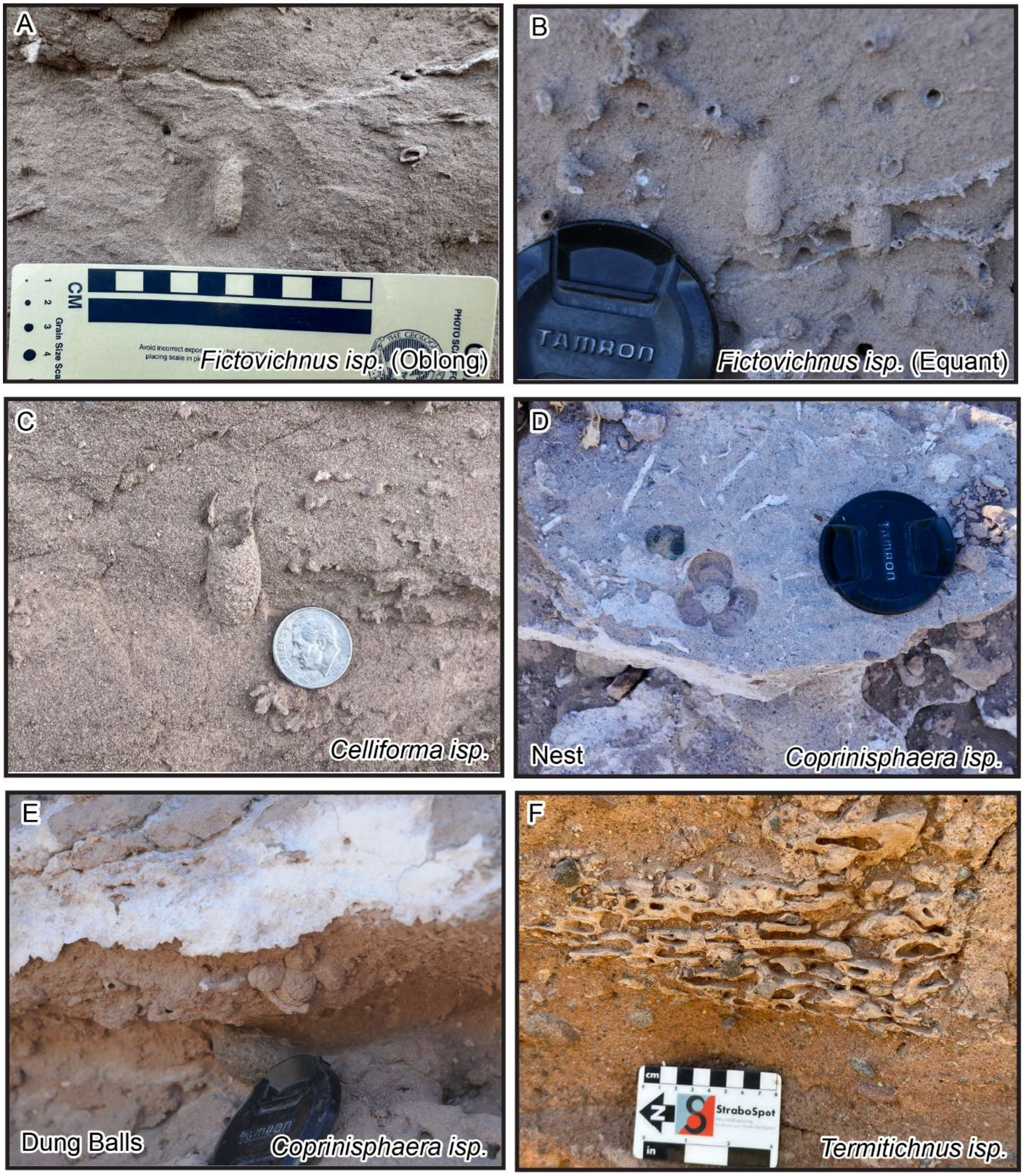

Figure 8. Representative photographs of continental trace fossils within the San Regis beds; (A) Oblong variant of *Fictovichnus isp*. Hymenoptera cell; (B) Equant variant of *Fictovichnus isp*. Coleoptera pupation chamber*;* (C) *Celliforma isp.* solitary bee cell with flask shape and open top; (D) Three-branched *Coprinisphaera isp.* dung beetle nest; (E)Spherical to quasispherical *Coprinisphaera isp.* dung balls; (F) Calcified galleries and chambers of *Termitichnus isp.* termite nest; Lens cap diameter 7 cm.

forms are well cemented and do not display any openings. They are typically observed below Bk soil horizons in weakly cemented C horizons. Observed *Fictovichnus* cells range from solitary cells to clusters of 2–6 cells.

Fictovichnus is attributed to beetles (Coleoptera) and wasps (Hymenoptera) that burrow within the vadose zone (Johnston *et al.*, 1996; Hasiotis, 2003). These tracemakers form cells or cocoons below the surface that serve as pupation chambers produced by the larvae. *Fictovichnus* are commonly found in carbonate paleosols typical of arid to semi-arid environment, and often in association with such other similar trace fossils as *Celliforma* (Johnston *et al.*, 1996; Hasiotis, 2003; Cardonatto *et al.*, 2016). The number of cells present in wasp nests typically scales with population, with larger populations producing nests including 200 or more cells (Hasiotis, 2003). The comparatively small number of *Fictovichnus* cells in single clusters of the San Regis beds suggests that they were constructed by solitary tracemakers spread out over the landscape rather than a large colony.

Celliforma isp.

Celliforma is a common trace fossil in the San Regis beds. They are typically observed as individual cells 10–30 cm below a Bk soil carbonate horizon in weakly cemented C horizons (Fig. 8C). They appear as either intact or partially opened oblong, flask-shaped cells 1–2 cm long and 1 cm across. The exterior of cells has a similar texture to the surrounding sediment while the interior of cells has a smooth surface, where visible. The cells are only slightly better cemented than the surrounding sediment, which makes them very fragile. Removal from outcrop without damage is therefore difficult, precluding species level identification. *Celliforma* in the San Regis beds are solitary, and no connection to tunnels or larger nest structures were observed.

Celliforma is attributed to soil bees (Hymenoptera) that burrow and form cells and nests where eggs are laid on a pollen loaf on which an egg hatches and the larvae will feed (Genise, 2000; Hasiotis, 2003; Cardonatto et al., 2016). Single-cell burrows are typically associated with solitary bees, while larger nesting structures are made by solitary bees or large colonies (Hasiotis, 2003). These trace fossils are formed in the vadose zone of fluvial deposits, above the water table in the vadose zone of well-drained soils (Hasiotis, 2002, 2003, 2004, 2008; Genise et al., 2010). *Celliforma* are commonly associated with calcic paleosols formed in arid to semiarid conditions where precipitation may increase periodically (e.g., seasonal storms) (Alonso-Zarza & Silva, 2002; Genise & Edwards, 2003). *Celliforma* are commonly observed in proximal to distal floodplain deposits, and the distribution and morphology of cells in the San Regis beds are consistent with dry to the drier end of wet-dry climates (Hasiotis *et al.*, 2007). *Celliforma* are also associated with *Coprinisphaera* in paleosols formed in fluvial deposits on alluvial plains, abandoned bars, levees, and splays (Genise, 2017). The association of rhizoliths with *Celliforma* and well-developed calcic horizons is consistent with scrublands in arid to semiarid climates (Hasiotis *et al.*, 2007; Genise, 2017).

Coprinisphaera isp.

Coprinisphaera is the second most abundant trace fossil observed in the San Regis beds. Two distinct morphologies are preserved only in well-developed (Stage II, III) calcic horizons. The first morphology is a top-down exposure of a trilobate nest structure ~7 cm across that surrounds a central column (Fig. 8D). Each lobe displays menisci extending outwards from the central column. Brood balls are not present in the trilobate structure, potentially due to the removal of material by the larvae or lack of preservation. The second morphology consists of calcite-cemented spherical to quasi-spherical structures (brood balls) 2–3 cm across observed in clusters of 3–4 spheres (Fig. 8E).

Coprinisphaera sp. are commonly attributed to the breeding structures of dung beetles (Hasiotis, 2002, 2003; Laza, 2006). Nests display a range of morphologies, typically comprising a main vertical shaft that terminates in a single chamber or splits into multiple small cells where dung balls (brood balls) are stored (Hasiotis, 2002, 2003; Laza, 2006). Dung balls range from 1.5 to 4 cm in diameter (Laza, 2006), like sizes observed in the San Regis beds. *Coprinisphaera* are commonly attributed to distal and proximal floodplain environments in the vadose zone (Hasiotis, 2002). They are also observed in association with *Celliforma* and rhizoliths in paleosols formed on fluvial deposits such as abandon bars, crevasse splays, and levees (Hasiotis, 2002, 2003; Genise, 2017). When observed with rhizoliths and in calcic paleosols, *Coprinisphaera* are typical of arid to semiarid climates. The abundance of vegetation and dung balls suggests a dry to wet-dry continental environment characterized by evaporation that exceeds precipitation with seasonal variations in precipitation (Hasiotis *et al.*, 2007; Genise, 2017).

Termitichnus isp.

Termitichnus was observed in one instance in a C horizon below a Stage III Bk horizon at the base of the composite San Regis beds section. *Termitichnus* is expressed here as calcite-cemented tunnels and chambers forming a rectilinear geometric pattern that covers an approximately equant area of 25 x 25 cm (Fig. 8F), suggesting a relatively low nest volume. Calcite cement on tunnel walls is ~0.5 cm thick, while galleries and chambers are 0.5–1 cm tall and 1–2 cm wide. This trace fossil occurred directly adjacent to large rhizocretions 1.5 m deep.

Termitichnus is attributed to the nesting structures and colonies of termites (Hasiotis & Dubiel, 1995; Hasiotis, 2003). Ancient termite nests have been observed in association with rhizoliths, which is consistent modern termites using decaying roots, vegetation, and trees as food sources. The *Termitichnus* observed at the base of the San Regis beds was found adjacent to well developed, large rhizocretions below a Stage III carbonate horizon suggesting that dead roots may have been a sought-after food source for the tracemaker. Termites are found in both humid, semiarid, and arid environments, and have nests that increase in complexity depending on the level of microclimatic control within the nest (Wood, 1988; Dibog *et al.*, 1998; Eggleton, 2000). Given the prevalence of arid to semiarid climates indicated by other trace fossils within the San Regis beds, the tracemakers of *Termitichnus* were likely arid-type as opposed to humid type. The low complexity of the observed nest suggests that minimal moisture and temperature control was required by the termites, consistent with the behavior of dryland termites that feed on woody debris rather than growing fungi within the nest for feeding. No epigeal termite mounds were observed in the San Regis beds, but their presence during deposition cannot be ruled out, as mounds constantly undergo erosion and redistribution (Wood, 1988).

Parawanichnus isp.

Parawanichnus was observed in the lower San Regis beds on the eastern side of Mesa San Regis (Fig. 9A). They appear as discontinuous horizontal flattened ellipsoids in the sediment. 0.5-cm tall and extending 2–3-cm wide, offset vertically and laterally from each other by 5–10 cm. No vertical shafts or subhorizontal tunnels were visible in the cross section.

Parawanichnus is widely attributed to ant nests used for a range of behaviors that include feeding, breeding, and habitation (Bown *et al.*, 1997; Hasiotis, 2003; Hembree & Hasiotis, 2008). They commonly form near root traces (Hasiotis *et al.*, 2007; Hembree & Hasiotis, 2008). These nests, like all the other trace fossils described here, formed in the vadose zone above the water table where the depth to the water table is a controlling factor for the depth of development (Hasiotis, 2002, 2003, 2004; Hasiotis and Platt, 2012). Modern ant nests and *Parawanichnus* are documented in distal to proximal floodplain and transitional environments where sufficient depth to the water table permits formation in the vadose zone (Hasiotis, 2003; Hasiotis *et al.*, 2007). Small and volumetrically

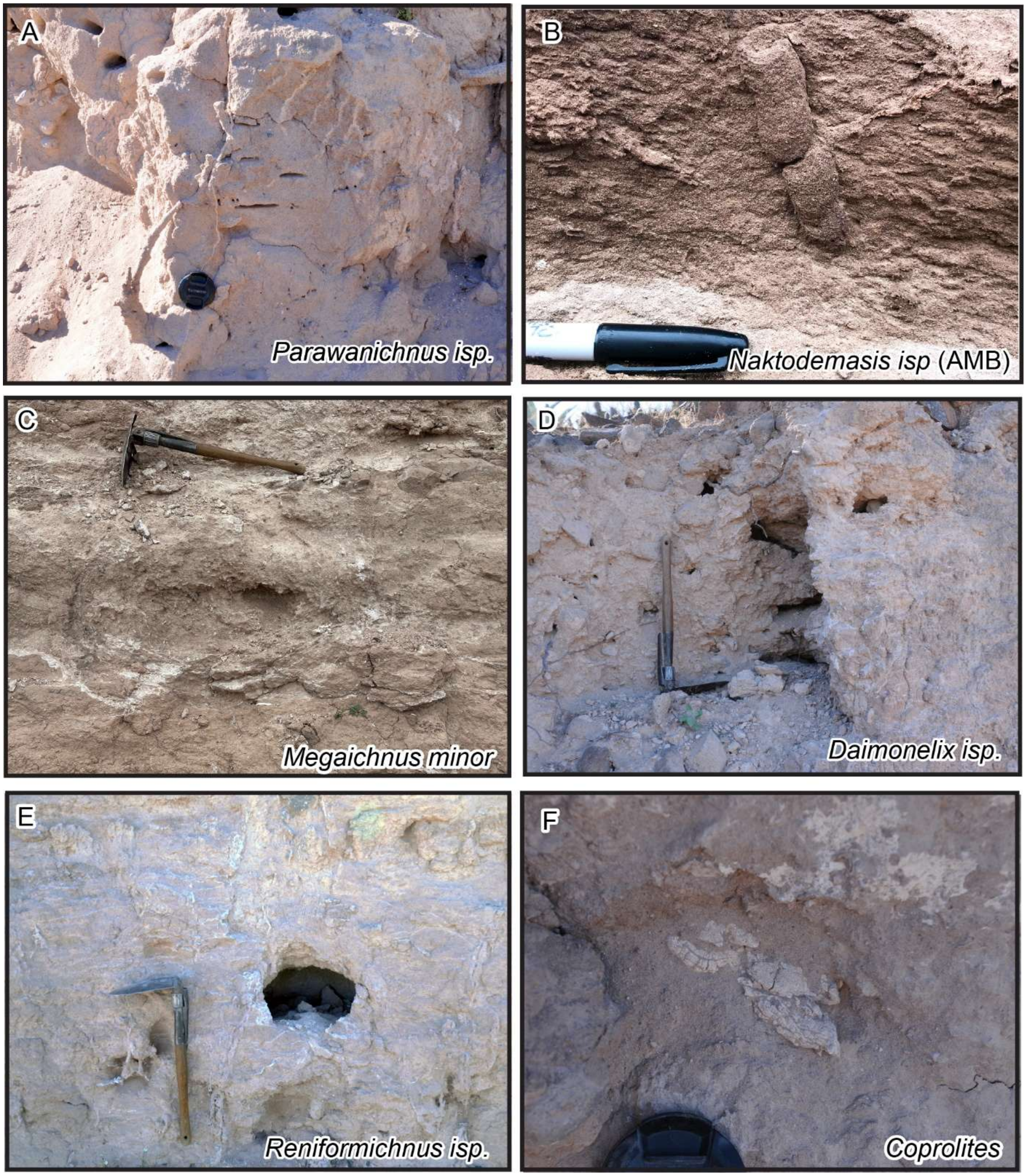

Figure 9. More common trace fossils of the San Regis beds. (A) Hollow horizontal chambers of *Parawanichnus isp.* in weakly cemented sandstone; (B) Bundled meniscate packages of *Naktodemasis isp.*; Filled *Megaichnus minor* with internal fabric following the outer boundaries of the burrow; (D) Hollow helical burrow of *Daimonelix isp.* with rectangular burrow cross sections; E) Cavity with reniform (bi-lobate) cross-section of *Reniformichnus isp.*; F) White, desiccated coprolites *in situ*. Shovel is 50-cm tall; Lens cap diameter 7 cm.

confined ant nests, such as those observed in the San Regis beds, are typically associated with dry to wet-dry climates with periodic (seasonal) increases in precipitation(Hasiotis *et al.*, 2007). Fossil ant nests with more vertical geometries such as *Daimoniobarax* (Smith *et al.*, 2011) may be present in the

San Regis beds but were not definitively identified due to well-developed calcic horizons, vertical rhizocretions, and calcite nodules that are morphologically similar and may mask adjacent ant nests.

Naktodemasis isp.

Two examples of *Naktodemasis* were observed in the San Regis beds (Figure 9B). The trace fossils occur in weakly cemented massive sandstone below weakly to moderately developed (Stage I–II) calcic horizons. The burrows are 4–7-cm long and 1-cm wide, oriented vertically. The walls of the burrows are unlined, and bounded meniscate backfill packets are displayed along the entire length.

Naktodemasis is a type of adhesive meniscate burrow (AMB) typically associated with the locomotion of nymphs belonging to the Cicadidae (Hemiptera) and larvae belonging to the Cydnidae, Carabidae, and Scarabidae (Coleoptera) (Smith et al., 2008; Counts & Hasiotis, 2008; Hasiotis, 2008). Active backfill during movement produces menisci in the burrow (Smith et al., 2008; Hasiotis 2008; Counts & Hasiotis, 2009). *Naktodemasis* forms in the vadose zone near roots in distal and proximal floodplain deposits, and co-occur with *Celliforma, Coprinisphaera, Parawanichnus,* and rhizoliths only in distal floodplains (Hasiotis, 2002, 2004; Hasiotis *et al.*, 2007; Smith *et al.*, 2008a). The occurrence of *Naktodemasis* is consistent with *Fictovichnus* pupation chambers for Coleoptera pupae that later hatch as adults.

Megaichnus minor

The largest and least common trace fossil identified in the San Regis beds is *Megaichnus minor* (Fig. 9C). A single instance of *Megaichnus minor* was observed in weakly cemented structureless sandstone with few to no rhizoliths surrounding the burrow. The burrow is roughly equant, ~40–50-cm wide, and is identified based on a well-defined outer bounding surface with infill that shows internal fabrics parallel to the outer boundary.

Megaichnus major and *Megaichnus minor* are best documented in Brazil where they have been observed as intact tunnels extending horizontally 10s of meters with widths up to 4 m (Lopes et al., 2017). The distinction between *M. major* and *M. minor* variants is based on two distinct size groups, with examples <1.5-m diameter assigned as *M. minor*, whereas larger types up to 4-m diameter are assigned as *M. major*. Tracemakers for *Megaichnus* are not clear, although it is commonly attributed to medium to large mammals, such as ground sloths or giant armadillos (Lopes *et al.*, 2017). The burrow observed in this study is slightly smaller than the size typically associated with *Megaichnus* (60 cm). The sandy infill of the burrow prevented investigation of the burrow walls for digging marks that may have shed light on the tracemaker. *Megaichnus* burrows in Brazil are thought to have formed during the Chapadmalalan age (4–3 Ma) (Lopes *et al.*, 2017). If the tracemaker was mammalian or reptilian, this burrow also formed in the vadose zone above the water table, likely near a source of water to support the tracemaker, consistent with burrowing in a floodplain of a fluvial system (Hasiotis, 2002, 2004; Hasiotis *et al.*, 2004; Hembree & Hasiotis, 2008).

Daimonelix isp.

A single instance of *Daimonelix* was observed in the San Regis beds (Fig. 9D). The burrow is a helical tunnel system with two branching tunnels to the paleosurface. The exposed burrow is ~60-cm deep. Burrows forming the helical section and paleosurface branches have a rectangular cross section, with heights ranging from 3–6 cm and widths between 10–17 cm. The spiral tunnel structure is well preserved in cross section.

Daimonelix are helical burrows previously attributed to an extinct species of beaver, *Paleocastor* (Barbour, 1897; Martin & Bennett, 1977; Raisanen & Hasiotis, 2018; Doody et al., 2024). Burrows of *Paleocastor* have a tight helical geometry with circular tunnel cross sections. In contrast, the helical burrows observed in the San Regis beds have a clear rectangular tunnel cross section and a much looser spiral shape. This geometry is not consistent with descriptions of *Paleocastor* burrows. Studies of extant monitor lizards have shown that they produce loose helical burrows and nesting structures that extend up to 3 m below the surface and have tunnel dimensions that overlap with the lower range of those observed in the San Regis beds (Doody *et al.*, 2015, 2024). *Daimonelix* observed in the San Regis beds were likely produced by a Pliocene monitor-like lizard in an arid environment resembling the habitat of extant monitor lizards (Ibrahim, 2002).

Reniformichnus isp.

One instance of *Reniformichnus* was observed in the upper San Regis beds on the north side of Mesa San Regis. This trace fossil appears as a hollow cavity with an entrance approximately 17-cm tall and 27-cm wide (Fig. 9E). The upper boundary of the entrance cavity is arched or semicircular, while the bottom boundary has a gentle bilobate geometry. No continuous tunnel was observed, suggesting that the cavity is a chamber at the terminus of a burrow. The chamber is slightly larger than the cavity entrance, with approximate internal dimensions of 25–30-cm tall, 35–45-cm wide and 25–30-cm long. Collapsed wall material was observed within the chamber, suggesting that the dimensions may have been similar to the cavity entrance during formation. No tracemaker scratches or other markings were observed on the interior of the cavity.

Reniformichnus has been described in Permian to Jurassic-aged continental deposits, and is attributed to various vertebrate tracemakers, such as Therapsids, Procolophonids, Sphenodontids, and other tetrapods living on floodplains or adjacent to open bodies of water (Hasiotis *et al.*, 2004, 2025; Krummeck & Bordy, 2018). Morphologically similar burrows described in Miocene calcic paleosols indicate burrowing behavior to evade predation and for protection from the elements in arid conditions (Cardonatto & Melchor, 2018). *Reniformichnus* burrows are formed in the vadose zone, allowing tracemakers to live in the burrows. The dimensions of *Reniformichnus* in the San Regis beds and the abundance of calcic paleosols are consistent with those of previous studies. The tracemaker is unlikely to be a Therapsid or Procolophonid, as these were long extinct by the Pliocene. Although no specific tracemaker can be identified, the tracemaker was likely a Pliocene tetrapod, such as a mammal or tortoise.

Coprolites

Coprolites were observed only in the upper San Regis beds along the northern exposures on Mesa San Regis. They occur as hard, brittle, white, desiccated pieces ranging from 1–5-cm long and 1–3-cm in diameter (Fig. 9F). The outer surface of individual pieces displays linear desiccation features. Coprolites are commonly attributed to the fossilized feces of vertebrate animals.

Stratigraphic Architecture

Four stratigraphic sections were measured in detail and correlated by hanging them from the base of the capping basaltic andesite lava (Fig. 4) to construct the detailed stratigraphic panel in Figure 10. Sedimentary facies in the four sections are dominated by normally graded sandstones (*Sng*) with little to no lateral changes in grain size or depositional environment (Fig. 10). The stratigraphic panel reveals two laterally discontinuous tephra channels at two unique stratigraphic levels in the northern sections (sections SR23-1, -2, -3), for which no equivalent interval was observed in the southern exposure (SR23-4), likely due to lateral pinch-out and/or a covered interval in the south.

Trace-fossil assemblages display slight lateral variations in the stratigraphic panel (Fig. 10). Rhizoliths are the dominant soil features and are present in most intervals of the sections, indicating persistent vegetation growth during deposition of San Regis beds. The animal trace-fossil assemblage is uniformly distributed across most of the four measured sections. Trace fossils are

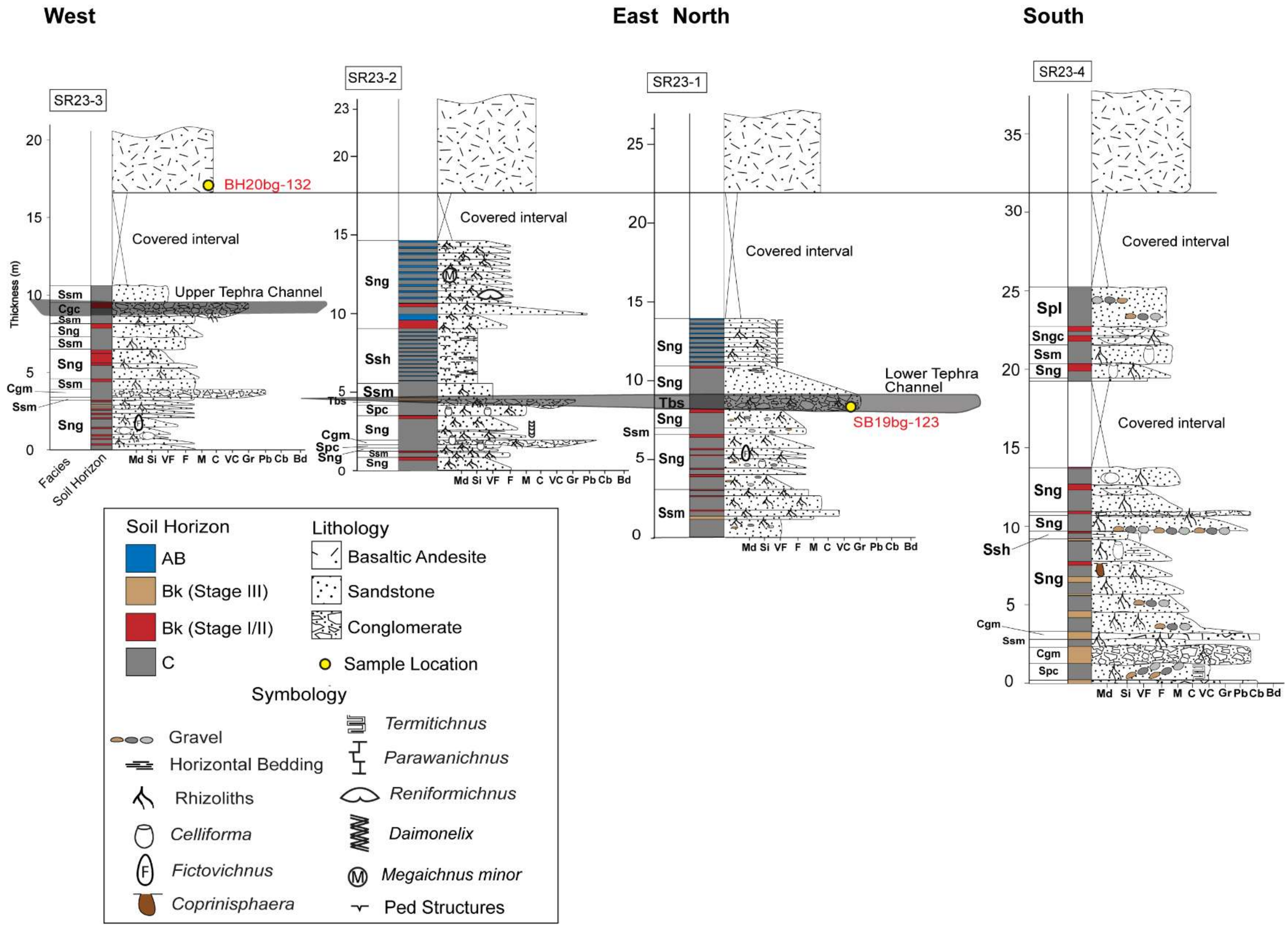

Figure 10. Correlation panel for the San Regis beds. Changes in calcic horizon development indicate weak to nonexistent calcic horizon development up-section and from east to west, with increased calcic horizon development from North-South between SR23-1 and SR23-4. Dark Grey highlighted zone shows the two tephra channels.

notably absent in uppermost intervals of sections SR23-1 and SR23-2, suggesting local variations in habitability or nonpreservation. These variations could be due to more frequent depositional events, a shallower depth to the water table, or a combination of those two factors.

Inceptisols lacking Bk horizons are most common on the north side of Mesa San Regis in sections SR23-1 and SR23-2. Equivalent intervals in SR23-3 and SR23-4 are either covered or contain paleosols with Bk horizons. Correlation of inceptisols lacking Bk horizons to intervals with well-developed Bk horizons suggests spatial variability in factors that influenced soil development. Sediment composition and distribution of trace fossils are spatially uniform, suggesting that changes in parent material or organisms were not the major drivers of variable soil development. The small size of the study area (<2 km lateral distance) and absence of paleotopographic relief indicate that changes in climate and topography also did not influence variations in soil development. Lateral variations in soil development (Fig. 9) likely reflect subtle variability in local topography, groundwater profile, and/or sedimentation rates associated with coeval channel and overbank subenvironments, which are known to control the duration of surface exposure and depth to the water table and thus enhance or inhibit soil carbonate development (Smith, 1990; Kraus & Aslan, 2009; Fischer & Hasiotis, 2018). Intervals of weaker soil development in SR23-1 and SR23-2 likely represent areas with more frequent sedimentation events and locally faster accumulation rates compared to equivalent intervals of better-developed soils in SR23-3 and SR23-4.

$^{40}Ar/^{39}Ar$ Geochronology

Two rock samples were collected and dated to constrain the depositional age of the San Regis beds (Fig. 11). Sample SB19bg-123 is from the lower basaltic tephra channel fill at the 9-m vertical position in section SR23-1 and sample BH20bg-132 is from the capping basaltic andesite located ~200 m southwest of SR23-3 (Fig. 10). The age spectra display some complexity (Fig. 11). Sample BH20bg-132 shows a somewhat climbing pattern with initial steps near 3 Ma, followed by a generally flat section at about 3.6 Ma for about 70% of the spectrum with the final 20% of the spectrum climbing to about 4 Ma (Fig. 11A). Sample SB19bg-123 has an overall saddle-shaped spectrum with initial ages near 5 Ma and stepping down to flat section at about 4 Ma between 50 and 80% of gas released before climbing over the final 20% to ages near 5 Ma (Fig. 11B). The flat segments yield weighted mean dates of 3.695 ± 0.009 and 4.288 ± 0.036 Ma for BH20bg-132 and SB19bg-123, respectively (Figs. 11A, B). Isochron analysis indicates minor excess ^{40}Ar as trapped initial $^{40}Ar/^{36}Ar$ values are near 300 and thus elevated over the atmospheric value of 295.5 (Figs.

11C, D). The isochron age for BH20bg-132 is 3.635 ± 0.013 Ma based on greater than 90% of the step-heating data, whereas the final ca. 60% of gas release yields an isochron age of 4.097 ± 0.076 Ma for SB19bg-123 (Figs. 11C, D). The MSWD of 1.3 for BH20bg-132 indicates a normal distribution of data, whereas the MSWD of 6.3 for SB19bg-123 suggests some scatter that is not fully accounted for by the analytical errors. The isochron ages are the preferred eruption ages for these samples despite the slightly elevated MSWD for SB19bg-123.

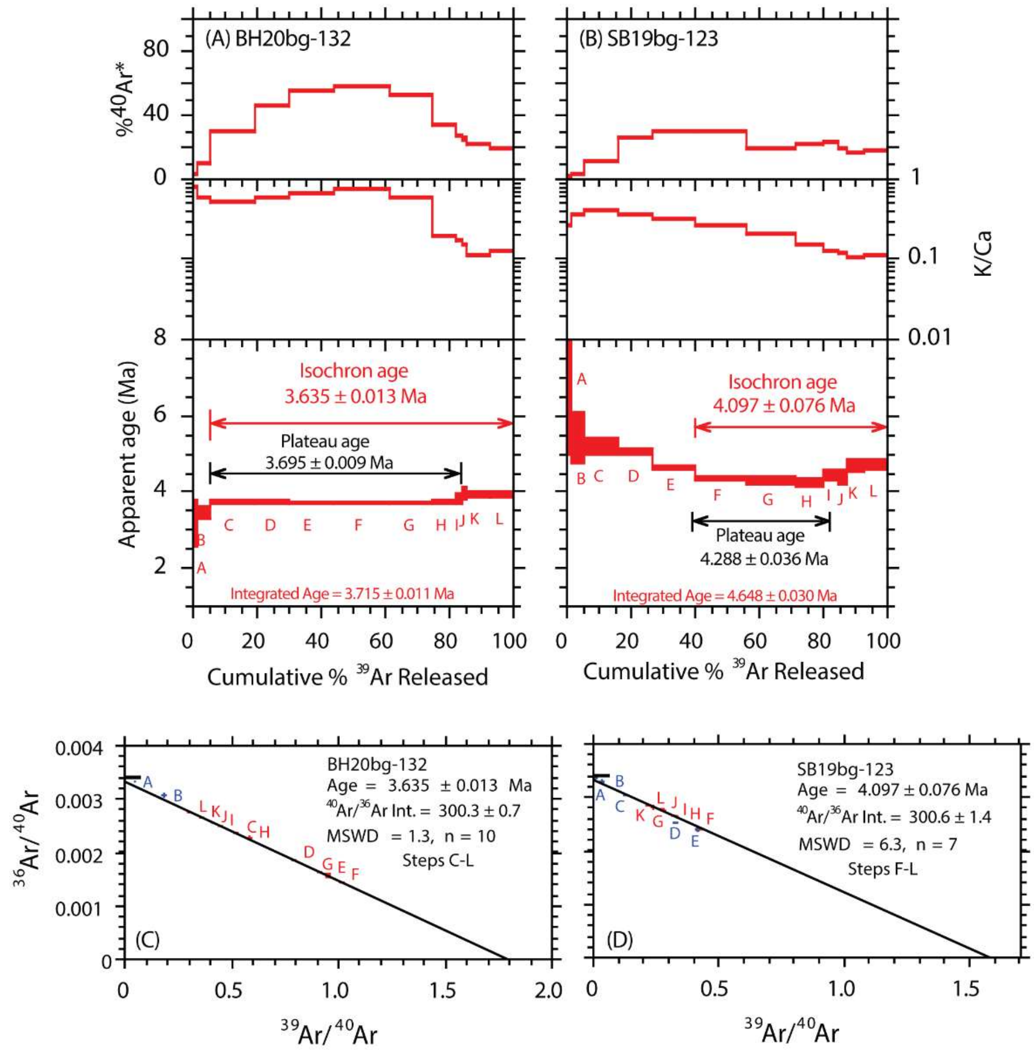

Figure 11. A, B) $^{40}Ar/^{39}Ar$ age spectrum, K/Ca and radiogenic yield diagrams; and C, D) isochron diagrams. The age spectra display some complexity that is principally explained by a minor excess argon, as shown by the isochron analysis that yields $^{40}Ar/^{39}Ar$ initial components near 300. Preferred eruption ages are given by the isochron results, and all errors are reported at 1s.

Composite Section

A ~30 m-thick composite stratigraphic section (Figure 12) was constructed by correlating and combining the four measured sections (Fig. 10), allowing changes in depositional environments and soil formation through time to be tracked. Sedimentary facies display subtle fining up-section from interbedded conglomerate and sandstone in the lower 5 m to primarily sandstone in the middle and upper parts of the ca. 30 m composite section (Fig. 12). The weak fining-up trend indicates a slight waning of paleocurrent strength through time, possibly due to lateral migration of the main channel away from the Mesa San Regis study site. Lithofacies record deposition in a sandy braided fluvial system, and the absence of major up-section changes in depositional environment indicate that the section accumulated in a stable persistent fluvial depositional system. Normally graded and massive sandstones are the most abundant lithofacies and show no major vertical change. Of the two reworked tephra deposits, only the lower tephra unit is shown in the composite section because the upper tephra is recorded in only one stratigraphic section and is laterally discontinuous (Fig. 10).

The composite section shows the main calcic paleosol horizons and inferred development stage (Fig. 12). All observed paleosols are likely aridisols (i.e., the number of consecutive days of water availability and temperature criteria for plants and carbonate accumulation is unknown), indicating that no major change in paleoclimate occurred during deposition of this section. The section reveals an overall up-section decrease in degree of soil development, from mature Stage III calcic horizons in the lower 10 m to primarily Stage I–II calcic horizons in the middle to upper San Regis beds, and a pronounced decrease in calcic horizons with prevalence of AB horizons of inceptisols in the uppermost 5 m of the San Regis beds (Fig. 12). The up-section decrease in abundance of well-developed calcic horizons may reflect changes in precipitation from arid to semiarid (dry to wet-dry) climate indicating fewer periods of prolonged aridity, an increase in effective precipitation (*cf.* Hasiotis *et al.,* 2025), and/or an increase in the frequency of flooding and higher sediment-accumulation rate resulting in fewer periods of prolonged nondeposition. The overall vertical change in paleosols indicates a minor shift from an arid to semiarid climate.

Celliforma and *Fictovichnus* are distributed through the composite section (Fig. 12), suggesting uniform floodplain habitats, consistent with deposition in a braided fluvial system as indicated by sedimentary facies and paleosol analysis. *Parawanichnus, Termitichnus,* and *Coprinisphaera* were only observed in the lower San Regis beds, though the prevalence of well-developed rhizocretions and variable carbonate brecciation may obscure these traces in upper parts of the section. One notable

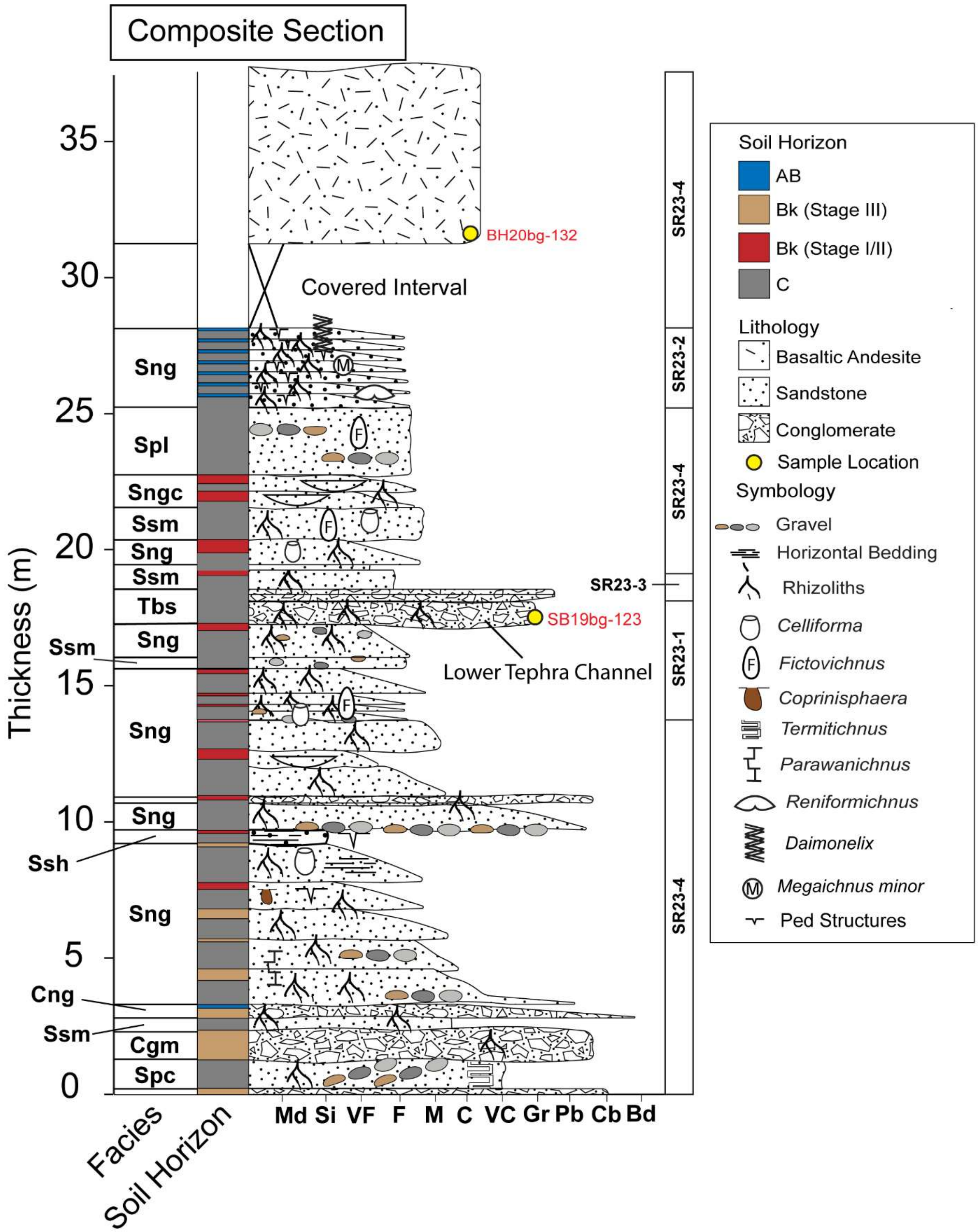

Figure 12. Composite stratigraphic section of the San Regis beds highlighting key lithofacies, Stage I-III calcic horizons, AB soil horizons, and trace fossils. There is little vertical change in facies assemblage, however, soil carbonate maturity does decrease up section.

vertical change in trace fossils is the occurrence of *Megaichnus, Reniformichnus,* and *Daimonelix* only in the uppermost 5 m of San Regis beds on the northern exposure where soil development is weak. Large tracemaker burrows were not observed elsewhere in the San Regis beds. Rhizoliths, rhizocretions, and rhizotubules are abundant and evenly distributed through the San Regis beds, suggesting the presence of well-established vegetation with minor changes in climate or similar climate under higher sediment accumulation rate as indicated by the distribution of calcic horizons (Fig. 12).

Paleosol-Age Analysis

Recognition of weakly to well-developed calcic paleosols in the San Regis beds (Fig. 12), integrated with $^{40}Ar/^{39}Ar$ ages of interbedded tephra and capping Mg-rich basaltic andesite, allows estimation of the timing and duration of deposition for the studied section. Soil formation times from similar calcic soils in nearby late Pleistocene sediments were applied to paleosols in the composite section (Fig. 12) to determine the total amount of time recorded in the ~30-m-thick San Regis beds. Schorr *et al.* (2018) performed optically stimulated luminescence (OSL) and cosmogenic exposure dating on calcic soils from late Pleistocene alluvial fans in Arroyo Santa Agueda and Arroyo Boleo, ~46 km SE of Mesa San Regis. They found that Stage II calcic horizons have an average formation age of 15 ± 3 ky, and Stage III calcic horizons represent 31 ± 9 ky. Since stage I and stage II horizons were grouped together in this study (Stage I–II), the 15-ky formation age was applied to this composite category (Figure 13). Paleosols with weakly developed profiles may be younger than this. The ages of calcic soil horizons from Schorr *et al.* (2018) are consistent with formation times for similar soils in Northern Mexico from Birkeland (1999), but are shorter than formation times for calcic soil horizons in southern California (Rockwell et al., 2019).

The composite section was simplified (Fig. 13A) and converted it into a time-stratigraphic section (Fig. 13B), assuming soil formation ages of Schorr *et al.* (2018) and incorporating our $^{40}Ar/^{39}Ar$ ages of the tephra channel and capping Mg-rich basaltic andesite. Data and analysis for paleosol horizons is available in supplementary file S2. This analysis of 20 calcic paleosol horizons indicates that the San Regis beds accumulated over a span of approximately 397 ± 111 ky. Deposition began at ~ 4.43 Ma and continued until ca. 4.04 Ma. Several meters of sediment above the highest well-developed calcic horizon are primarily AB and C horizons with no calcic horizons. No formation ages are attributable to this interval due to the lack of calcic horizons, and we assume

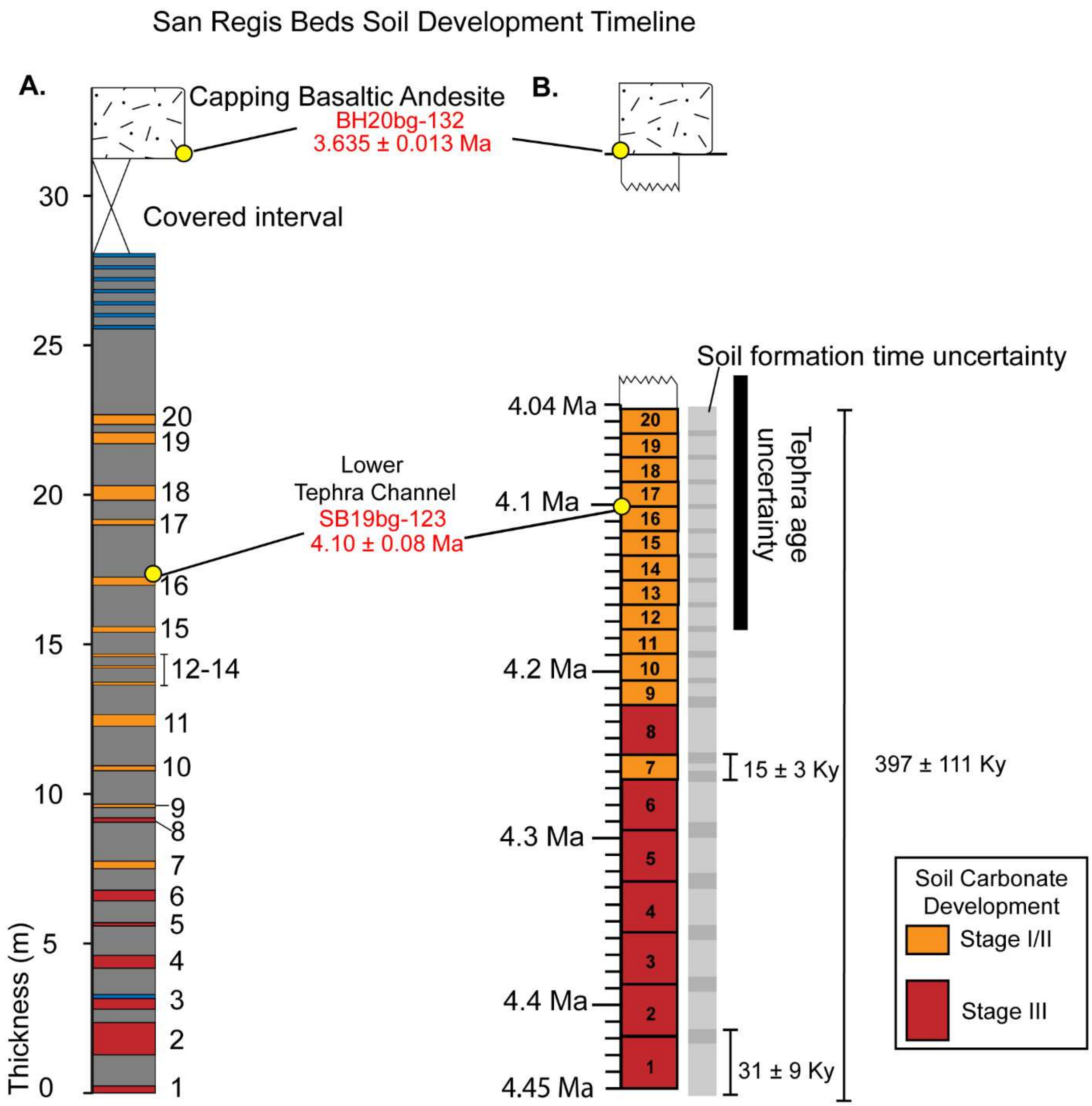

Figure 13. A) Composite measured section of the San Regis beds with carbonate paleosol horizons and development stage highlighted. Gray beds are non-paleosol intervals. (B) Composite temporal section showing estimated age range of the section using mean soil carbonate development times and $^{40}Ar/^{39}Ar$ ages for an interbedded tephra deposit. Light grey bars with darker overlapping regions represent the soil carbonate development time with uncertainties

that very little time is represented by these deposits that lack calcic paleosols. A time gap of 402 ± 77.3 ky was calculated between the youngest calcic soil horizon (4.04 ± 0.0762 Ma) and the mesa-capping basaltic andesite (3.635 ± 0.013 Ma) by propagating standard errors in quadrature. If the covered interval (~5 m) is assumed to represent a continuous and conformable section, it would imply that the upper 30% of San Regis beds accumulated over roughly the same time span as the lower 70%. This assumption would require a decrease in sediment accumulation rate and would predict an increase in soil maturity, which is inconsistent with the observed up-section decrease in soil maturity. Therefore, the base of the basaltic andesite is interpreted as an unconformity that spans most of the 402 ± 77.3 ky time gap between the highest exposed beds and the capping basaltic andesite (Fig. 13).

A plot of cumulative stratigraphic thickness vs. paleosol age (Figure 14) shows relatively uniform accumulation rate during deposition of the San Regis beds. The uncertainty of the tephra channel age (± 76 ky) is an order of magnitude larger than the uncertainty of the soil carbonate development times (± 3 ky, 9 ky) and thus represents the main uncertainty for ages of individual soil horizons. As a result, Gaussian standard error propagation of the uncertainties of the tephra age and

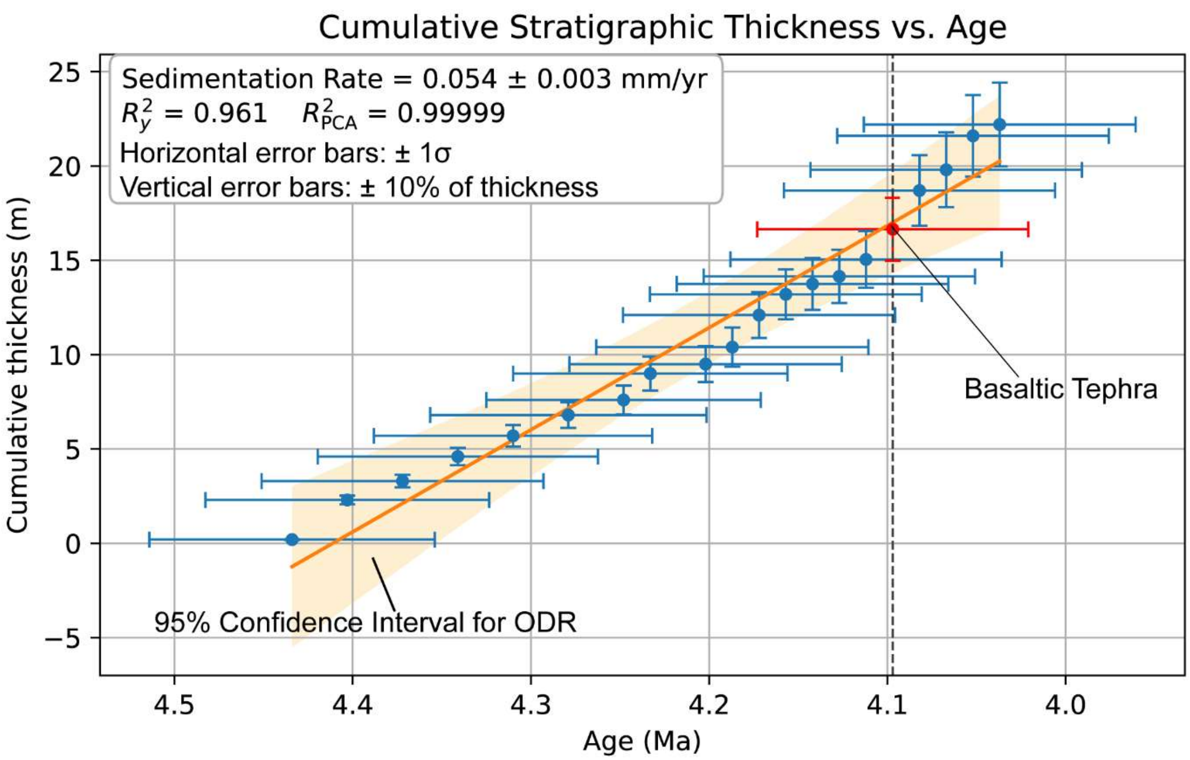

Figure 14. Cumulative stratigraphic thickness vs soil age for the San Regis beds. Thicknesses are the cumulative stratigraphic thickness at the top of each paleosol interval, and ages are calculated by adding or subtracting soil formation times (15 ± 3 Ka or 31 ± 9 Ka) from Paleosol #16 (Nearest age: Sample SB19bg-123; 4.097 ± 0.076 Ma) based on their stratigraphic order, and propagating the soil carbonate development uncertainties with the tephra age uncertainties. Orange line and highlighted area represent the Orthogonal Distance Regression (ODR) and the 95% confidence interval for the regression. The slope of the ODR gives a sedimentation rate of 0.054 ± 0.003 mm/yr. Dashed line at 4.1 Ma, red dot, and red error bars show the mean and uncertainty of the dated basaltic tephra

soil carbonate development times yields larger than expected uncertainties in the age of individual soil horizons. To account for residuals along the age axis due to age uncertainty, an orthogonal distance regression (ODR) was performed to determine the sedimentation rate. The best fit line yields a long-term average sedimentation rate of 0.054 ± 0.003 mm/yr, a slow accumulation rate that is consistent with the stratigraphic evidence for limited accommodation in the southwestern Baja California peninsula and San Ignacio trough (Dorsey *et al.*, 2024). To quantify the goodness of fit for the orthogonal distance regression, both the R^2_Y (0.961) and the R^2_{PCA} (0.999) were computed. The R^2_Y is functionally identical to the R^2 metric used in ordinary least squares regression, whereas the R^2_{PCA} represents the degree to which vertical and horizontal variations are explained by single principal component line. Both values indicate a robust fit for the orthogonal distance regression, with the R^2_{PCA} indicating that almost all variations fall along a single principal component line.

Discussion

Transpeninsular seaway hypothesis

The results of this study, combined with regional geologic constraints, provide a definitive test of the transpeninsular seaway hypothesis. These findings are reflected in a paleogeographic reconstruction of the central Baja California peninsula during deposition of the San Regis beds ~4.43–4.04 Ma (Figure 15A). Terrestrial sediments accumulated in an arid-climate, braided river system in the San Ignacio trough, between eroding Miocene volcanic centers to the NW and SE, which flowed southwest to a low-gradient coastal plain and shallow-marine shelf. The landscape was inundated with active high-Mg basaltic andesite volcanic cones and flows during this time (e.g., Benoit *et al.*, 2002; Calmus *et al.*, 2003; Pallares *et al.*, 2007). A marine connection across the central peninsula could not have existed prior to the initial marine flooding of the central Gulf of California at ca. 6.3 Ma (Darin *et al.*, 2025), which defines the earliest possible timeframe for any such seaway. On the western side of the proposed seaway near San Ignacio, the youngest exposed marine strata belong to the middle Miocene San Ignacio Formation, which is conformably overlain by continental fluvial-alluvial deposits of the middle to upper Miocene Atajo Formation (Fig. 2). This stratigraphic succession records fully emergent terrestrial conditions in the San Ignacio Trough from ca. 12 to 6 Ma, well before the earliest possible onset of marine flooding in the Gulf of California. This long-term record of continental deposition rules out the existence of a marine corridor through the San Ignacio region during Miocene time.

New evidence from the San Regis beds presented in this study further eliminates the possibility of a younger, Pliocene, or Pleistocene seaway in this region. Located near the center of the proposed seaway position, the Mesa San Regis section is characterized by fluvial deposits and abundant calcic paleosols and continental trace fossils that are clear indicators of terrestrial and

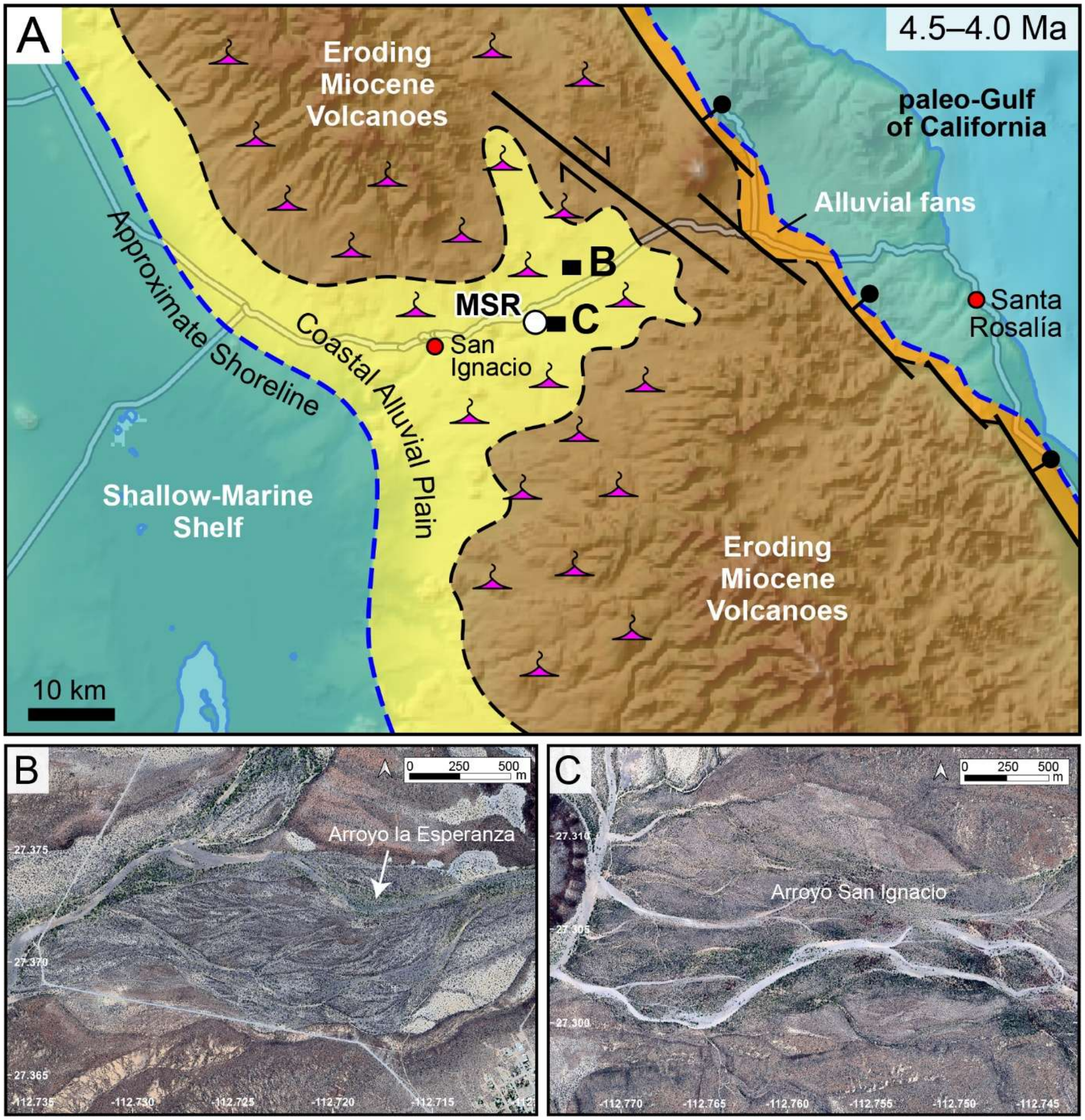

Figure 15. A) Paleogeographic reconstruction for the central Baja California peninsula during deposition of the San Regis beds ~ 4.43–4.04 Ma, with present-day topography, roads, and shoreline included for reference. Sediments accumulated in an arid-climate braided river system in the San Ignacio trough, between eroding Miocene volcanic centers to the NW and SE, that flowed southwest to a low-gradient coastal plain and shallow-marine shelf. The landscape was dotted with many active high-Mg basaltic andesite volcanic cones and flows (indicated schematically with small magenta cones). Black lines are inferred faults (from Bennett et al., 2025; Dorsey et al., in review); MSR is Mesa San Regis. Note locations of parts B and C. B) Satellite image of small braided channels and sparsely vegetated bars in the modern dryland river network northeast of Mesa San Regis. C) Satellite image of large, heavily vegetated bars southeast of Mesa San Regis. The present-day environment and depositional processes provide a good modern analogue for the paleoenvironment of the Pliocene San Regis beds.

freshwater environments between ca. 4.5 and 3.6 Ma. These deposits, along with overlying Quaternary alluvial gravel and sand in the San Ignacio Trough, reflect continued deposition in a low-gradient continental river system with no evidence for tidal currents, marine influence, or trace fossils typically associated with seaways (Steel et al., 2010; Olariu et al., 2012; Longhitano, 2013; O'Connell et al., 2020; Gardner & Dorsey, 2021).

Together, these constraints demonstrate that no viable transpeninsular marine connection existed through the San Ignacio region at any time during the Neogene or Quaternary periods, allowing the rejection of the transpeninsular seaway hypothesis as an explanation for observed patterns of genetic divergence at this latitude. Other possible drivers of the observed genomic divergence include climate-modulated glacial refugia, regional differences in rainfall patterns, and habitat fragmentation likely related to other climatic factors (e.g., Dolby *et al.,* 2022; Araya-Donoso *et al.,* 2022, 2024).

Paleoclimatic conditions

Abundant Stage I–II to Stage III Bk calcic paleosol horizons and the trace-fossil assemblages of the San Regis beds are all consistent with an arid to semiarid climate and well-drained soils formed in the vadose zone above the water table (Monger *et al.*, 1972; Hasiotis *et al.*, 2007; Genise *et al.*, 2010; Genise, 2017; Fischer & Hasiotis, 2018). The results show that conditions remained relatively constant for 397 ± 111 ky. The up-section decrease in soil carbonate maturity suggests a slight increase in sedimentation rate commensurate with less time for soil development or that the climate may have been more arid during deposition of the lower San Regis beds and became somewhat less arid through time, potentially due to an increase in seasonal precipitation. Increased precipitation may have resulted in more frequent sedimentation in active channels, as suggested by the lack of soil carbonate horizons in the upper San Regis beds. These same layers with immature soils also host the largest observed trace fossils: *Megaichnus minor, Daimonelix,* and *Reniformichnus*. The presence of these trace fossils only in this interval may suggest that climatic changes may also have driven changes in the habitability of the San Regis area for larger tracemakers, such that conditions became more suitable for large tracemakers during later stages of deposition.

Comparison to present-day depositional environments

Satellite imagery of Mesa San Regis and surrounding area shows the present-day fluvial system in Arroyo Hondo east of the mesa. The modern fluvial system has an overall westward transport direction, and the flow is locally deflected southward adjacent to Mesa San Regis. Fluvial bars and channels in small, braided channels of the modern fluvial system (Fig. 15B) resemble bars and shallow channels interpreted for the Regis beds. Larger channels and heavily vegetated bars in the modern system (Fig. 15B) provide a modern analog to overbank areas interpreted for the San Regis beds. Sedimentation is less frequent on these large bars, promoting development of more mature calcic soil horizons compared to active channel areas. The modern depositional system in the study area thus resembles the interpreted paleodepositional environment of the San Regis beds. This comparison, and the absence of any marine sedimentary sequences in post-4.5 Ma deposits of this area, indicates that alluvial drainage systems and trace-fossil assemblages have prevailed in the central Baja California peninsula since Miocene or Pliocene time (Carreno and Smith, 2007; Bennett *et al.,* 2025).

Conclusions

An analysis of sedimentology, paleopedology, and ichnology was applied to test the biologically inspired transpeninsular seaway hypothesis, which has been invoked for decades to explain genetic divergence between northern and southern populations of terrestrial plants and animals on the Baja California peninsula. The study site is located in the low-lying San Ignacio trough, where the seaway has been proposed. Results of this study show that the San Regis beds accumulated in a sandy braided fluvial system between ~4.43 and 4.04 Ma, over a time span of 397 ± 116 ky. Stage I–II to Stage III Bk soil horizons and trace fossils indicate that the paleoclimate was arid to semiarid with a possible increase in seasonal precipitation near the end of deposition. When integrated with regional geologic evidence, our results provide definitive evidence that no transpeninsular marine connection existed through the San Ignacio region during Neogene or Quaternary time. These results permit the rejection the transpeninsular seaway hypothesis as a driver of genetic divergence along the Baja California peninsula. Therefore, alternate hypotheses to explain the observed genomic pattern, such as glacial refugia, rainfall asynchrony, and habitat fragmentation, must be considered

Bridge

We identified relict, abandoned channels at elevations that closely correlate to Quaternary marine terraces in the Laguna San Ignacio Region (Ortlieb, 1991) with field verification of marine terrace deposits for one locality. The association of these channels with marine terraces raises the possibility that they may have been formed by tidal processes at sea level, and could potentially be used to reconstruct paleo-sea levels in the region. Similar relict channels globally could be used for this purpose as well. However, there exists no way to classify modern tidal and fluvial channels using their planform geometries, preventing classification of relict channels for this purpose. In Chapter III we develop a methodology to classify modern tidal and fluvial channels based on their planform geometry using trained machine-learning classifiers.

CHAPTER III: PLANFORM GEOMETRIC CLASSIFICATION OF FLUVIAL AND TIDAL CHANNELS VIA MACHINE LEARNING

This chapter includes previously published co-authored materials published as Gardner, K. K., & Dorsey, R. J. (2025). Planform geometric classification of fluvial and tidal channels via machine learning. *Earth Surface Processes and Landforms*, *50*(4). e70010 https://doi.org/10.1002/ESP.70010. Data collection, analysis, figure creation, and primary manuscript writing were completed by Kevin Gardner. Rebecca J. Dorsey aided in data interpretation and provided editorial feedback on figures and manuscript text.

Introduction

Channels are ubiquitous elements of fluvial and tidal systems that span a wide range of scales, shapes, and lengths (Figure 1). Channel planforms are the 2-dimensional top-down geometry which, in the simplest form, are described using width and curvature signals along a centerline (Vermeulen *et al.*, 2016). In fluvial settings, flow is unidirectional with variable discharge, reaching maximum discharge during floods (Leopold *et al.*, 1964; Lutscher *et al.*, 2007). Conversely, tidal settings are characterized by bimodal flows created by diurnal or semidiurnal flood and ebb tides where discharge is regular and reaches a maximum during fortnightly spring tides (Kvale *et al.*, 1995; Fagherazzi *et al.*, 2004; Hughes, 2012). Despite these differences in flow conditions, there is a significant overlap between the morphodynamics and geometries of tidal and fluvial channels.

Morphodynamic analyses of tidal and fluvial meanders reveal that tidal and fluvial channels display similar meander migration rates and meander cutoff behavior (Finotello *et al.*, 2018; Gao *et al.*, 2024). Width and meander wavelength of tidal channels exhibit the same linear correlation as fluvial meanders (e.g., Leopold et al., 1964), and the ratio of e-folding length for channel width to total channel length of tidal channels is similar to that of estuaries (Lanzoni & Seminara, 1998; Marani *et al.*, 2002; Lanzoni & D'Alpaos, 2015). Statistical analyses of meanders demonstrate that meander asymmetry is a key meander metric for differentiating channel types, and that principal component analyses of meander metrics are capable of grouping tidal and fluvial reaches (Fagherazzi *et al.*, 2004; Finotello *et al.*, 2020).

The general overlap of morphodynamics and planform characteristics in tidal and fluvial systems, while useful for understanding hydrodynamic processes, limits our ability to classify channels as tidal or fluvial based on planform geometry. True meanders have been defined as regions of a channel with a sinuosity index of 1.5 or greater (Leopold and Wolman, 1957). Many

Figure 1: Examples of tidal channels and digitized planforms in: A) Ganges-Brahmaputra, Bangladesh ; B) Brussa,Italy; and fluvial channels and digitized planforms of the C) Congaree River, South Carolina, USA; and D) Latorica River, Slovakia. Note the widening of the tidal channels in the seaward direction in A and B. Digitized banks shown by the white lines. Image Credits – Google Earth V 7.3.6.10201 – A: (1/11/2023) 45Q 783344.84 m E, 2441992.03 m N. Eye altitude: 67.72. Airbus, Maxar Technologies, TerraMetrics 2024, earth.google.com [10/8/2024]; B: (2/20/2024) 33T 342377.00 m E, 5056617.19 m N, Eye Altitude: 736 m. Airbus 2024, earth.google.com [10/8/2024] C: (6/14/2024) 17S 516492.90 m E, 3742013.75 m N, Eye altitude 29.78 km. Airbus 2024, earth.google.com [10/8/2024]; D: (6/12/2020) 34U 565715.29 m E, 5373520.49 m N, Eye altitude: 8.71 km. Eurosense/Geodis Slovakia 2024, earth.google.com [10/8/2024]

channel reaches have low sinuosity or broad bends that fall below this sinuosity threshold, where meander metrics do not provide the best representation. This is particularly relevant for analysis of relict channels where full or half meander geometries are not always preserved, or in cases where the relict channel has low sinuosity making application of meander metrics difficult. Multi-variate statistical analysis of meander metrics can effectively cluster longer channel reaches by channel type (Finotello et al. 2020) but this method requires the presence and delineation of meanders. Currently there is no system for classifying whole channel reaches as tidal versus fluvial that are not based on extraction of meander metrics.

Machine-learning (ML) algorithms are capable of classifying inputs based on patterns in large, high-dimensional datasets that may not be apparent using other types of analyses. These algorithms have been successfully applied to remote sensing, well log data, seismology, mining, and geologic mapping (Evans *et al.*, 1986; Kong *et al.*, 1988; Lee *et al.*, 1994; Cracknell & Reading, 2014; Keshtkar *et al.*, 2017; Corbi *et al.*, 2019; Bressan *et al.*, 2020; Parikh *et al.*, 2020; El Fels & El Ghorfi, 2022; Murti *et al.*, 2022; Wang *et al.*, 2024). To date, however, ML methods have not been used in analysis of channel planform geometries to classify channel reaches as tidal or fluvial.

This study uses geometric analysis integrated with machine learning applied to a limited set of channel metrics to classify channels as tidal or fluvial. Our dataset consists of 63 tidal (n = 46) and fluvial (n = 17) channels from a variety of climates, tidal ranges, channel sizes (≈ channel width), and 144 statistical variables that describe normalized width (NW), normalized curvature (NC), normalized radius of curvature (NR), NC/NW, convolutions of NR and NC with NW, and their derivatives. We find that dimension-reduction techniques such as linear discriminant analysis are not capable of classifying channel type based on discriminant scores. We compare the performance of three common machine-learning classification algorithms (Multi-layer Perceptron, Random Forest, and Logistic Regression) and develop thresholds for classifying individual channels as tidal or fluvial using segment-scale output of ML classifiers with reach-scale accuracies up to 100%. This method allows us to classify channels with easily extracted data from inaccessible regions on Earth and has potential for interpreting the origin of relict channels on inactive geomorphic surfaces. Our results show that machine-learning algorithms, particularly Random Forest classifiers, are highly accurate for classifying entire channel reaches.

Methods

Methods used in this study can be grouped into six components: (1) digitize channel and extract a centerline; (2) calculate along-channel metrics; (3) extract statistics and segment the data; (4) train classification algorithms; (5) apply classifiers to the reach scale; and (6) Linear Discriminant Analysis (LDA). Figure 2 is a flowchart showing the complete workflow, from channel digitization to evaluation of performance for each classifier at the reach scale. The data, results, and python functions used in this study are available in the Supplementary Files S1-S6

Channel bank digitization and centerline extraction

Metrics for local channel width and curvature along a channel centerline are needed to fully capture the planform geometry of a channel reach (e.g., Vermeulen et al., 2016). We used digitized channel banks to extract a centerline along the channel reach and measure width transects across the centerline. We digitize banks of channels at bank-full geometries in Google Earth as line objects from downstream to upstream. Nearly all channels digitized had distinct vegetation lines that we

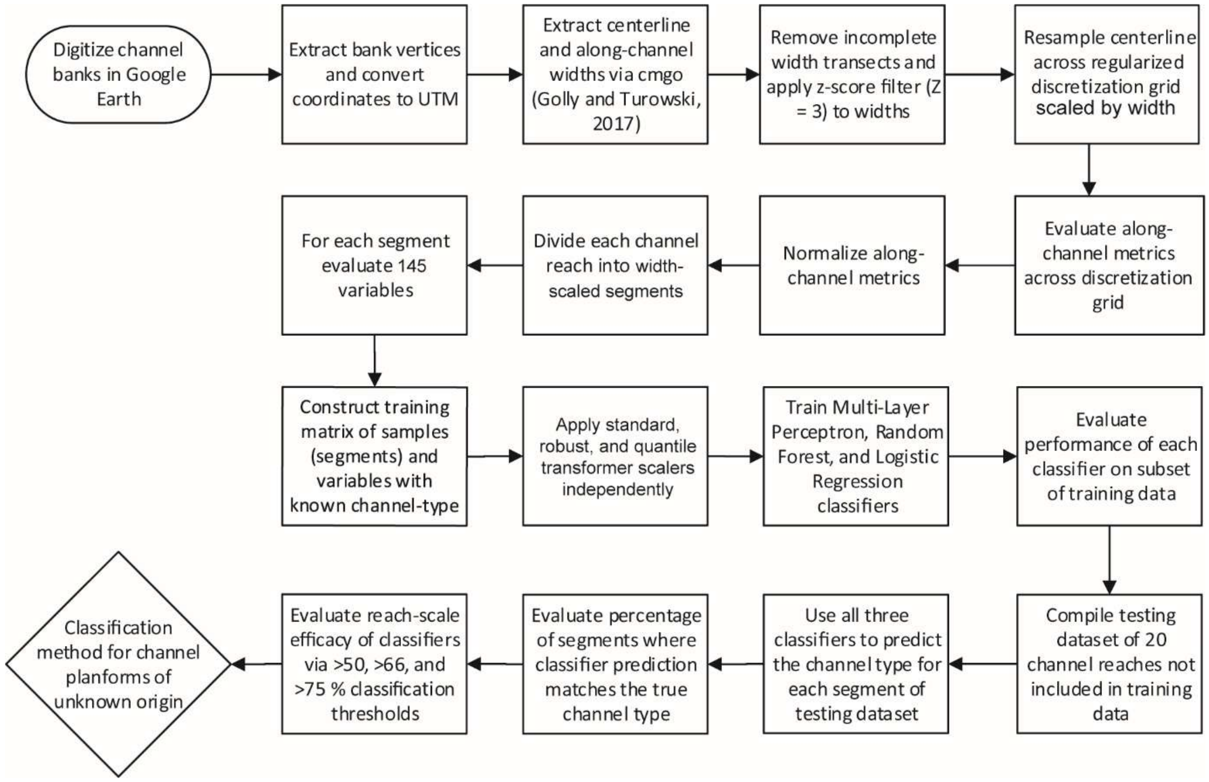

Figure 2. Flowchart illustrating the workflow for digitizing channels, extracting channel metrics, preparing datasets for input into machine-learning algorithms, training and evaluating classifier performances, and classifying at the reach scale.

used to delineate the channel banks. In instances where vegetation was sparse, we delineated banks by clear breaks in slope on levees, manmade structures on banks, or temporal satellite imagery directly showing bankfull conditions. If channel banks could not be clearly delineated, we would select another location with clearly defined banks. We digitized channel reaches on all continents except Antarctica, cover a range of channel sizes with widths ranging from meters to hundreds of meters, and tidal ranges from micro- to macro-tidal. We then extract the coordinates of each vertex, convert them to UTM, and compile coordinates in a text file containing all bank vertices and bank-side identifiers for a given channel. To extract a centerline, we implement the R package "CMGO" (Golly & Turowski, 2017). This program uses Voronoi tessellation of channel bank vertices to establish points along the channel centerline and smooth high-frequency noise to create a smoothed centerline. At each point along the centerline, a transect perpendicular to the centerline gives the full channel width. The output of this extraction includes the coordinates of channel centerline points, distance along the channel centerline, and channel width at each point.

Calculate along-channel metrics

To ensure consistent measurements along a channel centerline for channels of different sizes, we re-sample the centerline across a regular discretization grid that is scaled to channel width (Fagherazzi *et al.*, 2004; Finotello *et al.*, 2020). We evaluate cubic spline representations of latitude, longitude, and width (w(s)) vs distance upstream at spacing equal to $1/100^{th}$ the average width of the channel reach on a discretization grid. Scaling of the discretization grid is necessary for the comparison of channels of different size and width (e.g., Finotello et al., 2024). Curvature at each point is calculated using equation 2 of Marani et al., (2002):

$$(1) \qquad c(s) = \frac{(dx/ds)(d^2y/ds^2) - (dy/ds)(d^2x/ds^2)}{[(dx/ds)^2 + (dy/ds)^2]^{3/2}}$$

where c(s) is the local channel curvature at each point along the centerline, s; x and y are longitude and latitude; $dx/ds, dy/ds, d^2x/ds^2$, and d^2y/ds^2 are the first and second derivatives of x and y with respect to distance along the channel (s). Using the local channel curvature at each point, we can evaluate the local radius of curvature using the following equation:

$$(2) \qquad R(s) = \frac{1}{|c(s)|}$$

where R(s) is the radius of curvature at each point s, evaluated by taking the inverse of the absolute value of curvature at that point. To compare channels of different scales to one another, the data are normalized using the following equations:

$$(3) \qquad NW(s) = {}^{W(s)}/_{\overline{W}}$$

$$(4) \qquad NC(s) = C(s) * \overline{W}$$

$$(5) \qquad NR(s) = {}^{R(s)}/_{\overline{W}}$$

where NW(s), NC(s), and NR (s) are normalized width, normalized curvature, and normalized radius of curvature at each point; and $\overline{W}, \bar{C}$ are the average width and average curvature for the entire channel reach. Finotello et al. (2020) normalized width against average width of the meander rather than the entire reach. While this method keeps variables directly related to meanders, the broader context relative to the rest of the channel reach is lost. In tidal channels that exhibit unique funneling in the downstream direction (Marani *et al.*, 2002; Lanzoni & D'Alpaos, 2015), our approach of normalizing channel width relative to the reach-averaged width allows us to capture width anomalies that would otherwise be lost if width values were normalized to the average width of a segment, as is necessary when using meander-based metrics and segmentation. Similarly, normalizing curvature to the average curvature of the entire reach provides spatial context that would be lost if curvature was normalized against local averages.

In addition, we calculated the convolution of normalized curvature and normalized radius of curvature with width. Convolving the signals provides a measure of the effect that channel width has on curvature and radius of curvature. The discrete linear convolution is described by the equations:

$$(6) \qquad NCxNW(s) = \sum_{m=0}^{i} NC_m NW_{s-m}$$

$$(7) \qquad NRxNW(s) = \sum_{m=0}^{i} NR_m NW_{s-m}$$

where NCxNW and NRxNW are the convolutions of normalized curvature and normalized radius of curvature with normalized width, m is the point along the NC or NR signal, i is the end point of the signal, and S is the point along the width signal. To better capture how geometry changes along the centerline, we also calculate the first derivative with respect to s for normalized width, normalized curvature, normalized radius of curvature, NCxNW, and NRxNW. Additionally, we utilize the simple quotient of normalized curvature and normalized width, given by the equation:

$$(8) \qquad NC/NW = \frac{NC}{NW}$$

where NC/NW is the normalized curvature to normalized width ratio, NC is normalized curvature, and NW is normalized width. At this step, each point along the centerline of each channel reach has a measure of normalized width, normalized curvature, normalized radius of curvature, normalized curvature convolved with normalized width, normalized radius of curvature convolved with normalized width, the first derivatives of these signals. These metrics provide the basis for all statistical analyses and variables used in the training and testing datasets.

Extract statistics and segment the data

Each channel reach is divided into uniform segments, where each segment is treated as an individual sample described by statistical measures of NW, NC, NR, NCxNW, NRxNW, and NC/NW. Segmentation is necessary to capture local geometric details that may be important for distinguishing tidal versus fluvial channel types, though choosing a segment size that is too small may result in overfitting to high-frequency noise that inhibits classification. Many tidal channels are short (~ 1 km), which means assigning segments that are too long results in loss of local detail. This requires more tidal channels to be digitized to achieve a balance in the number of segments from fluvial and tidal channels. In this study, we divide all channel reaches into segments scaled to double the average channel width, to maximize coverage of tidal channels and minimize overfitting of noise on larger channels. This approach is different from previous studies which segmented channels based on the delineation of individual meander bends.

For each channel segment we calculate thirteen statistical variables (Table 1). For each of the eleven along-channel metrics (NC/NW, NW, NC, NR, NCxNW, NRxNW, NW', NC', NR', NCxNW', NRxNW') we calculate the mean, variance, standard deviation, minimum, maximum, median, midpoint, skewness, kurtosis, range, mean absolute deviation, intra-quartile range, and mode. In addition to these 143 statistical variables, we also calculate the sinuosity of each channel segment for a total of 144 variables with the following equations:

$$(9) \quad L_c = \sqrt{\left(x_{last} - x_{first}\right)^2 + \left(y_{last} - y_{first}\right)^2}$$

$$(10) \quad SI = \frac{L_s}{L_c}$$

where L_c is the cartesian distance between the first and last points in the segment, x and y are the longitude and latitude of the first and last points, L_s is the intrinsic distance along the centerline of the segment, and SI is the sinuosity index. This provides a measure of the degree to which a particular segment is meandering or straight.

We completed this process for tidal (n = 46) and fluvial channels (n = 17) that were used to train and evaluate the classifiers, and to 20 additional tidal (n =10) and fluvial channels (n = 10) used to test the accuracy of the classifiers at the reach scale. The final training dataset contains 4294 fluvial and tidal channel segments, each with 144 variables describing their geometries and class labels (tidal or fluvial). The training and testing tables are in supplementary files S1 and S2, respectively. The data processing python functions used in this study are in Supplementary File S3.

Table 1. Principal along-channel metrics and the statistical variables for each metric used to train the classifiers. d/ds = first derivative of metric with respect to distance upstream (s); Mid = Midpoint; Me = Median; MAD = Mean Absolute Deviation; IQR = Intra-Quartile Range, γ = skewness; κ = kurtosis; SI = Sinuosity Index

Metric	Variables
NC/NW	$\overline{\mathrm{NC/NW}}$, $\boldsymbol{\sigma}_{\mathrm{NC/NW}}$, $\boldsymbol{\sigma}^2_{\mathrm{NC/NW}}$, $\boldsymbol{Min}_{\mathrm{NC/NW}}$, $\boldsymbol{Max}_{\mathrm{NC/NW}}$, $Mid_{\mathrm{NC/NW}}$, $\boldsymbol{Me}_{\mathrm{NC/NW}}$, $\boldsymbol{\gamma}_{\mathrm{NC/NW}}$, $\boldsymbol{\kappa}_{\mathrm{NC/NW}}$, $\mathrm{Range}_{\mathrm{NC/NW}}$, $\mathrm{MAD}_{\mathrm{NC/NW}}$, $\mathrm{IQR}_{\mathrm{NC/NW}}$, $\mathrm{Mode}_{\mathrm{NC/NW}}$
NW	$\overline{\mathrm{NW}}$, $\boldsymbol{\sigma}_{\boldsymbol{NW}}$, $\boldsymbol{\sigma}^2_{\boldsymbol{NW}}$, $\boldsymbol{Min}_{\boldsymbol{NW}}$, $\boldsymbol{Max}_{\boldsymbol{NW}}$, $Mid_{\boldsymbol{NW}}$, $\boldsymbol{Me}_{\boldsymbol{NW}}$, $\boldsymbol{\gamma}_{\boldsymbol{NW}}$, $\boldsymbol{\kappa}_{\boldsymbol{NW}}$, $\mathrm{Range}_{\boldsymbol{NW}}$, $\mathrm{MAD}_{\boldsymbol{NW}}$, $\mathrm{IQR}_{\boldsymbol{NW}}$, $\mathrm{Mode}_{\boldsymbol{NW}}$
NC	$\overline{\mathrm{NC}}$, $\boldsymbol{\sigma}_{\boldsymbol{NC}}$, $\boldsymbol{\sigma}^2_{\boldsymbol{NC}}$, $\boldsymbol{Min}_{\boldsymbol{NC}}$, $\boldsymbol{Max}_{\boldsymbol{NC}}$, $Mid_{\boldsymbol{NC}}$, $\boldsymbol{Me}_{\boldsymbol{NC}}$, $\boldsymbol{\gamma}_{\boldsymbol{NC}}$, $\boldsymbol{\kappa}_{\boldsymbol{NC}}$, $\mathrm{Range}_{\boldsymbol{NC}}$, $\mathrm{MAD}_{\boldsymbol{NC}}$, $\mathrm{IQR}_{\boldsymbol{NC}}$, $\mathrm{Mode}_{\boldsymbol{NC}}$
NR	$\overline{\mathrm{NR}}$, $\boldsymbol{\sigma}_{\boldsymbol{NR}}$, $\boldsymbol{\sigma}^2_{\boldsymbol{NR}}$, $\boldsymbol{Min}_{\boldsymbol{NR}}$, $\boldsymbol{Max}_{\boldsymbol{NR}}$, $Mid_{\boldsymbol{NR}}$, $\boldsymbol{Me}_{\boldsymbol{NR}}$, $\boldsymbol{\gamma}_{\boldsymbol{NR}}$, $\boldsymbol{\kappa}_{\boldsymbol{NR}}$, $\mathrm{Range}_{\boldsymbol{NR}}$, $\mathrm{MAD}_{\boldsymbol{NR}}$, $\mathrm{IQR}_{\boldsymbol{NR}}$, $\mathrm{Mode}_{\boldsymbol{NR}}$
NCxNW	$\overline{\mathrm{NCxNW}}$, $\boldsymbol{\sigma}_{\boldsymbol{NCxNW}}$, $\boldsymbol{\sigma}^2_{\boldsymbol{NCxNW}}$, $\boldsymbol{Min}_{\boldsymbol{NCxNW}}$, $\boldsymbol{Max}_{\boldsymbol{NCxNW}}$, $Mid_{\boldsymbol{NCxNW}}$, $\boldsymbol{Me}_{\boldsymbol{NCxNW}}$, $\boldsymbol{\gamma}_{\boldsymbol{NCxNw}}$, $\boldsymbol{\kappa}_{\boldsymbol{NCxNW}}$,

Metric	Variables
	Range$_{NCxNW}$, MAD$_{NCxNW}$, IQR$_{NCxNW}$, Mode$_{NCxNW}$
NRxNW	$\overline{\text{NRxNW}}$, $\boldsymbol{\sigma_{NRxNW}}$, $\boldsymbol{\sigma^2_{NRxNW}}$, $\boldsymbol{Min_{NRxNW}}$, $\boldsymbol{Max_{NRxNW}}$, Mid_{NRxNW}, $\boldsymbol{Me_{NRxNW}}$, $\boldsymbol{\gamma_{NRxNW}}$, $\boldsymbol{\kappa_{NRxNW}}$, Range$_{NRxNW}$, MAD$_{NRxNW}$, IQR$_{NRxNW}$, Mode$_{NRxNW}$
$\boldsymbol{dNW/ds}$ (NW')	$\overline{\text{NW'}}$, $\boldsymbol{\sigma_{NW'}}$, $\boldsymbol{\sigma^2_{NW'}}$, $\boldsymbol{Min_{NW'}}$, $\boldsymbol{Max_{NW'}}$, $Mid_{NW'}$, $\boldsymbol{Me_{NW'}}$, $\boldsymbol{\gamma_{NW'}}$, $\boldsymbol{\kappa_{NW'}}$, Range$_{NW'}$, MAD$_{NW'}$, IQR$_{NW'}$, Mode$_{NW'}$
$\boldsymbol{dNC/ds}$ (NC')	$\overline{\text{NC'}}$, $\boldsymbol{\sigma_{NC'}}$, $\boldsymbol{\sigma^2_{NC'}}$, $\boldsymbol{Min_{NC'}}$, $\boldsymbol{Max_{NC'}}$, $Mid_{NC'}$, $\boldsymbol{Me_{NC'}}$, $\boldsymbol{\gamma_{NC'}}$, $\boldsymbol{\kappa_{NC'}}$, Range$_{NC'}$, MAD$_{NC'}$, IQR$_{NC'}$, Mode$_{NC'}$
$\boldsymbol{dNR/ds}$ (NR')	$\overline{\text{NR'}}$, $\boldsymbol{\sigma_{NR'}}$, $\boldsymbol{\sigma^2_{NR'}}$, $\boldsymbol{Min_{NR'}}$, $\boldsymbol{Max_{NR'}}$, $Mid_{NR'}$, $\boldsymbol{Me_{NR'}}$, $\boldsymbol{\gamma_{NR'}}$, $\boldsymbol{\kappa_{NR'}}$, Range$_{NR'}$, MAD$_{NR'}$, IQR$_{NR'}$, Mode$_{NR'}$
$\boldsymbol{dNCxNW/ds}$ (NCxNW')	$\overline{\text{NCxNW'}}$, $\boldsymbol{\sigma_{NCxNW'}}$, $\boldsymbol{\sigma^2_{NCxNW'}}$, $\boldsymbol{Min_{NCxNW'}}$, $\boldsymbol{Max_{NCxNW'}}$, P$_{NCxNW'}$, $\boldsymbol{Me_{NCxNW'}}$, $\boldsymbol{\gamma_{NCxNW'}}$, $\boldsymbol{\kappa_{NCxN}}$ Range$_{NCxNW'}$, MAD$_{NCxNW'}$, IQR$_{NCxNW'}$, Mode$_{NCxNW'}$
$\boldsymbol{dNRxNW/ds}$ (NRxNW')	$\overline{\textbf{NRxNW'}}$, $\boldsymbol{\sigma_{NRxNW'}}$, $\boldsymbol{\sigma^2_{NRxNW'}}$, $\boldsymbol{Min_{NRxNW'}}$, $\boldsymbol{Max_{NRxNW'}}$, $Mid_{NRxNW'}$, $\boldsymbol{Me_{NRxNW'}}$, $\boldsymbol{\gamma_{NRxNW'}}$, $\boldsymbol{\kappa_{NI}}$ Range$_{NR'xNW'}$, MAD$_{NRxNW'}$, IQR$_{NRxNW'}$, Mode$_{NRxNW'}$
Sinuosity	SI

Train classification algorithms

To determine the most effective machine-learning algorithm, we trained and tested three different supervised classification algorithms using the scikit-learn package in Python: Logistic Regression, Multi-layer Perceptron, and Random Forest (Pedregosa *et al.*, 2011). The Logistic Regression (LR) classifier is a simple classifier that creates a linear combination of variables, passes it through a sigmoid function, and returns the probability of it being one class or the other (McCullagh, 2019). LR classification has been successfully implemented for land cover classification using multispectral data (Das & Pandey, 2019). The Multi-layer Perceptron (MLP) is a form of neural network that takes the input variables, connects them to a pre-defined structure of layered nodes where it determines connection weights between layers, and outputs the predicted class nodes. The MLP algorithm then compares its predictions to the true values, and adjusts the node connection weights via backpropagation and stochastic optimization to determine the optimal weights with the highest accuracy (Hinton, 1990; Kingma & Ba, 2014). Random Forest classifiers are comprised of bootstrap aggregated decision trees (Figure 3) where each node at a split is chosen based on the greatest split between the classes, and the final output of the classifier is democratically chosen by all individual trees via majority vote (Breiman, 2001).

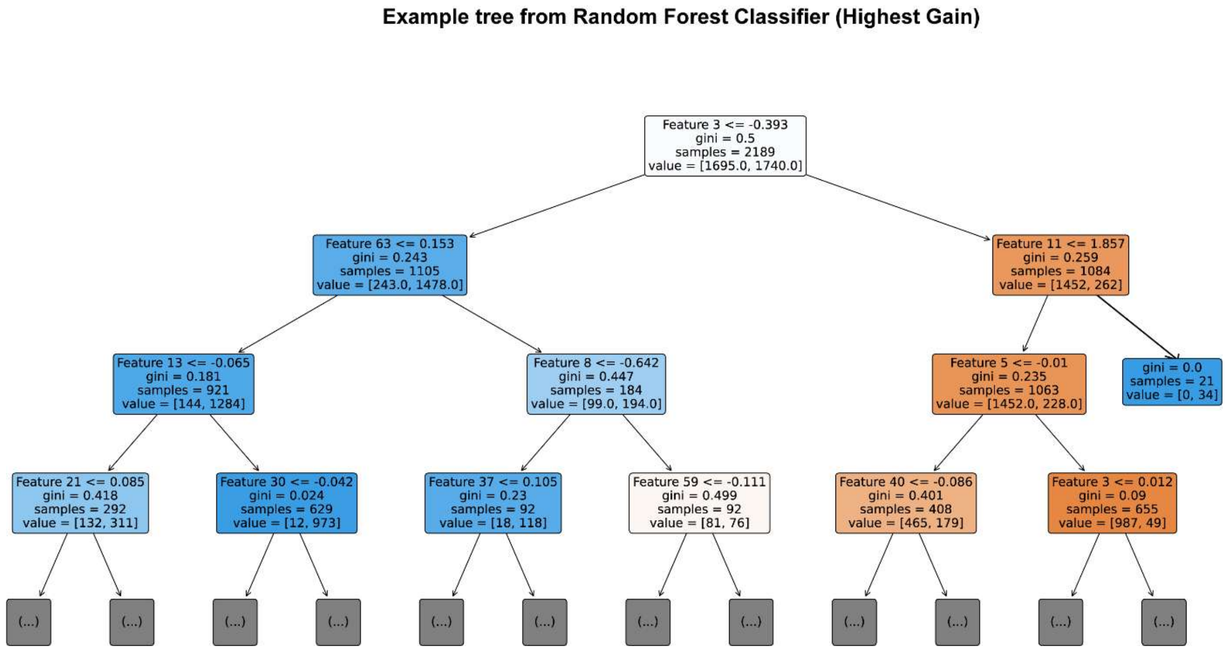

Figure 3. Example tree from the Random Forest Classifier chosen by highest gain levels. Blue leaves are dominated by tidal samples while red/orange leaves are dominated by fluvial samples. Each leaf represents a feature variable and threshold values. Only 3 full levels are shown. Nodes on the far right exemplify end results of purely tidal or purely fluvial nodes.

Prior to training we defined the structure the Multi-layer Perceptron where each hidden layer has half the number of nodes (rounded to the nearest integer) of the preceding layer. (Kingma and Ba, 2014). The number of hidden layers is determined by the last hidden layer to have more than 2 nodes. We applied an alpha of 0.001, the rectified linear unit activation function and the *adam* stochastic optimization solver to the MLP model (e.g., Kingma & Ba, 2014). The Random Forest classifier was structured with 100 decision trees in the forest, using gini impurity to determine the split quality. We applied the 'sag' solver, which is well suited for large datasets with binary labels. Each classifier was trained on the training dataset of 4294 tidal and fluvial segments, where 80% of the data was used to train the models and the remaining 20% was reserved for testing segment-scale accuracy. Testing parameters used are in Supplementary File S4

Apply classifiers to the reach scale

Each of the classifiers above was trained to classify channels at the segment scale, thus giving the classifiers enough geometric data to provide robust classifications. However, classifying a single segment is not sufficient to classify an entire reach as tidal versus fluvial. The classification of all segments within a reach must also be considered to classify the full reach. To address this, we implemented three classification thresholds that represent the percent of segments in a reach needed to classify the channel as tidal or fluvial: >50%, >66%, and >75%. In all cases, the dominant segment type determines the channel type, but the majority needed increases with increased classification threshold. To assess the efficacy of each classifier at these thresholds, we presented the trained models with a separate dataset of ten tidal and ten fluvial channel reaches prepared identically to our training dataset. The models classify all segments within a reach as either tidal or fluvial. For each channel reach, we evaluate the number of tidal segments and fluvial segments and classify the reach as the dominant channel type determined at each threshold. The accuracy of a classifier is determined by the percent of reaches that were correctly classified (e.g., tidal reach was classified as tidal). The classifier that had the highest overall reach-scale accuracy and the smallest decrease in accuracy with an increased classification threshold was considered to be the best performing.

To maximize performance of the classifiers at the reach scale, we performed 69 training trials on each classifier. We organized variables that were included in each trial into 23 different configurations ranging from all the variables to only small subsets of the data (Table 2), and ran each metric configuration through three different scalers in the scikit-learn library: standard scaler (parametric), robust scaler (non-parametric), and quantile transformer (non-parametric) (Pedregosa *et al.*, 2011). By adjusting these two parameters we can understand the effects of different groupings of data on the performance of these classifiers. This approach also reveals how the different combinations are affected by parametric and non-parametric scaling.

Table 2. 23 Principal along channel metric configurations used in this study. MC = Metric configurations. Y indicates statistical variables of that metric are included, N indicates statistical variables of that metric are not included.

MC	NC/NW	NW	NC	NR	NCxNW	NRxNW	NW'	NC'	NR'	NCxNW'	NRxNW'	SI
1	Y	Y	Y	Y	Y	Y	Y	Y	Y	Y	Y	Y
2	Y	Y	Y	Y	Y	Y	Y	Y	Y	Y	Y	N
3	N	Y	Y	Y	Y	Y	Y	Y	Y	Y	Y	Y
4	N	Y	Y	Y	Y	Y	Y	Y	Y	Y	Y	N
5	Y	Y	Y	Y	Y	Y	N	N	N	N	N	Y
6	N	Y	Y	Y	Y	Y	N	N	N	N	N	Y
7	N	Y	Y	Y	Y	Y	N	N	N	N	N	N
8	Y	N	N	N	N	N	Y	Y	Y	Y	Y	Y
9	Y	N	N	N	N	N	Y	Y	Y	Y	Y	N
10	N	N	N	N	N	N	Y	Y	Y	Y	Y	N
11	N	N	N	N	N	N	Y	Y	Y	Y	Y	Y
12	Y	N	N	N	Y	Y	N	N	N	Y	Y	Y
13	Y	N	N	N	Y	Y	N	N	N	Y	Y	N
14	N	N	N	N	Y	Y	N	N	N	Y	Y	N
15	N	N	N	N	Y	Y	N	N	N	Y	Y	Y

MC	NC/NW	NW	NC	NR	NCxNW	NRxNW	NW'	NC'	NR'	NCxNW'	NRxNW'	SI
16	Y	Y	Y	N	Y	N	Y	Y	N	Y	N	Y
17	Y	Y	Y	N	Y	N	Y	Y	N	Y	N	N
18	N	Y	Y	N	Y	N	Y	Y	N	Y	N	N
19	N	Y	Y	N	Y	N	Y	Y	N	Y	N	Y
20	Y	Y	N	Y	N	Y	Y	N	Y	N	Y	Y
21	Y	Y	N	Y	N	Y	Y	N	Y	N	Y	N
22	N	Y	N	Y	N	Y	Y	N	Y	N	Y	N
23	N	Y	N	Y	N	Y	Y	N	Y	N	Y	Y

Linear Discriminant Analysis (LDA)

A simple form of supervised classification is linear discriminant analysis (LDA). Given classified data and variables, LDA transforms data to maximize between-class variance and minimize within-class variance. In doing so, the LDA creates the greatest possible separation between the discriminant scores of each group. Discriminant scores are best used to classify data when a clear threshold score is defined that separates the classes. We performed a linear discriminant analysis on our training dataset of 4294 fluvial and tidal channel segments, and the results are presented below.

Results

Linear Discriminant Analysis

Figure 4 shows the frequency distribution and violin plots of discriminant scores for fluvial and tidal channel segments. The range of discriminant score values overlaps significantly for the two groups, which means there is no threshold discriminant score with which to separate the groups. The discriminant scores for fluvial channel segments do not exceed 2, whereas there are several tidal channel segments that are above this score, suggesting that segments with scores above this can be classified as tidal. However, results of the Linear Discriminant Analysis are not sufficient to classify channel segments as tidal or fluvial, prompting the need for more powerful classifiers.

Segment-scale Classifier Performance

The classifiers used in this study operate at the segment scale $(L_S = 2\overline{W})$, where L_s is the segment length for a given channel and $\overline{W}$ is the average width of the channel, and therefore the most direct assessment of the classifiers is their accuracy in classifying segments. Across 69 trials the Logistic Regression classifier performed the worst, with accuracies ranging from 64% to 90% (mean

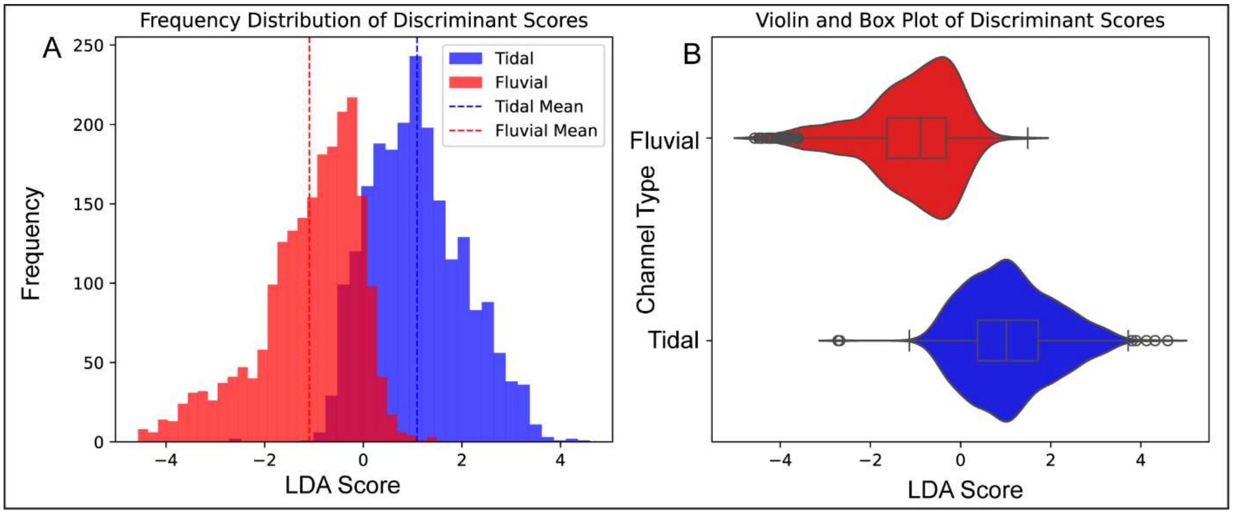

Figure 4. Plots of discriminant scores for tidal and fluvial segments derived from linear discriminant analysis. A) Frequency distribution and means for tidal and fluvial discriminant scores; B) Combined violin and box plots for tidal and fluvial discriminant scores displaying overlap of the intraquartile range for both distributions, and a larger number of outliers for the tidal distribution. There is considerable overlap between the two populations. The distribution of fluvial discriminant scores is negatively skewed while the distribution of tidal discriminant scores is positively skewed. No clear threshold score for differentiating between the groups could be identified.

= 80%). The Multi-layer Perceptron classifier performed significantly better than the Logistic Regression classifier, with accuracies ranging from 82% to 95% (mean = 89%). The best and most consistent performance across all trials was the Random Forest classifier with segment-scale accuracies between 89% and 97% (mean = 93%) (See Supplementary File S5)

Figure 5 shows important segment-scale performance metrics for the Random Forest classifier that performed the best at the reach scale (trial 58). The confusion matrix (Fig. 5A) shows that the Random Forest classifier successfully predicted 451 true fluvial segments and 361 true tidal segments, while misclassifying 27 true tidal segments and 20 true fluvial segments with overall segment scale accuracy of 95%. The Receiver Operating Characteristic (ROC) curve (Figure 5B) is a plot of the true positive rate against the false positive rate and shows an area under the curve (AUC) of 0.9865. This near-perfect score indicates an exceptional level of discrimination between classes. The feature importances chart (Figure 5C) shows the top 10 statistical variables, ranked by importance, used to discriminate between classes (Full rankings in Supplementary File S6). Table 3 shows these same rankings with the full names of the top 10 statistical variables included. Statistical variables describing the central tendency and the minimum and maximum of the convolution of normalized radius of curvature with normalized width (NRxNW) comprise the top 5 most important features, with importances at least twice that of the next highest ranked variables. The lowest ranked variable (Rank 88) is the variance of the derivative of normalized radius of curvature with respect to s. The Precision-Recall curve (Figure 5D) is a plot of precision (the proportion of true tidal segments among all segments) versus recall (the proportion of true tidal segments among

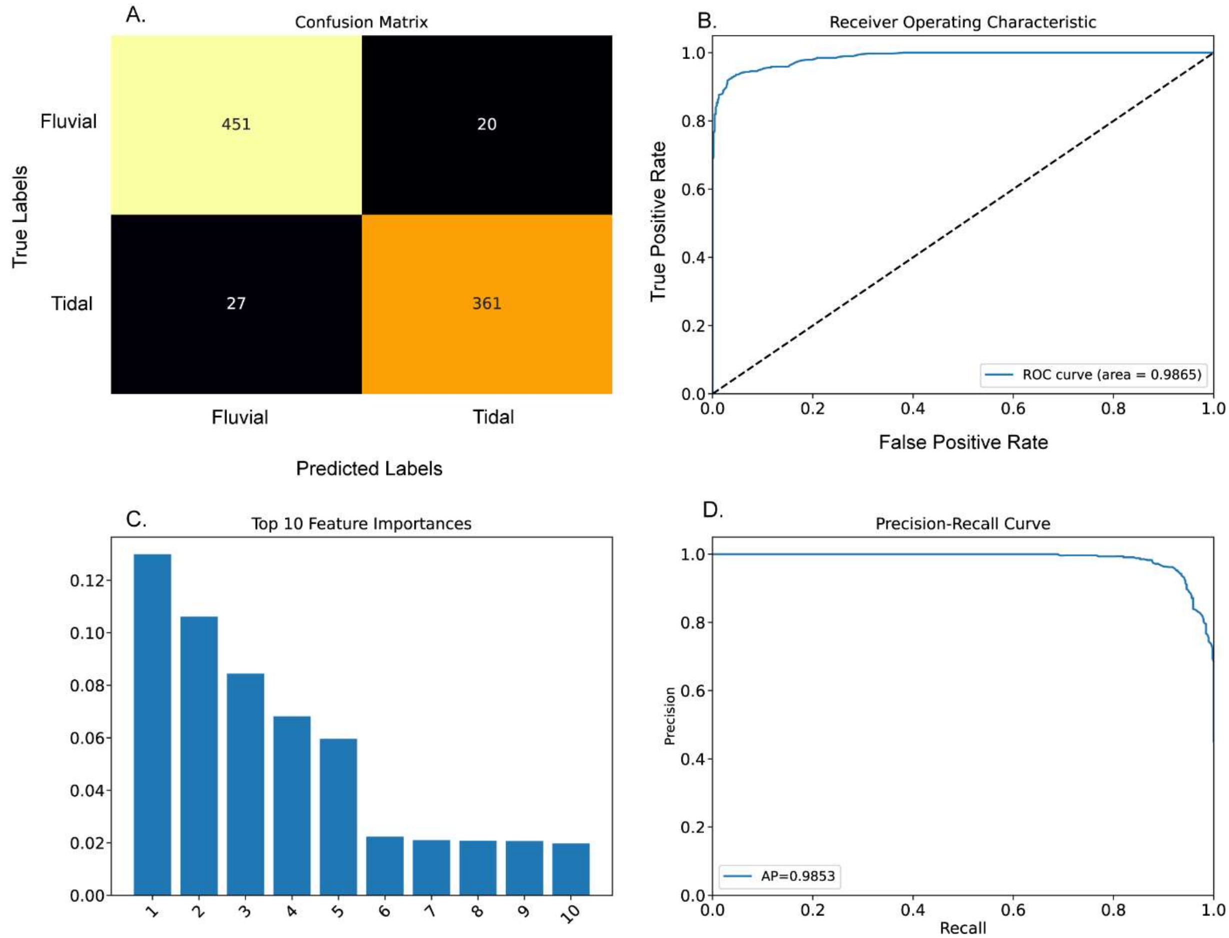

Figure 5. Composite Evaluation of Random Forest Classifier. A) The confusion matrix demonstrates dominantly true positives (tidal) and negatives (fluvial) with fewer false positives and false negatives. B) The ROC curve suggests a high true positive rate with few false positives. C) The feature importance bar chart ranks the top 10 predictors (full feature names are in Table 3), with height representing relative importance. Note that the top 5 are significantly more important than 6-10. D) Precision recall curve indicating high precision at various recall thresholds. Precision drops sharply as recall approaches 1, as the model becomes less conservative at these thresholds.

all actual tidal segments) at different threshold settings. We have an average precision value (AP) of 0.9853, which indicates that the classifier has high precision across a wide range of recall values. Only when the model approaches recall values near 1.0 do we observe a significant drop-off in the precision values, which is expected because the classifier becomes less conservative as it boosts recall, increasing the number of false positives.

Collectively, these results demonstrate that the Random Forest classifier performs exceptionally well at the segment scale, maintaining high accuracies relative to the MLP and Logistic Regression classifier, as well as a high ROC area and Average Precision.

Table 3. Top 10 Ranked feature importances from Trial 58

Rank	Variable Name	Importance
1	NRxNW Minimum	**0.1299**
2	NRxNW Median	**0.1062**
3	NRxNW Midpoint	**0.0845**
4	NRxNW Mean	**0.0682**
5	NRxNW Maximum	**0.0596**
6	NW Midpoint	**0.0224**
7	NW Mean	**0.0210**
8	NW Minimum	**0.0208**
9	NRxNW Range	**0.0207**
10	NW' Range	**0.0197**

Reach-scale Classifier Performance

The performance of individual classifiers at the reach scale using segment-scale data is a key factor in determining the most effective classifier and classification threshold for unknown channel reaches. Figure 6 shows example centerlines for one fluvial channel and one tidal channel, with segments color-coded according to their predicted type from the Random Forest classifier. We presented trained classifier models with previously unseen datasets for 10 tidal and 10 fluvial channels. In 69 trials comparing data scalers and metric configurations, we evaluated the performance of trained models at the reach scale by the percent of channel reaches correctly classified at three classification thresholds using the segment-scale output of the classifiers for a given reach

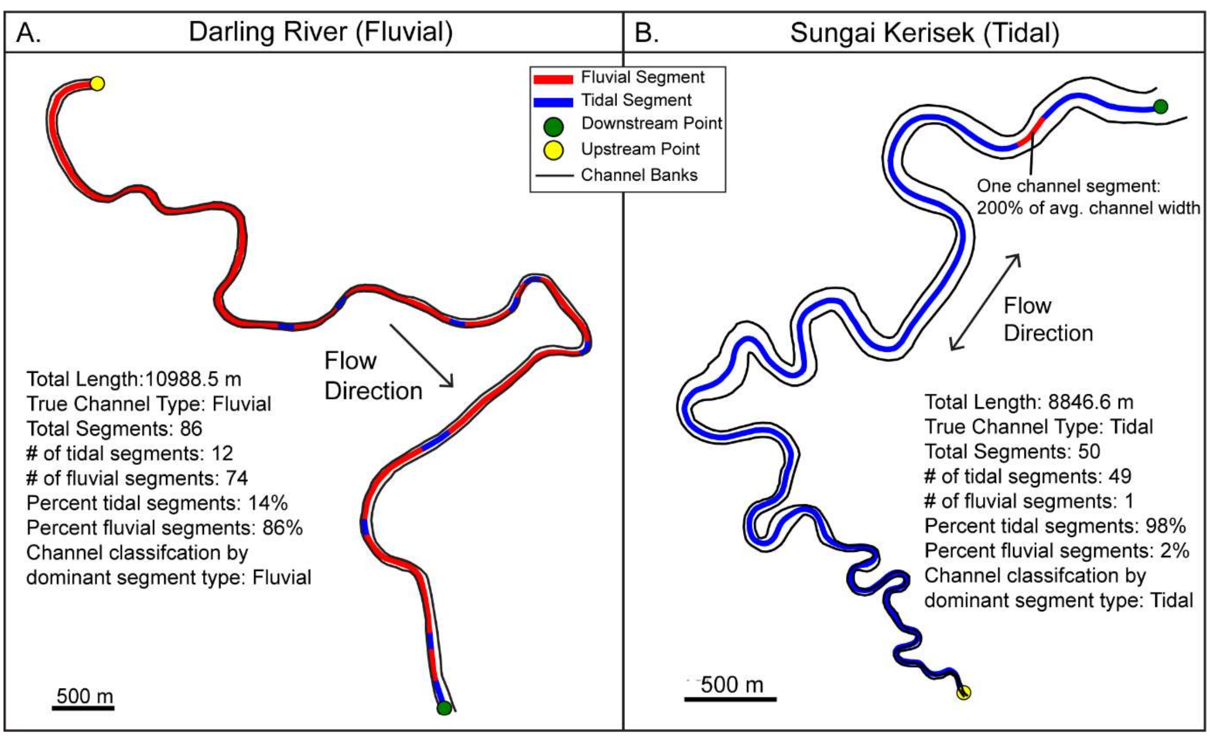

Figure 6. Classified centerlines for two example channels classified using the Random forest classifier and configurations from trial 58: A) Darling river (fluvial), and B. Sungai Kerisek (tidal). Additional information about the length of the reach, number of segments, classification of segments, and classification of the entire channel reach.

Figure 7 is a heatmap showing the accuracy of each classifier at the reach scale for three thresholds, along with the metric configuration and scaler associated with each trial. At the highest classification threshold (>75%), the Logistic Regression classifier had reach-scale accuracies ranging from 25% to 80%, the MLP classifier had reach-scale accuracies of 45% to 80%, and the Random Forest classifier had accuracies between 65% and 80%. At the >66% classification threshold, we observe the following ranges of reach-scale accuracies for each classifier: Logistic Regression = 50% to 85%; MLP classifier = 60% to 90%; and Random Forest classifier = 75% to 95%. The Random Forest classifier had the best performance, followed closely by the MLP classifier, and the Logistic Regression classifier had the worst performance. The >50% classification threshold produced the best reach-scale performance, with the following accuracies for each classifier: Logistic Regression = 70% to 95%; MLP classifier = 75% to 100%; and Random Forest classifier = 85% to 100%. At this classification threshold, all classifiers achieved 95% or greater reach-scale accuracy on one or more trials. Major differences in performance for this threshold can be seen in the minimum accuracies for each classifier, where the Random Forest classifier had the greatest minimum accuracy, the MLP had the second greatest minimum accuracy, and the Logistic Regression had the lowest minimum accuracy.

The heatmap in Figure 7 highlights the broad pattern of results observed throughout the trials. Reach-scale accuracy generally decreased with higher classification thresholds, except in some instances where there was no decrease at higher classification thresholds. For any given trial, no classifier had an increase in reach-scale accuracy as the classification threshold was increased. All classifiers had either decreased or unchanged accuracy with increasing classification thresholds. In most trials, the Logistic Regression classifier performed the worst in comparison to the other two. The Logistic Regression classifier had its best performance in trials 46 and 49 where it achieved 95%, 85%, and 75% reach-scale accuracy for each classification threshold, respectively. The Multi-layer Perceptron classifier reached its peak performance in trial 4, where it had 100%, 90%, and 65% reach-scale accuracies at the respective classification thresholds. The Random Forest classifier outperformed the other two classifiers in trials 58 and 69, where it achieved 100%, 95%, and 75% reach-scale accuracies at the three classification thresholds. Both trials exclude statistical variables from NC, NCxNW, NC', and NCxNW', but trial 58 includes NC/NW whereas trial 68 excludes those variables. Another key difference is that trial 58 uses the standard scaler from sci-kit learn, and trial 69 uses the quantile transformer from sci-kit learn. The metric configuration and classifier used in trial 58 has advantages over that of trial 69, despite identical performance. The quantile

Trial #	MLP > 50%	MLP > 66%	MLP > 75%	RF > 50%	RF > 66%	RF > 75%	LR > 50%	LR > 66%	LR > 75%	Scaler	MC
1	100	85	70	95	85	75	85	85	75	SS	1
2	95	80	70	95	85	70	75	60	50	RS	
3	100	85	70	95	85	70	80	75	70	QT	
4	100	90	65	95	85	75	85	85	75	SS	2
5	95	85	75	95	85	80	75	60	50	RS	
6	95	75	70	95	85	75	85	75	70	QT	
7	95	85	65	95	90	70	85	80	80	SS	3
8	95	85	70	95	90	75	85	60	55	RS	
9	90	80	70	95	90	75	80	75	70	QT	
10	100	85	75	95	90	75	85	80	75	SS	4
11	90	80	80	95	85	75	85	60	55	RS	
12	100	75	70	95	90	70	85	75	70	QT	
13	85	80	60	85	75	70	75	75	65	SS	5
14	85	60	60	85	75	70	70	55	25	RS	
15	80	75	60	85	75	75	80	65	60	QT	
16	95	65	60	85	75	70	75	75	65	SS	6
17	85	60	60	85	80	70	70	50	40	RS	
18	75	75	65	85	80	70	80	70	60	QT	
19	95	70	55	85	80	70	75	75	65	SS	7
20	90	75	60	85	80	70	70	60	40	RS	
21	90	70	60	85	80	70	80	70	60	QT	
22	90	80	50	85	80	80	85	85	70	SS	8
23	90	80	65	85	80	75	70	55	55	RS	
24	95	70	45	85	80	75	70	65	60	QT	
25	90	75	50	85	80	80	85	85	70	SS	9
26	85	80	75	85	80	75	70	55	55	RS	
27	85	75	70	85	80	75	70	65	60	QT	
28	85	75	60	90	80	70	85	80	70	SS	10
29	85	75	65	90	80	70	80	70	60	RS	
30	80	80	75	90	80	70	75	65	60	QT	
31	85	75	70	90	80	65	85	80	70	SS	11
32	85	65	45	90	80	65	80	70	60	RS	
33	90	80	70	90	80	65	75	65	60	QT	
34	90	70	60	100	75	65	80	75	75	SS	12
35	100	70	60	100	75	65	80	50	50	RS	
36	95	80	70	100	75	65	85	75	65	QT	
37	95	75	60	100	80	65	80	75	75	SS	13
38	100	70	55	100	75	70	80	50	50	RS	
39	100	80	70	100	75	70	85	75	65	QT	
40	90	65	60	90	85	70	80	75	75	SS	14
41	90	75	65	95	85	70	85	60	50	RS	
42	95	75	65	90	85	75	85	75	75	QT	
43	90	70	60	90	80	65	80	75	75	SS	15
44	90	75	65	95	85	70	85	60	50	RS	
45	90	90	75	95	85	70	85	75	75	QT	
46	95	80	65	85	80	70	95	85	75	SS	16
47	85	75	65	85	80	70	70	65	55	RS	
48	85	70	70	85	80	70	80	75	65	QT	
49	90	70	60	85	80	75	95	85	75	SS	17
50	85	75	70	85	80	75	70	60	55	RS	
51	85	80	75	85	80	75	85	65	60	QT	
52	90	75	65	85	75	70	95	80	75	SS	18
53	90	75	65	85	75	70	70	70	60	RS	
54	85	75	75	85	75	70	90	65	65	QT	
55	90	85	55	85	85	70	95	80	70	SS	19
56	80	70	65	85	85	70	70	70	60	RS	
57	85	75	70	85	85	75	80	70	65	QT	
58	95	75	70	100	95	75	80	80	80	SS	20
59	100	75	65	100	90	70	80	50	50	RS	
60	95	85	70	100	95	70	85	70	60	QT	
61	100	80	65	100	90	65	80	80	80	SS	21
62	100	85	70	100	90	65	80	50	50	RS	
63	95	90	80	100	90	65	85	70	60	QT	
64	100	75	70	100	90	70	80	80	75	SS	22
65	95	80	65	100	85	75	80	60	60	RS	
66	95	90	75	100	85	75	85	75	65	QT	
67	95	75	70	100	90	75	80	80	75	SS	23
68	95	85	75	100	90	75	80	60	60	RS	
69	95	90	85	100	95	75	85	75	65	QT	

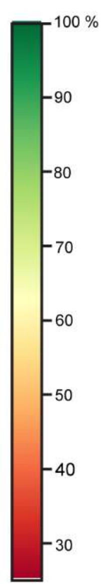

Figure 7. Heatmap showing the reach scale accuracy for Logistic Regression (LR), Multi-layer Perceptron (MLP), and Random Forest (RF) classifiers at three classification thresholds (>50%, >66%, >75%). Each row represents a different trial consisting of different combinations of feature variables and scalers. MC = Metric Configuration; SS = Standard Scaler; RS = Robust Scaler; QT = Quantile Transformer

transformer is a non-linear transformation of input data that suppresses outliers, but it makes interpretation of feature importance difficult as the features are non-linearly related to their original values. Trial 58 uses the standard scaler, a linear transformation, enabling straightforward interpretation of feature importance rankings via preservation of linear relationships variables. As there is no sacrifice in reach-scale accuracy by retaining data interpretability, the Random Forest classifier in trial 58 represents the most successful configuration.

Reach Classification using Random Forest Classifier

Figure 8 shows centerlines for a subset of fluvial and tidal channels used in the reach-scale testing dataset. These reaches were classified with the trained Random Forest classifier using the configurations from the best performing trial (Trial 58) at the >50% threshold. Individual segments of the centerlines are color-coded to show the predicted channel types in the context of their surrounding reach. All 20 fluvial and tidal channel reaches were correctly classified using the >50% threshold.

The performance of all three classifiers for the same channels in trial 58 is shown in Figure 9. Each reach has three bars representing the percent of segments for which the prediction matches the true channel type, with the >50%, >66%, and >75% classification thresholds indicated. This allows direct comparison within and between classifiers and channel types. Each classifier utilizes the data differently, and therefore certain segments classified as one channel type or the other may be classified differently by another model. Normalized width and normalized curvature are the two metrics from which channel planform can be completely reconstructed (Vermeulen *et al.,* 2016). In Figure 10, these two metrics are plotted as a function of distance upstream, for one tidal channel and one fluvial channel, classified by the three classifiers. The classified segments are color-coded to show their predicted channel type. In all cases we see that no two classifiers classify the same reach identically, and that the Random Forest classifier produces the greatest number of segments that are correctly classified.

Discussion

The preceding results show that modern tidal and fluvial channels can be distinguished from each other through statistical analysis of channel planform geometries using common machine-learning tools. The Random Forest classifier exhibited the highest accuracy levels for all three classifiers at the >50% classification threshold by application of outlier-resistant scaling methods. Below we explore four related topics: (1) application of segment-trained classifiers to larger channel

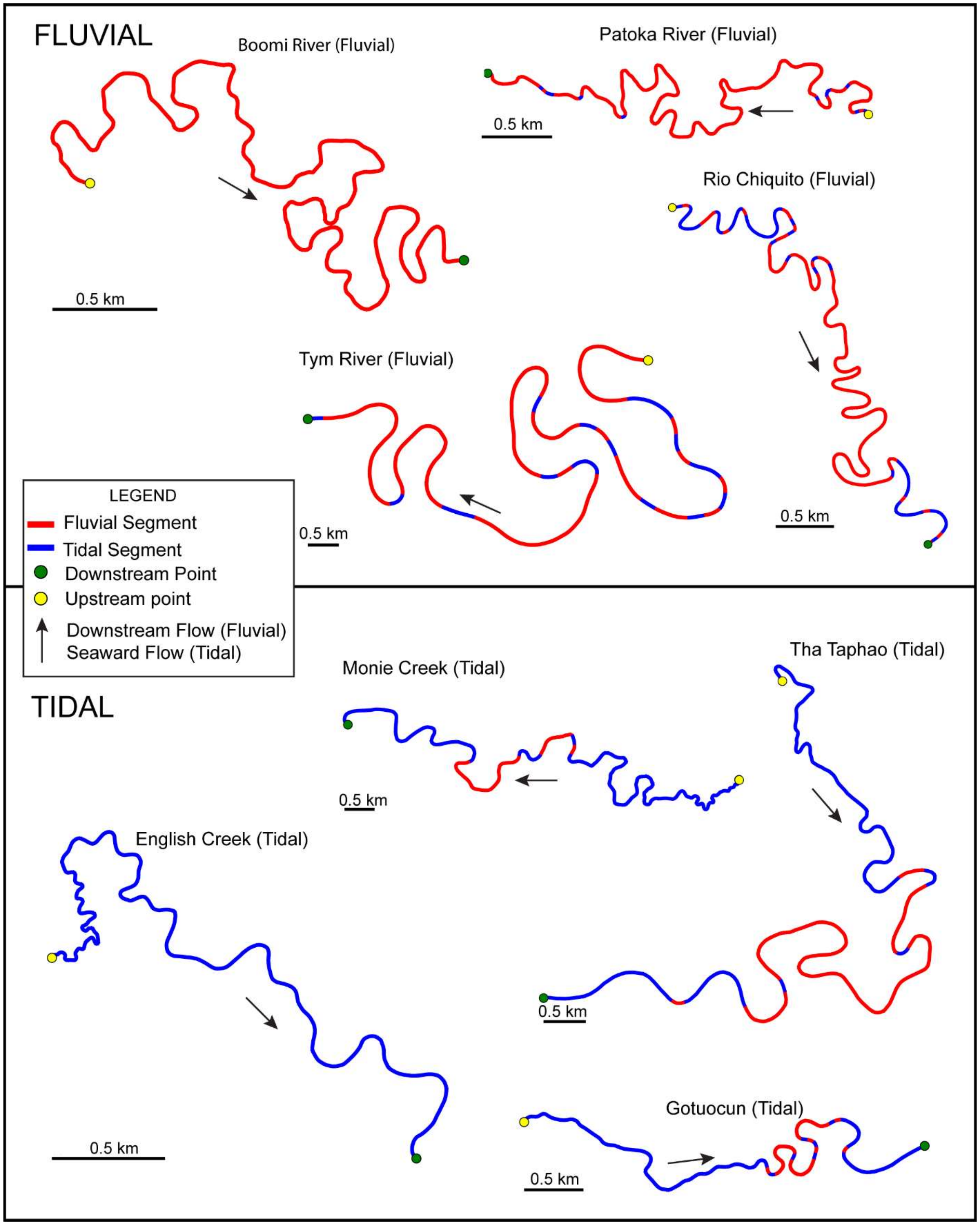

Figure 8. Classified channel centerlines for a subset of classified tidal and fluvial channels used for reach-scale testing. Classified using the trained Random Forest classifier using configurations from the best performing trial (Trial 58).

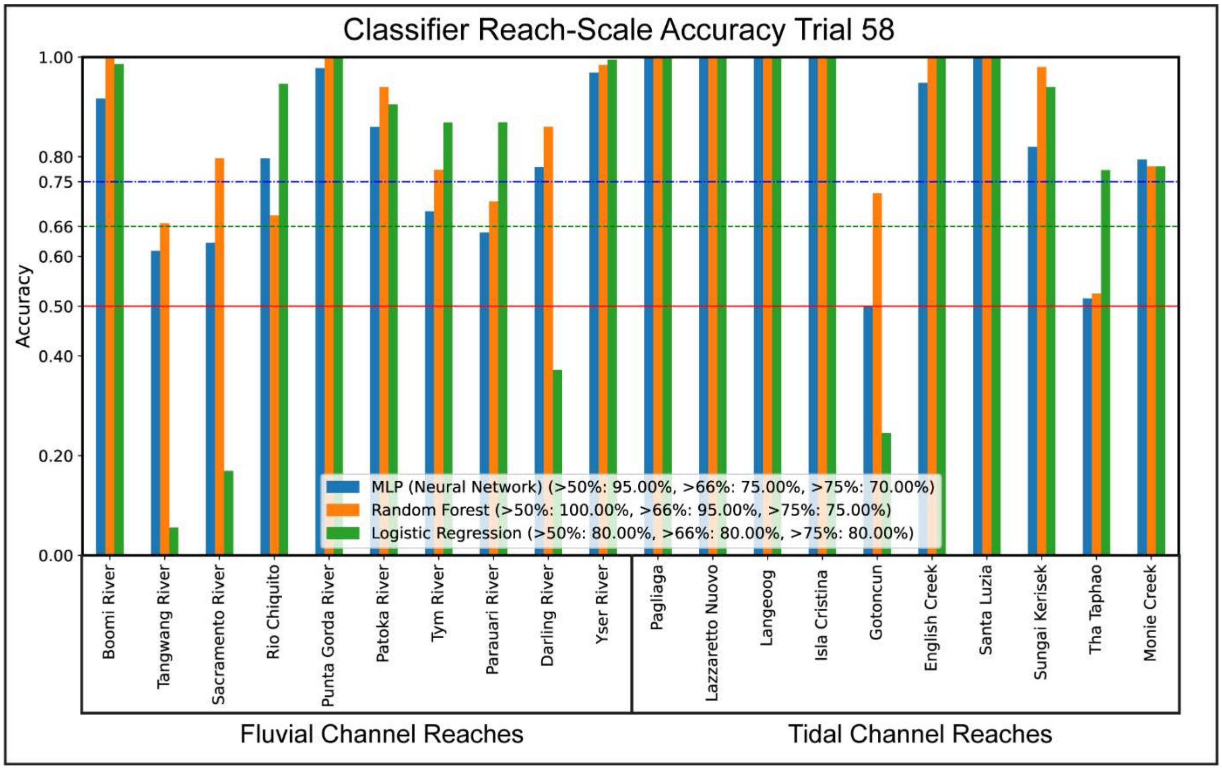

Figure 9: Bar graph comparing the reach-scale accuracy for three different classifiers: Multi-layer Perceptron (MLP), Random Forest, and Logistic Regression. 10 tidal channel reaches and 10 fluvial channel reaches were treated as unknowns by each classifier. The accuracy for each classifier for a given channel is the percentage of 100 m channel segments that were correctly classified (i.e. when the predicted channel type matches the true channel type). Three threshold levels (50%, 66%, 75%) represent the percentage of segments that must be correctly classified in order for the entire reach to be classified as that channel type. The Random Forest classifier has 100 % accuracy at correctly classifying at the reach scale for a 50% threshold, while the MLP (Neral Network) and Logistic Regression classifiers have 95% and 80% accuracy at the 50% threshold, respectively.

reaches; (2) assessment of metric configurations; (3) feature importances and implications for differentiating channel types; and (4) implications for interpreting relict and possibly mixed-energy channel planforms.

Application of segment-trained classifiers to larger channel reaches

By segmenting the data and using statistical variables to describe the geometry of each segment, we can capture local variability and preserve the geometric characteristics of upstream and downstream segments without needing to account for position within the channel or relative to adjacent segments. However, the end goal of the classification is not at the segment scale, but to perform classification of longer channel reaches. To bridge this gap, we calculate the percent of segments in a reach that are classified as tidal or fluvial to obtain a reach-scale classification, without

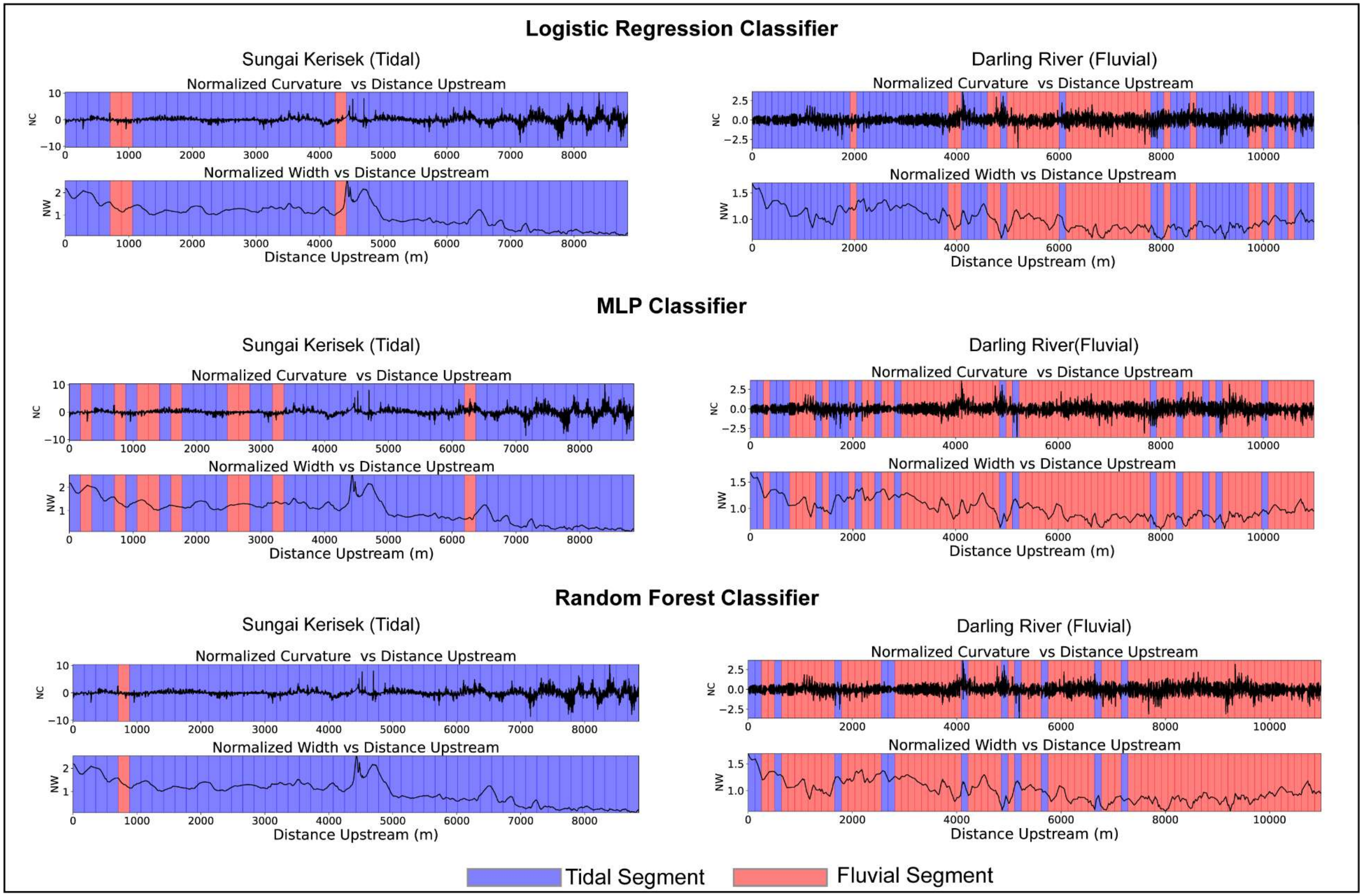

Figure 10. Segment-wise comparison of three classifiers for Sungai Kerisek (tidal) and Darling River (fluvial). Blue segments are tidal and red segments are fluvial. Normalized width (NW) and normalized curvature (NC) signals have been added to each.

having the classifiers classify directly at the reach scale. This approach requires the classification models to have accuracies at the segment scale that are well above 50%. In instances where a model is correct in more than 50% of segments, simple majority reach-scale classification thresholds can be applied. In this study the Random Forest (89-97%),MLP (82-95%), and Logistic Regression (64-90%) classifiers had segment-scale accuracies well over 50%. Interpretation of the spatial distribution of channel segment types for classified reaches should be handled with caution, especially when downstream hierarchies (i.e. fluvial segments cannot be downstream of tidal segments) exist. Channel segments with geometries similar to both tidal and fluvial channels may be misclassified, and the re-classification of downstream segments on this basis may be incorrect. In future work, use of convolutional neural networks and continuous wavelet transform representations of channel reaches may permit direct classification at the reach scale without the need for segmentation or even statistical representations of the channel geometry, while simultaneously preserving sub- to supra-meander scale structures.

Assessment of metric configurations

The best performing Random Forest classifier (trial 58) had a segment-scale accuracy of 95% and a reach-scale accuracy of 95% at the >50% threshold. The high segment-scale accuracy translated to high reach-scale accuracy at the >50% and >66% thresholds but did not translate to equally high accuracy at the 75% threshold. This trial excluded 56 statistical variables derived from NC, NCxNW, NC' and, NCxNW', but did include those from NC/NW. Earlier trials (1-12) that include the 56 additional statistical variables had slightly higher segment-scale accuracies (96-97%), but poorer reach-scale accuracies. Trial 69, which had reach-scale accuracies identical to those of trial 58, did not include NC/NW but had lower segment scale accuracy (94%). This suggests that exclusion of normalized curvature-based variables positively influences the performance of classifiers evaluated at the reach scale, while having a minor negative influence on segment-scale accuracy.

Trial 58 included only principal channel metrics and statistical variables derived from normalized width (NW), normalized radius of curvature (NR), their convolutions (NRxNW), and their derivatives (NC/NW), and it excluded normalized curvature-based variables (NC), their convolutions (NCxNW), and derivatives. Because along-channel width and curvature can be used to reconstruct the planform geometry of a given channel reach (Vermeulen *et al.*, 2016), it is not surprising that width and curvature emerge as two of the principal channel metrics. The Radius of curvature is the inverse of the absolute value of curvature, and unlike curvature, it has no directionality and is merely a representation of how curved a channel is at that point. The exclusion of normalized curvature-based variables from the most successful trial suggests that curvature may not be the best representation of local channel sharpness for the purposes of differentiation between channel types. This may be because the central tendency of normalized curvature values is near-zero for both channel types, a byproduct of its directionality that may inhibit differentiation. Similarly, curvature signals almost always oscillate between negative and positive values as channels change the direction of their bends. For example, segments that are right bending or left bending may have identical magnitude of curvature but with opposite signs due to the direction of the bend. This oscillation due to bend direction makes it difficult to identify relationships between channel sharpness and metrics that do not oscillate. However, this is not to say that curvature does not effectively record channel sharpness, which it certainly does, but instead that other representations of local channel sharpness such as radius of curvature may be better suited for differentiating between channel types and identifying relationships with other variables.

Feature importances and implications for differentiating channel types

Table 3 provides insight into the most important variables for classification according to the Random Forest classifier. The top 5 most important features are measures of the central tendency, minimum, and maximum of the normalized radius of curvature convolved with normalized width (NRxNW). The next 5 most important features are the midpoint, mean, and minimum of normalized width (NW) and ranges of the derivative of normalized width with respect to s (distance along centerline; NW') and NRxNW. NRxNW is a representation of how normalized radius of curvature is modified by normalized width at any point along the channel. It can effectively highlight where the two variables are positively correlated. For example, points along a channel where the normalized width is high and normalized radius of curvature is high (i.e. low channel sharpness) would have a high convolution value indicating there is a strong positive relationship between the two variables. The highest-ranking variable derived from normalized radius of curvature (NR) is the median NR, ranked 36th out of 88 with an overall importance of 0.0071. While normalized radius of curvature does contribute to the differentiation between channel types, its low importance relative to NW or NRxNW derived variables suggests it does not play a critical role in differentiating between channels. These rankings do indicate that the relationship between normalized radius of curvature (channel bend sharpness) and normalized channel width is more important for classification than normalized radius of curvature. In other words, the effect that local channel width at any point along the channel has on the sharpness of bends in the channel is more diagnostic than the actual sharpness of the bend at that point. Curvature is an important factor for the development and migration of channel bends, as bank erosion (e.g., active migration) has been shown to occur where curvature is the sharpest (Sylvester et al., 2019).

Figure 11 shows the kernel density and cumulative density plots of normalized radius of curvature convolved with normalized width and normalized width, and plots of NRxNW and NW versus normalized distance upstream for tidal and fluvial channels. Kernel density plots of NRxNW show that tidal channels tend to have lower values of NRxNW (Fig. 11A), suggesting that tidal channels have configurations in which narrow channel widths co-occur with tighter bends (i.e. smaller radius of curvature). The distribution of NRxNW for fluvial channels is much broader than that of tidal channels, indicating a more complex or less direct relationship between local channel width and channel sharpness. This finding is consistent with results of Finotello *et al.* (2020), who found that fluvial channels have greater morphological complexity than tidal channels, and attributed the difference to fundamental differences in flow conditions between the two domains (Leopold et al., 1964). They segmented channel reaches into individual meanders, which allowed meander-specific metrics not included in our study to provide insight into morphological differences (Finotello *et al.,* 2020). The difference between morphological complexities of tidal and fluvial channels is resolvable both in meanders and smaller segments. Kernel density plots of NW (Fig. 11B) show that fluvial channels have a much higher density around normalized widths of 1, indicating that channel width for a fluvial reach does not vary significantly relative to its average, and rarely exceeds 2 times the average width. Tidal channels have normalized widths close to 1 in most instances, but the distribution is highly positively skewed relative to fluvial channels with normalized widths exceeding 6 times the average channel width. These pronounced differences result from normalization of local channel width by the average width of the channel at the reach scale and reflect the characteristic downstream increase in channel width observed in many tidal channels (Marani *et al.*, 2002; Fagherazzi *et al.*, 2004; Lanzoni & D'Alpaos, 2015). Cumulative density plots and non-parametric Kolmogorov-Smirnov (K-S) tests of NRxNW and NW (Figs. 11C, D) quantify the differences in the distributions between channel types. Figure 11C shows a K-S statistic of 0.6330 with a p value of <0.001, indicating that fluvial and tidal distributions of NRxNW are statistically different at a significant level, and likely reflect different processes driving the relationship between normalized radius of curvature and normalized width. Figure 11D shows the CDF of normalized

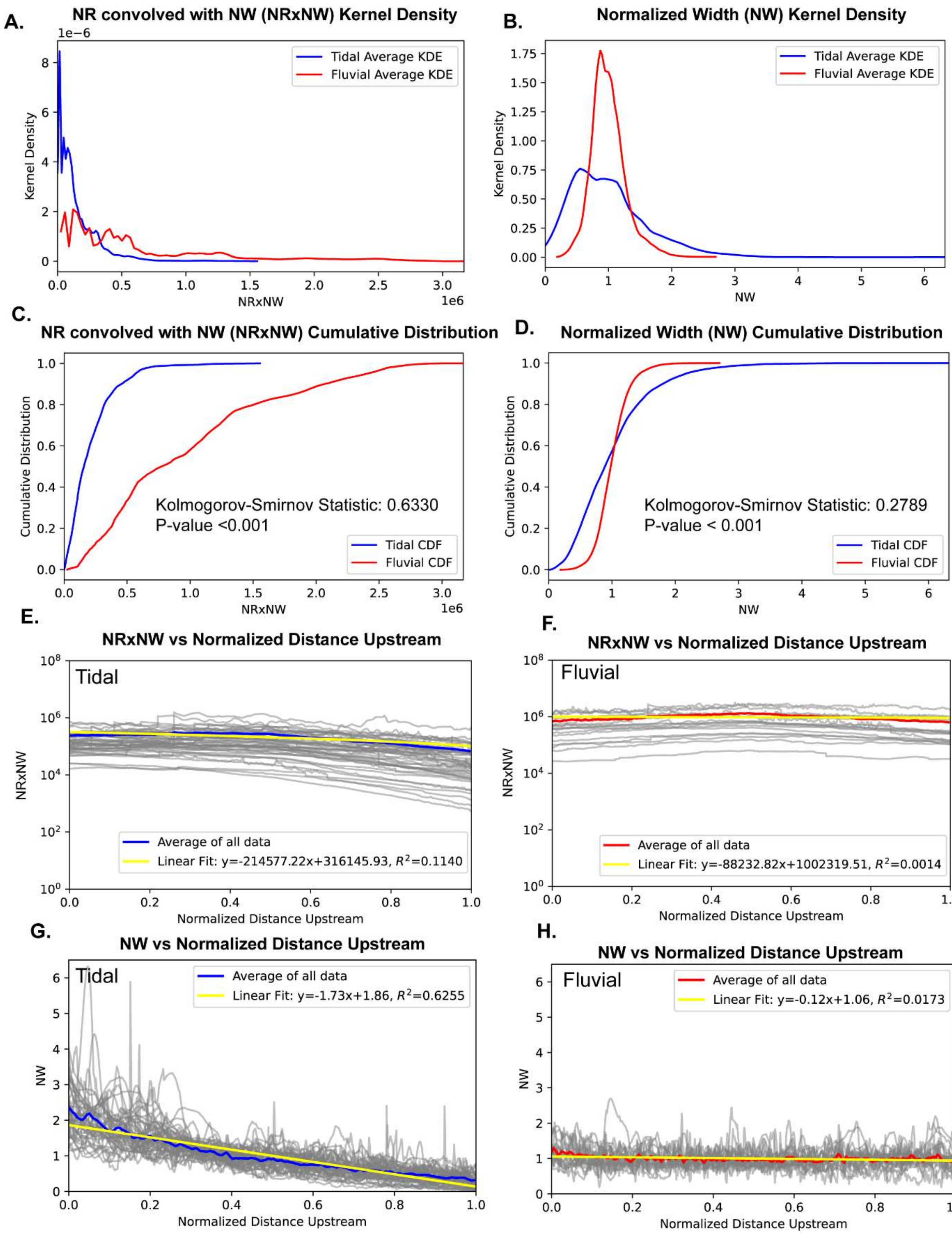

Figure 11. Statistical and along-channel plots of important principal along channel metrics, A,B) Kernel density plots showing distrubitons of NRxNW and NW for tidal and fluvial channels; C,D) Cumulative distributions NRxNW and NW for tidal and fluvial channels, Kolmogorov-Smirnov statistics indicate percent difference between functions in decimal form. Higher values indicate more separation. E,F) Plots of NRxNW vs normalized distance upstream for tidal and fluvial channels; G,H) Plots of NW vs normalized distance upstream for tidal and fluvial channels.

width and has a K-S statistic of 0.2789 at a p-value of <0.001. This indicates that the distributions of normalized width for tidal and fluvial channels are significantly different, although to a lesser magnitude than NRxNW. The distributions and significant differences in NRxNW and NW between channel types are consistent with high feature importance rankings of variables derived from these metrics.

Along-channel patterns in NRxNW for tidal channels (Fig. 11E) shows a gradual decrease in NRxNW in the upstream direction, suggesting that high radii of curvature are associated with higher widths at the mouths, and lower radii of curvature are associated with narrower widths in the upstream portions of reaches. This contrasts with the along-channel pattern of NRxNW for fluvial channels, which display relatively little change in the NRxNW in the upstream direction (Fig. 11F). In addition, tidal channels display a quasi-exponential decrease in channel width in the upstream direction (Fig. 11G), a pattern recognized in other prior studies (Marani *et al.*, 2002; Fagherazzi *et al.*, 2004; Lanzoni & D'Alpaos, 2015). In contrast, the along-channel distribution of normalized width for fluvial channels shows relatively consistent channel widths (Fig. 11H), with values fluctuating irregularly around 1. This pattern likely results in more complex or less direct relationships between normalized width and normalized radius of curvature. While upstream narrowing of tidal channels has been recognized in prior studies (Marani *et al.*, 2002; Fagherazzi *et al.*, 2004; Lanzoni & D'Alpaos, 2015), this study is the first to incorporate this pattern into machine-learning and statistical analysis via reach-scale normalization of segments. Additionally, this study is the first study to quantify the morphological relationship between normalized width and normalized radius of curvature via convolution of the two along-channel signals, which we use to classify channels using machine-learning algorithms.

Implications for interpreting relict channels and mixed-energy settings

While recognition of channel type is typically straightforward in modern settings, methods developed here offer promising potential to study ancient, relict channels preserved on inactive low-relief surfaces. Because tidal channels generally form within 1-5 meters of mean sea level, recognition of tidal channels on relict surfaces can provide useful constraints on changes in relative sea level and vertical crustal motions. Conversely, fluvial channels provide no information about relative sea-level change or uplift rates. Low-relief geomorphic surfaces with preserved channel planforms are known from uplifting coastal landscapes in active tectonics settings around the world, including: (1) rift-flank uplifts adjacent to extensional and transtensional plate boundaries (e.g., Red

Sea and Gulf of Suez (Morag *et al.*, 2019); Baja California, Mexico (Ortlieb, 1991); (2) young uplifts in zones of active continental collision (e.g., Persian Gulf of southwest Iran (Berberian, 1995); Ganges-Brahmaputra Delta in southern Bangladesh (Kuehl *et al.*, 2011)); and (3) forearc regions undergoing uplift above active subduction zones (e.g., southwest Japan, North Island of New Zealand, Cascadia of western North America, and Chilean margin of South America (Menant *et al.*, 2020). These regions offer the potential for study of preserved inactive low-relief landscapes to identify and use relict tidal channels to gain improved understanding of uplift histories.

The channel reaches used in this study were either completely fluvial or completely tidal. This choice was made intentionally, to have as little overlap in channel origin as possible for the purposes of machine learning. However, mixed tidal and fluvial energy settings are commonly observed in estuaries. While the methodology developed in this paper can be applied to future studies of channels in mixed tidal-fluvial settings, important factors should be considered. For example, misclassification of channel segments is likely to occur at higher rates in mixed-energy settings, because the juxtaposition of contrasting processes may produce intermediate morphologies unfamiliar to the trained classifier. Segmentation in this methodology was implemented to preserve local channel geometries while also allowing for segments to be analyzed in the context of the channel type, and thus misclassifications can place tidal segments in purely fluvial channels and vice versa. This challenge can potentially be addressed through use of geographical markers to identify tidally-dominant versus fluvially-dominant sections in estuary systems. For example, a decrease in abundance of tidally-classified segments upstream of the furthest inland extent of modern tides would suggest that our methodology can be applied to a mixed-energy setting. It may also be possible to implement a third classification category that represents mixed energy or undifferentiable segments.

Conclusions

We present a machine learning-based classification method that uses reach-normalized data to classify channels as either tidal or fluvial. Through training multiple classifiers on a global dataset of tidal and fluvial channels we find: (1) Linear Discriminant Analysis is not sufficient for classification; (2) the Random Forest classifier demonstrated 100 % accuracy at classifying "unknown" channel reaches at the >50% classification threshold, indicating that this classification method is robust and reliable; and (3) the convolution of normalized radius of curvature with normalized width (NRxNW) and normalized width (NW) are more successful for differentiating tidal channels using this approach than the magnitude of local curvature.

This methodology offers the potential to identify relict tidal channels on inactive low-relief surfaces and constrain uplift histories in a wide range of tectonic and physiographic settings. It may also be possible to analyze channel planforms in mixed-energy settings using this approach, although care must be taken when interpreting the spatial arrangement of classified segments. Future work could use wavelet representations of channel morphologies and train convolutional neural networks to classify channels directly at the reach scale while retaining sub- and supra-meander structures.

Bridge

With an effective method for the classification of modern tidal and fluvial channels, we can now apply this method to relict channels of unknown origin. In Chapter IV we apply the trained random forest classifier and reach-scale classification methodology developed in Chapter III to a dataset of 14 relict channels that include both unknown and likely fluvial relict channels from the central Baja California Peninsula and other localities around the world and classify their geometries as tidal or fluvial to determine their origin. Furthermore we analyze the performance of the random forest classifier and consider the relict channels classified as tidal in the context of global sea level changes over the last 798 ky and discuss their efficacy as paleo-sea level indicators.

CHAPTER IV: IDENTIFICATION OF RELICT CHANNELS USING A TRAINED RANDOM FOREST CLASSIFIER

This chapter includes un-published co-authored material. Principal data collection, analysis, figure creation and manuscript writing was completed by Kevin Gardner. Rebecca J. Dorsey assisted in study site selection and data analysis and provided editorial feedback on the manuscript and figures.

Introduction

Channels are critical features of tidal and fluvial systems that are shaped by fluid flow and sediment transport. The flow conditions of tidal and fluvial systems are considerably different due to contrasting hydrodynamic processes. Tidal systems experience bi-directional currents and cyclical daily to monthly fluctuations in the volume of the tidal prism, whereas fluvial systems experience unidirectional flow with stochastic weather-modulated and seasonal fluctuations in discharge (Leopold *et al.*, 1964; Kvale *et al.*, 1995; Fagherazzi *et al.*, 2004; Lutscher *et al.*, 2007; Hughes, 2012). Despite major differences in the flow conditions of tidal and fluvial channels, their meander evolution and planform geometries are remarkably similar (Leopold *et al.*, 1964; Lanzoni & Seminara, 1998; Marani *et al.*, 2002; Lanzoni & D'Alpaos, 2015; Finotello *et al.*, 2018; Gao *et al.*, 2024).

Bi-directional currents in tidal systems produce meander geometries that are statistically different from fluvial meanders, with meander asymmetry being the most important component in statistical analyses for effectively clustering tidal and fluvial reaches (Fagherazzi *et al.*, 2004; Finotello *et al.*, 2020). A recent study found that a random forest classifier trained on geometric data from modern tidal and fluvial channels can successfully classify entire reaches as tidal or fluvial using segment-scale classifications and majority thresholds to determine reach classification (Gardner & Dorsey, 2025). Feature rankings from the trained random forest classifier show that the top five most important variables for differentiating tidal and fluvial segments are measures of the minimum, central tendency, and maximum of the convolution of local normalized radius of curvature and normalized width. Fluvial channels exhibit a more complex relationship between local channel width and sharpness of channel bend, consistent with observations of greater morphological complexity in fluvial channels compared to tidal channels driven by differences in flow conditions (Finotello *et al.*, 2020; Gardner & Dorsey, 2025). Effective classification of tidal and fluvial channel reaches is possible using the relationship between local normalized radius of curvature and local normalized width and, to a lesser extent, local normalized width where it can capture downstream funneling commonly observed in tidal channels (Lanzoni & Seminara, 1998; Marani *et al.*, 2002; Lanzoni & D'Alpaos, 2015; Gardner & Dorsey, 2025).

The segment-based machine-learning classifier developed by Gardner and Dorsey (2025) can also be used for identification of relict channels on abandoned low-relief surfaces, with potential implications for paleo-sea level reconstructions in coastal regions. Tidal channels form at or near sea level within the local tidal range, whereas fluvial channels can form at any elevation. If relict channels preserve the planform geometric characteristics of their original domain (tidal or fluvial), then classification of relict reaches should be possible. If a relict channel is classified as tidal, the elevation of the surface on which the channel formed provides a record of relative sea-level change (Figure 1). The elevation difference between a relict tidal surface and modern sea level represents a fall of relative sea level that may be due either to crustal uplift or a fall in global sea level after abandonment of the channel. Because present-day sea level is at or near the highest interglacial levels recorded in the past ~ 1 m.y. (e.g., Spratt & Lisiecki (2016), preservation of tidal channel planforms on relict geomorphic surfaces in most cases provides evidence for post-abandonment uplift.

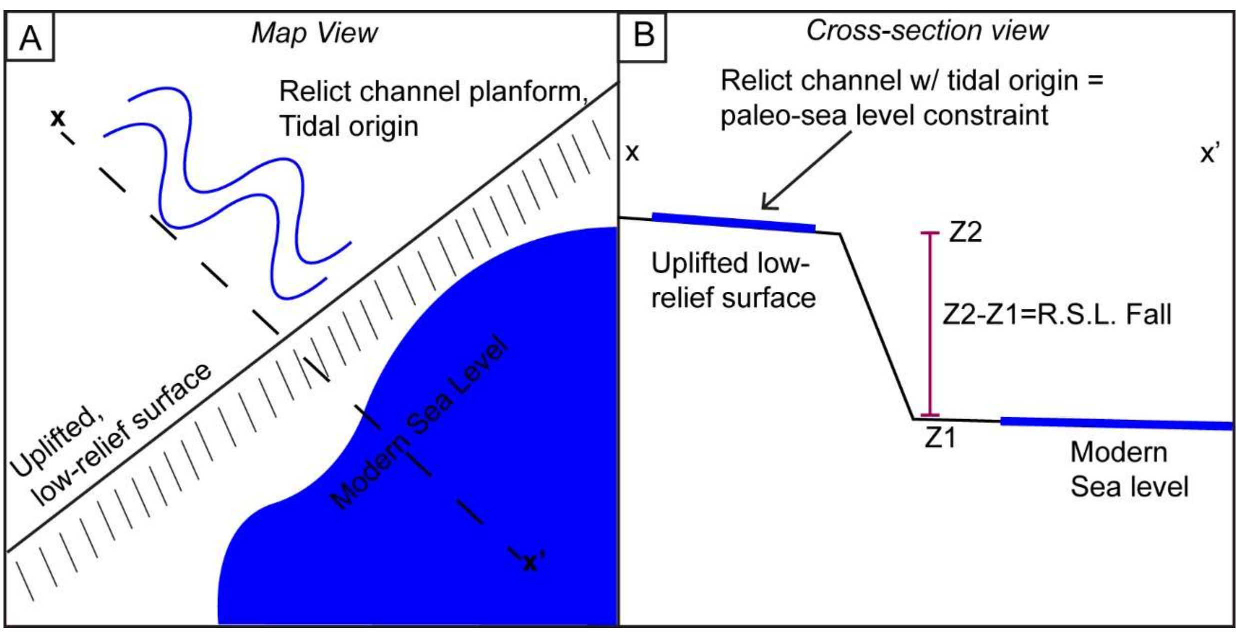

Figure 1. Conceptual diagram of using relict channels with tidal origin as paleo-sea level indicators. A) Map view of relict channel with a tidal origin on an uplifted surface; B) Cross-section view from x-x' showing the elevation difference between relict channel with a tidal origin and modern sea level being used to constrain relative sea level (R.S.L) fall.

Prior analyses of relict channels have focused on terrestrialization of abandoned paleochannels of fluvial systems, reconstruction of long term river evolution, and sediment accretion in abandoned paleochannels in tide-dominated systems (Woodroffe *et al.*, 2016; Dépret *et al.*, 2017; Tena *et al.*, 2020; Vayssière *et al.*, 2020; Wu *et al.*, 2020; Alam *et al.*, 2025; Nathan *et al.*, 2025). Many of these studies, especially those in tide-dominated settings, provide valuable insight into understanding channel reorganization due to rising sea level. Previous studies have had the benefit of evidence connecting them to their domain of formation, but little work has been done on relict channels on uplifted low-relief paleosurfaces where data is limited and the domain of formation is not known. In this study we address this gap in understanding of relict channels by tackling three questions: (1) Do relict channels inherit the geometric characteristics of their domain of formation? (2) Can relict reaches be effectively classified using random forest classifiers trained on modern tidal and fluvial channels? (3) What are the implications for paleo-sea level reconstruction using relict channels of tidal origin? To assess these questions, we applied the random forest classifier and classification methods of Gardner & Dorsey (2025) to classify 14 relict channels at elevations ranging from 7 m to 1335 m above modern sea level (trained model files and classification script in Supplementary Files S1-S2). We use the results to evaluate classification probability scores of relict channels, and compare them to modern channels from a dataset of modern tidal, fluvial, and mixed-energy channels. Our results show that relict channels retain much of the geometric characteristics of their original channel type, allowing them to be classified as tidal or fluvial. Probability score distributions provide an important metric for evaluating the level of confidence in classification of relict channels. We also demonstrate the potential of this method for estimating the magnitude and time-averaged rate of uplift in coastal regions where well-dated relict tidal channels are preserved.

Summary of Relict Channel Study Areas

In this study we digitized 14 middle to late Pleistocene relict channels in several locations around the world for comparison to examples from the testing dataset of Gardner and Dorsey (2025) (Figure 2; Relict channel data table in Supplementary File S3). Relict channel localities span climates from arid to humid and are found at elevations from 7 m to 1335 m above sea level. The studied sites include relict channels that are of unknown or potentially tidal origin, relict channels with known fluvial origins, and channels that are likely to be fluvial due to their distance from modern shorelines.

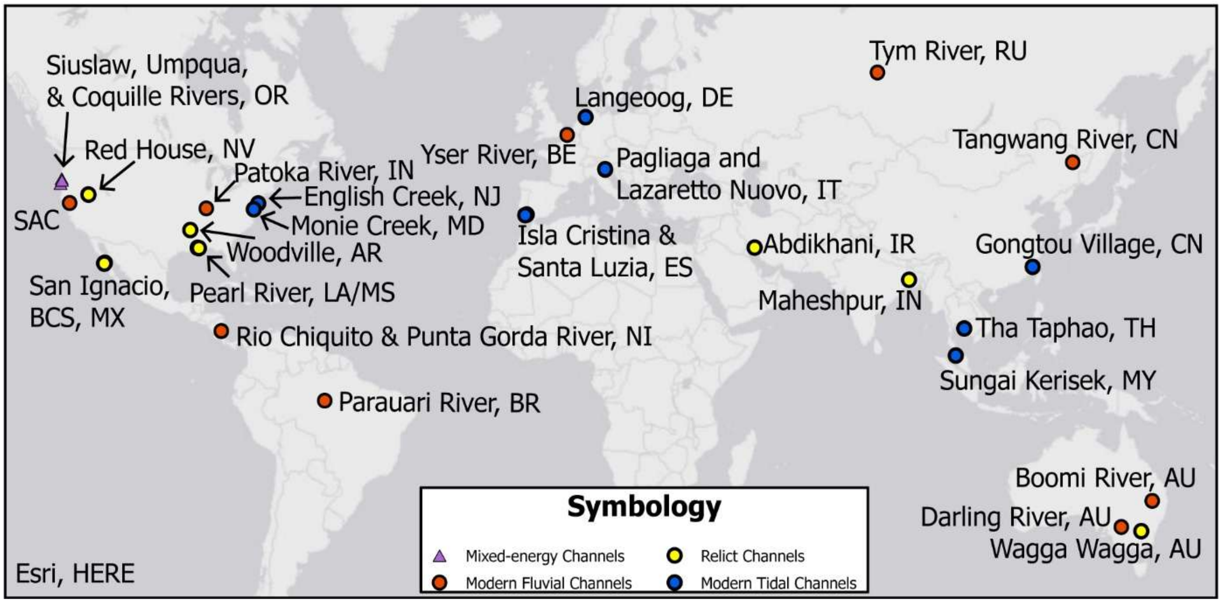

Figure 2. Map showing distribution of relict channels, modern tidal and fluvial channels, and mixed-energy channels used in this study. Yellow circles represent relict channels, red circles represent modern fluvial channels, blue circles represent modern tidal channels, and purple triangles represent modern mixed-energy channels. OR = Oregon; NV = Nevada, SAC = Sacramento River; BCS, MX = Baja California Sur, Mexico; AR = Arkansas; LA = Louisiana; MS = Mississippi; MD = Maryland; NJ = New Jersey; IN = Indiana, USA or India; BE = Belgium; DE = Germany; BR = Brazil; NI = Nicaragua; ES = Spain; IT = Italy; RU = Russia; CN = China; IR = Iran; TH = Thailand; MY = Malaysia; AU = Australia

Central Baja California Peninsula, BCS, Mexico

The central Baja California Peninsula (Figure 3A) has a 20–30 million year history of subduction-related volcanism and transition from subduction of the Farallon plate to transtensional rifting associated with opening of the Gulf of California (Hausback, 1984; Umhoefer *et al.*, 2001, 2018; Carreño & Smith, 2007; Bennett & Oskin, 2014; Bennett *et al.*, 2015; Darin *et al.*, 2016). Marine deposits in the mid-peninsular region include the 15–11 Ma San Ignacio Formation which records tidally influenced deposition on a shallow marine shelf on the western peninsula, as well as the Late Miocene Boleo Fm. and the Pliocene-Quaternary Tirabuzón, Infierno, and Santa Rosalia formations in the Santa Rosalia basin (Bennett et al., 2025; Darin et al., 2025; Dorsey et al., 2024 in press; McLean et al., 1985). Quaternary marine terraces have been documented along the length of the peninsula at elevations ranging from ~10 m to 340 m above sea level(Ortlieb, 1991). In the Laguna San Ignacio region, near Punta Abreojos on the Vizcaino Peninsula, marine terraces have been documented at elevations ranging from 6 m to 90 m above sea level, and were assigned ages ranging from 80 ka to early-middle Pleistocene using U-Th geochronology, Amino Acid Racemization (AAR), faunal assemblages, and oxygen isotopes (Ortlieb, 1991).

Figure 3. Overview maps of Baja Relict channels 1-4. A) Overview of the central Baja California Peninsula, Mexico with a black square at the northern end of Laguna San Ignacio from which the relict channels in B,C,D,E were digitized; B) Baja Relict Channel 1 at 67 m above sea level; C) Baja Relict Channel 2 at 50 m above sea level; D) Baja Relict Channel 3 at 38 m above sea level; E) Baja Relict Channel 4 at 38 m above sea level. Black lines indicate digitized bank lines

In the Laguna San Ignacio region we digitized four relict, abandoned channels at elevations ranging from 38 m to 67 m above sea level (Figure 3B – 3D). The relict channels appear to be associated with paleoshorelines of Laguna San Ignacio, and they are associated with Quaternary marine terraces documented by Ortlieb (1991). Field observations at Baja Relict Channel 2 (Fig. 3C) confirmed the presence of Quaternary marine terrace deposits on the surface where the channel formed. Based on their association with known elevations of Quaternary marine terraces and their association with paleoshorelines, these relict channels are considered to have an unknown or potentially tidal origin.

Abdikhani, Iran

Abdikhani, Iran is a village in the Khuzestan Province of southwest Iran approximately 33 km northeast of the larger population center of Hendijan (Figure 4A). The geological history of the region is dominated by uplift, deformation, and faulting in the Zagros fold and thrust belt, and associated foreland basin sedimentation (Ghorbani, 2013). Abdikhani is situated on the NE flank of a NW-trending anticline associated with a NW-trending thrust fault that represents the southwestern front of the active fold and thrust belt. Limited data on the geology of the Abdikhani region is available, and average uplift rate is estimated at ~1 mm /yr (Berberian, 1995).

We digitized three relict channels 3.5 km northeast of Abdikhani selected from a network of abandoned channels (Figure 4B). The relict channels in this region display downstream widening that is typical of tidal channels, and they have upstream connectivity between drainage areas that is also common to tidal networks. Relief between channel banks and the base of the channel is typically 1-2 meters, and the flat channel bottoms have more recently been adapted for farming. The channels are all between 55 m and 57 m above sea level. Assuming an average uplift rate of ~1 mm/yr (Berberian, 1995), the elevation of these relict channels suggests they may have been at or near modern sea level approximately 55,000–57,000 years ago. Based on the tidal-like geometries of the channels and the plausible time frame for the region being at or near sea level during the Quaternary, we consider these channels to be unknown or potentially of tidal origin.

Pearl River, Louisiana, USA

The Pearl River flows south into the Gulf of Mexico along the border between southeast Louisiana and southwest Mississippi, (Figure 5A). The surficial geology of the lower Pearl River region consists predominantly of Holocene and Pleistocene coastal plain deposits and ancient Pearl River deposits (Heinrich, 2006). Holocene deposits are present on a narrow terrace directly adjacent to the modern Pearl River and represent inactive meander belts and backswamps formed during

Figure 4. Overview maps of Iran Relict Channels 1,2, and 3. A) Overview of SW coastal Iran (IR) with black square indicating the location of the relict channels on the NE limb of an uplifting anticline. Red dashed line shows the major fault associated with the growth of the anticline. B) Satellite imagery of the three relict channels near Abdikhani, Iran. White lines show the digitized banklines, numbers correspond to the relict channel number.

recent configurations of the Pearl River. The Pearl River relict channel belongs to a collection of coastal plain deposits known as the Prairie Allogroup, which form a terrace extending from the coast of the Gulf of Mexico eastward to Mobile, Alabama (Heinrich, 2006). The Prairie Allogroup in the Pearl River region is composed mainly of the Hammond Alloformation, which has an age of 194 ± 14 ka at St. Tammany, LA (Otvos, 2005; Heinrich, 2006). The Stennis relict channel is associated with deposits of the Gum Bayou Alloformation, which forms a terrace inset into the Prairie Allogroup along a relict valley of the Pearl River near the Stennis Space Center (Heinrich, 2006).

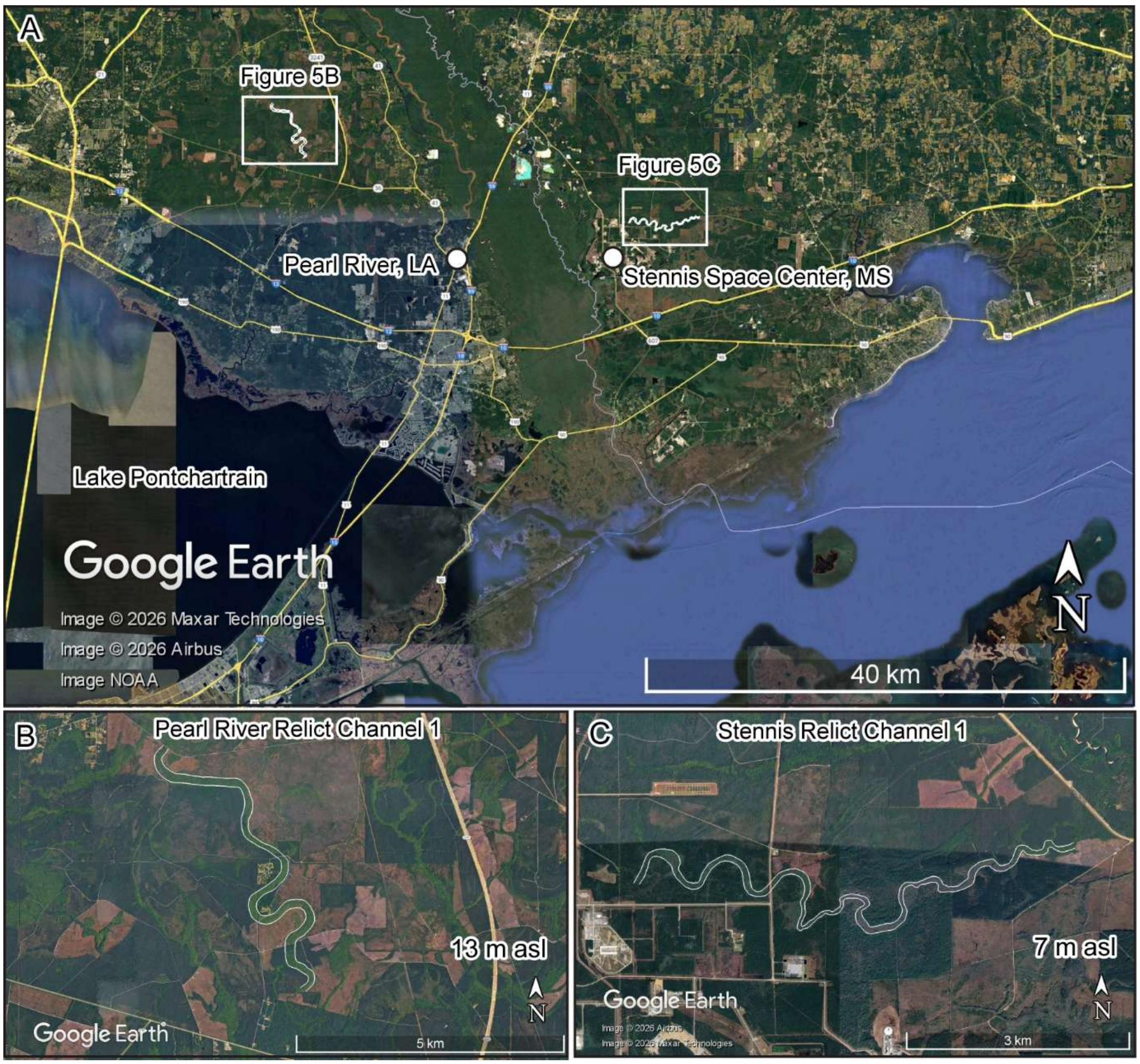

Figure 5. Overview maps of Pearl River and Stennis relict channels. A) Overview map of the Louisiana (LA)/Mississippi (MS) border along the Pearl River near Lake Pontchartrain. White squares indicate the locations of relict channels in B and C. B) Pearl River Relict Channel 1 at 13 m above sea level; C) Stennis Relict Channel 1 at 7 m above sea level. White lines indicate the digitized bank lines.

Relict channel forms are ubiquitous features on the surfaces of the Hammond and Gum Bayou Alloformations (Heinrich, 2006). We digitized two relict channels in this area: the Pearl River Relict Channel 1 (Figure 5B), and the Stennis Relict Channel 1 (Figure 5C). Pearl River Relict Channel 1 is 13 m above sea level on the surface of the Hammond Allofomation, where the surface has an age of 194 ± 14 ka based on OSL dating (Otvos, 2005). The Stennis River Relict Channel 1 occurs 7 m above sea level and occupies the surface of the Gum Bayou Alloformation, which has an OSL age of 124 ± 12 ka (Otvos, 2005). Although the relict channels in this region are generally referred to as fluvial, the ages of the two alloformation terraces overlap with sea level highstands at ~125 and ~200 ka (Spratt & Lisiecki, 2016). Estuarine deposits are known from the Prairie Allogroup (Heinrich, 2006), and no studies have directly analyzed the relict channels in this region for potential tidal influence. For this reason, we consider the Pearl River and Stennis relict channels to be likely fluvial with potential for tidal influence.

Red House, Nevada, USA

Red House, Nevada, is a small community located on the Humboldt River in the Basin and Range Province of north-central Nevada (Figure 6A). The Miocene to recent geologic history of the region is dominated by E-W extension and associated normal faulting. Surrounding mountain ranges are composed of Paleozoic-Cenozoic sedimentary, volcanic, and metamorphic rocks, while valley floors consist predominantly of Quaternary alluvium and gravel associated with alluvial fans and drainages sourced in the surrounding mountains. Local sediments also include former deposits of the Humboldt River and its local tributaries (Hotz & Willden, 1961; Erickson & Marsh, 1974).

There are numerous relict abandoned channels on the terraces adjacent to the Humboldt River and adjacent to modern tributaries. We digitized two relict reaches on terraces on the north (Figure 6B) and south (Figure 6C) banks of the Humboldt River. Other than existing geologic maps that assign a general Quaternary age to the alluvium, there are no available ages for these surfaces or channels. Given their distance 100's of km from nearest ocean coastlines and an average elevation of 1334 m above sea level, we considered these relict reaches to be likely fluvial in origin.

Maheshpur, India

Maheshpur, India is small village located in the state of West Bengal, India, near the border with Bangladesh, approximately 212 km north of the shoreline of the Ganges-Brahmaputra Delta

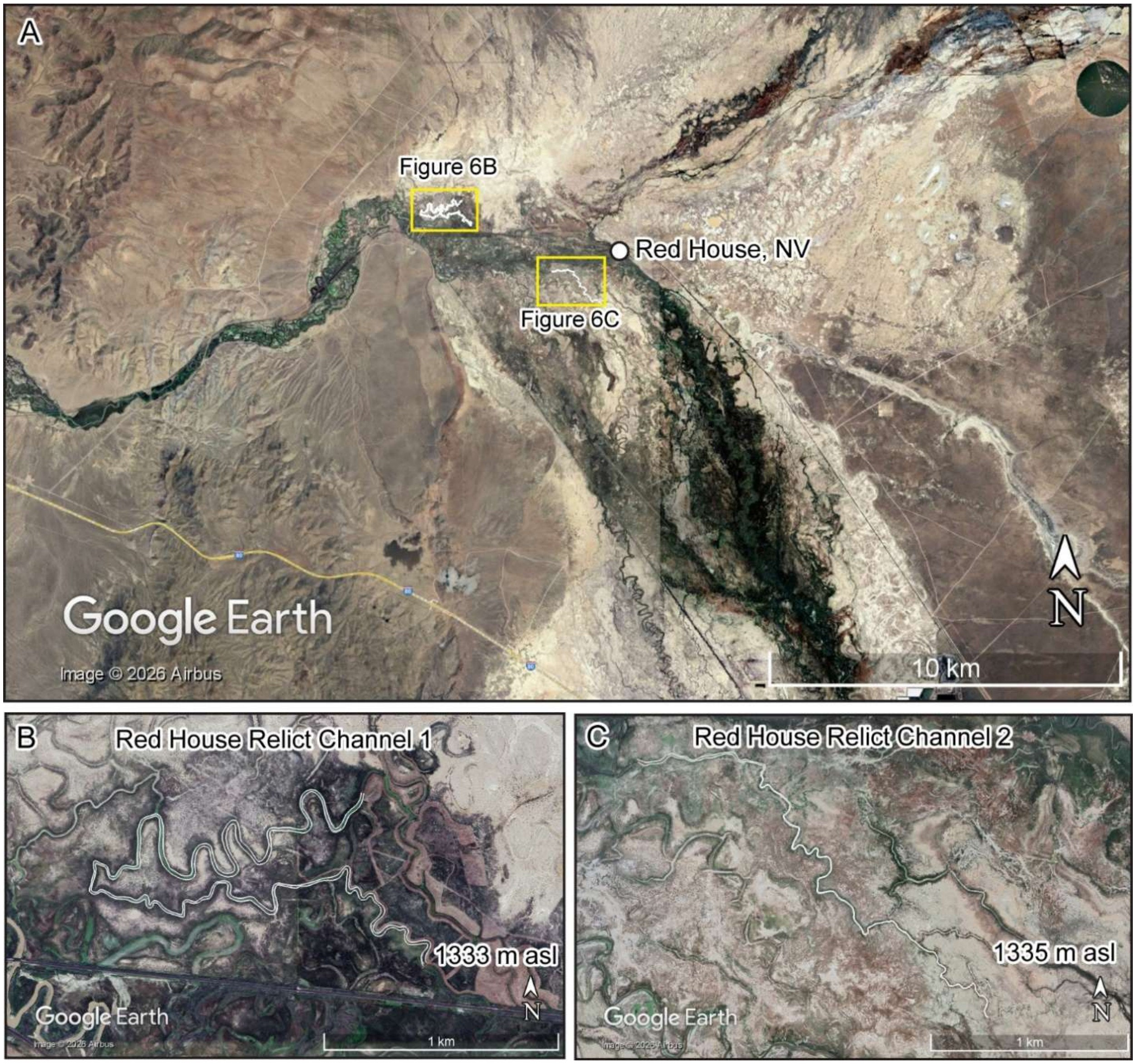

Figure 6. Overview maps of Red House Relict Channels 1 and 2. A) Regional overview of the Red House, Nevada (NV) area with yellow squares indicating the location of relict channels in B and C. B) Red House Relict Channel 1 at 1333 m above sea level; C) Red House Relict Channel 2 at 1335 m above sea level. White lines indicate the digitized bank lines.

(Figure 7A). The region has numerous paleochannels, oxbow lakes, and scrollbars. The Ganga Plains extend from Punjab in western India, southeastward along the frontal thrusts of the Himalayas into West Bengal and Bangladesh where the Ganges and Brahmaputra rivers join and ultimately flow into the Bay of Bengal (Vaidyanadhan & Ramakrishnan, 2010). The Ganga Plains represent the modern expression of the Himalayan foreland basin which has a long history of Cenozoic subsidence, filling, and uplift (Singh, 1996). The Maheshpur region falls within the upper delta plains of the Ganges-Brahmaputra delta in the Ganges fluvio-deltaic Plain Graben east of the

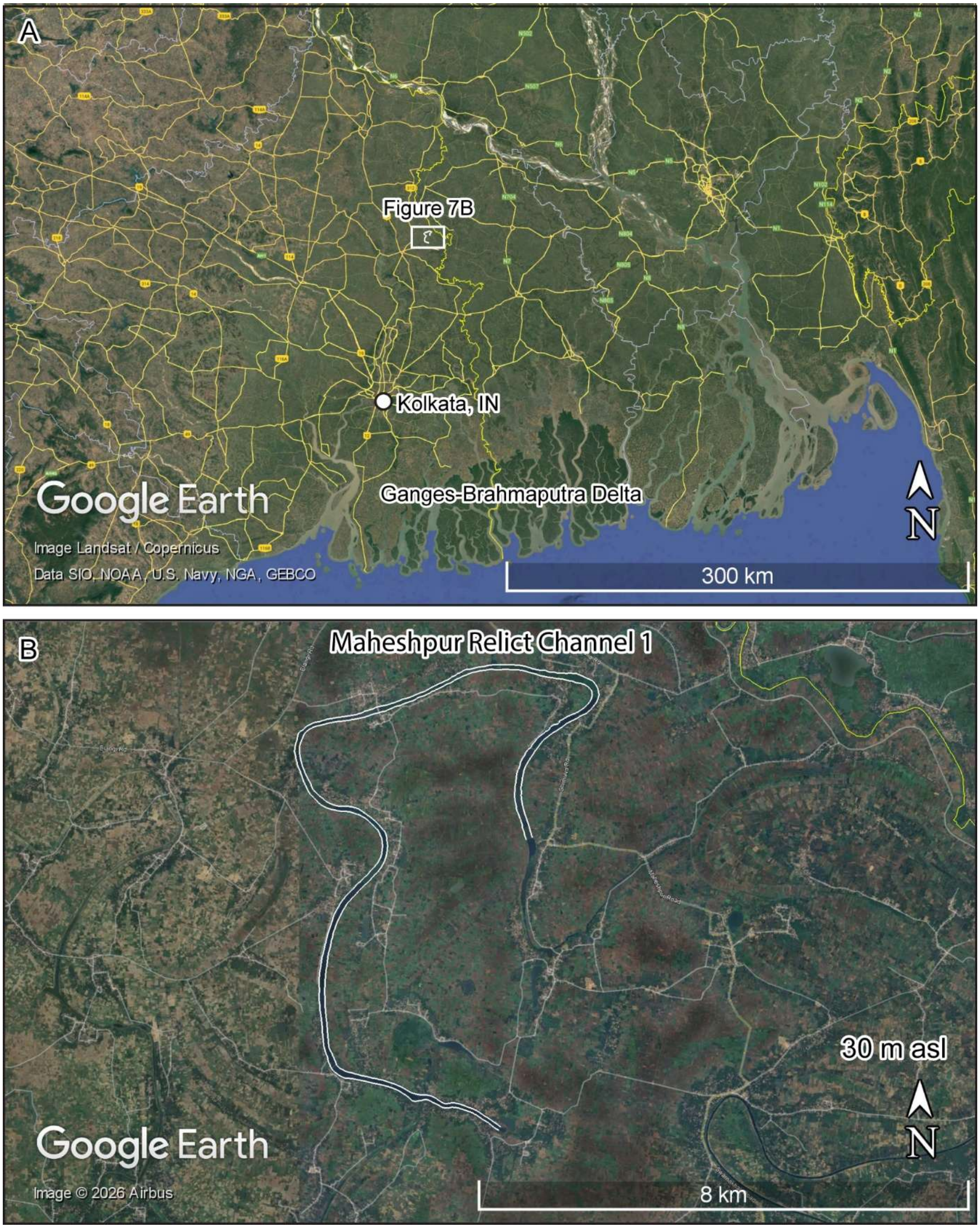

Figure 7. Overview maps of Maheshpur Relict Channel 1. A) Regional overview of the India/Bangladesh border and the Ganges-Brahmaputra Delta. White square indicates the location of the Maheshpur Relict Channel in B on the delta plain; B) Satellite imagery showing the Maheshpur Relict Channel at 30 m above sea level (asl) on the delta plain of the Ganges-Brahmaputra Delta. White lines indicate the digitized bank lines. IN = India

Damodar fault (Singh *et al.*, 1998; Tandon *et al.*, 2008; Kuehl *et al.*, 2011). Regional studies have largely focused on geomorphic units and terraces east of the Hooghly River, with the Maheshpur area west of the river falling within a broad classification of Moribund Ganga Deltaic Plain (Singh *et al.*, 1998). Geologic maps of West Bengal identify the surface geology of the Maheshpur region as Holocene alluvium (Geological Survey of India, 1999). Holocene alluvium in this region belongs to the morphostratigraphic

Bhagirathi units which have thermoluminescence ages ranging from of 1.0 to 6.7 ka (Singh *et al.*, 1998; Mukhopadhyay *et al.*, 2005).

We digitized a single relict channel in the Maheshpur region (Fig. 7B). The channel is approximately 30 m above sea level and is associated with eastern Middle-Late Holocene floodplains of the Bhagirathi and Hooghly Rivers (Geological Survey of India, 1999; Mukhopadhyay *et al.*, 2005). Paleogeographic reconstructions for the past 18 ka show that the depositional environment of the Maheshpur region has been active or incipient floodplains since 11 ka, with Holocene transgression and subsequent landward shoreline migration limited to the easternmost Ganges-Brahmaputra Delta (Goodbred & Kuehl, 2000). For this reason, we consider the Maheshpur Relict Channel 1 to be of likely fluvial origin.

Wagga Wagga. Australia

Wagga Wagga is a city in New South Wales, Australia, ~200 km west of Canberra (Figure 8A). It is located on the floodplain of the Murrumbidgee River that flows east across New South Wales to its junction with the Murray River east of Balranald. The geology of the region consists of deformed Ordovician-Devonian bedrock overlain by laterally extensive Quaternary floodplain alluvium (Wynn, 1977). The Quaternary alluvium accumulated on the floodplains of regional rivers and local streams that drain surrounding Paleozoic highlands.

We digitized a single relict fluvial channel, Wagga Wagga Relict Channel 1, on the surface of Holocene floodplains adjacent to the Murrumbidgee River ~44 km NW of Wagga Wagga, ~170 m above sea level (Figure 8B). Due to the long distance from the nearest shoreline(~360 km) and high elevation, we consider the Wagga Wagga Relict Channel 1 to be of likely fluvial origin.

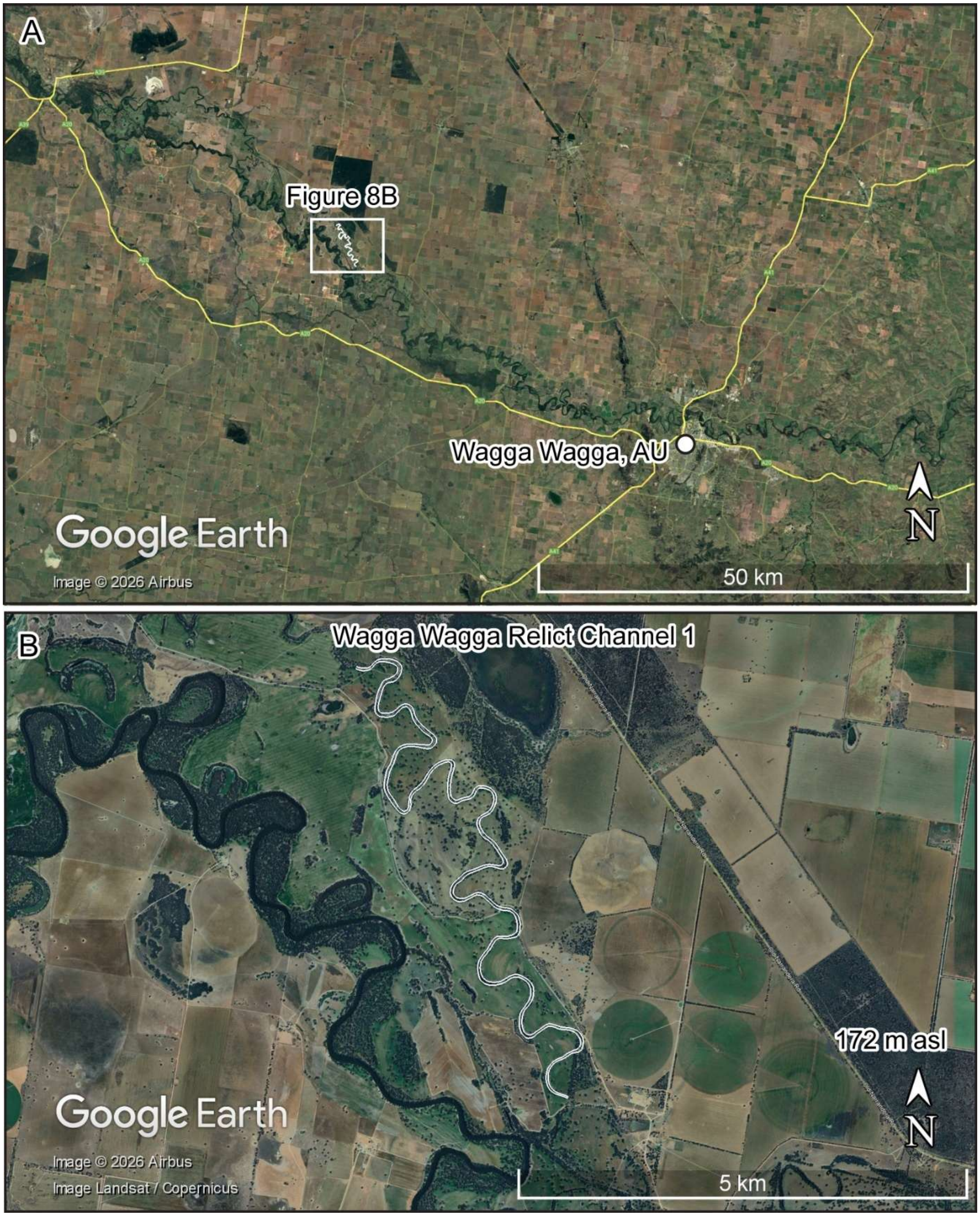

Figure 8. Overview maps of Wagga Wagga Relict Channel 1. A) Satellite imagery of the Wagga Wagga, Australia (AU) region with the location of the Wagga Wagga Relict Channel denoted by the white square. B) Wagga Wagga Relict Channel at 172 m above sea level. White lines indicate the digitized bank lines.

Woodville, Arkansas, USA

The Pine Bluff region of Arkansas (Figure 9A) is dominated by Quaternary alluvial deposits of the Arkansas River as it flows ESE toward the Mississippi River. Woodville is a small, unincorporated community located about 30 km ESE of Pine Bluff. This region hosts two main types of Arkansas River-derived deposits: Holocene point bar deposits, and Holocene backswamp/floodplain deposits (Saucier, 1994). Paleogeographic reconstructions show that the Mississippi River and Arkansas River valleys have been dominated by fluvial sedimentation in pre-Pleistocene to Holocene time, and there is no evidence of estuarine, marine, or deltaic deposition in the Arkansas River valley during this time (Saucier, 1994).

We digitized a single relict channel on the surface of the Holocene Arkansas River backswamp deposits of Saucier (1994). Woodville Relict Channel 1 (Figure 9B) lies south of the modern Arkansas River at an elevation of 60 m above sea level. Given the clear association with the Holocene Arkansas River and large distance from the modern coastline (~ 500 km), we consider this channel to have a high likelihood of a fluvial origin.

Methods

Channel digitization and processing

Relict channels were hand-digitized using high-resolution satellite imagery in Google Earth. Channel banks were delineated in imagery using clear bank topography, abrupt changes in vegetation, and abrupt color changes that indicate bank geometries. Mixed-energy channels were digitized from the mouth of the channel and past the inland tidal reach, using bankfull geometries indicated by clear water lines, vegetation, and bank topography. Processing of channel planforms follows steps outlined in Gardner and Dorsey (2025). Channel banks are converted into UTM and then processed in the R program "cmgo" to extract a centerline with regularly sampled width measurements (Golly & Turowski, 2017). The centerline is resampled at a spacing of $s = \overline{W}/100$, where $\overline{W}$ is the average width of the reach. At each point we calculate the principal channel metrics: normalized width (NW), normalized curvature (NC), normalized radius of curvature (NR), normalized width to normalized curvature ratio (NW/NC), the convolution of NR and NW (NRxNW), the convolution of NC and NW (NCxNW), and their first derivatives with respect to distance along the centerline (indicated here using prime notation, e.g., NW'). Each reach is subdivided into segments with a length (L) of $L = 2\overline{W}$. For each principal channel metric within a

Figure 9. Overview maps of the Woodville Relict Channel. A) Overview imagery of the Woodville and Pine Bluff, Arkansas (AR) region with the location of the Woodville Relict Channel indicated by the white square; B) the Woodville Relict Channel at 60 m above sea level (asl). White lines denote the digitized bank lines.

given segment, the mean, variance, standard deviation, minimum, maximum, median, midpoint, skewness, kurtosis, range, mean absolute deviation, intra-quartile range, and mode are calculated. Each segment also has a sinuosity value. Segments from each reach are then added to a matrix that contains all statistical variables from each segment and reach.

Classification via trained random forest classifiers

The relict and mixed-energy prediction matrices were used as input for the random forest classifier trained on a dataset of modern tidal and fluvial reaches (Gardner and Dorsey, 2025). The random forest classifier uses all statistical variables derived from the principal along-channel metrics NW, NR, NRxNW, NC/NW, NW', NR', NRxNW', and NC/NW' as well as sinuosity to differentiate between segment types. The classifier produces probability scores from individual trees in the random forest for each segment that are a measure of the model consensus that a given segment is tidal or fluvial (Breiman, 2001). In applying a model trained on modern tidal and fluvial segments to relict channel reaches, there is a domain shift between modern training data and relict prediction data. The classifications from trained random forest classifier of Gardner and Dorsey (2025) yielded a 100% reach-scale classification at the >50% classification threshold. This indicates that the uncalibrated segment-scale model output generalized well to the reach-scale using previously unseen data. Furthermore, we do not treat the forest-level output probability scores of individual segments as true numeric probabilities, for which calibration would be needed to map probability scores to actual frequency (Niculescu-Mizil & Caruana, 2005; Feng, 2021). Instead, we focus on reach-scale classification based on the dominant segment-type for a given reach and interpret the uncalibrated forest-level probability scores as measures of model consensus of segments within the reach (Breiman, 2001). We retain the uncalibrated forest-scale classifier output because we do not interpret the probability scores as true probabilities, and to ensure consistent methodology and continuity of the validated reach-scale classification scheme of Gardner and Dorsey (2025). We refer to the forest-scale classifier probability scores as model consensus scores (MCS) in this study avoid confusion with true probability. To improve clarity, the term prediction probability is strictly used for the probability scores produced by an individual decision tree within the random forest.

For a given individual decision tree, the prediction probability of each domain (tidal or fluvial) for a segment is calculated from the amount of training data samples from each domain that fell within the same terminal leaf node as the segment being classified (Breiman, 2001; Pedregosa *et* *al.*, 2011). Mathematically, for an individual tree this is $p_{tree}(tidal\ |x) = \frac{n_T}{n_T+n_F}$, where $p_{tree}(tidal\ |x)$ is the tidal prediction probability from a tree for a given sample, x, n_T is the number of tidal training samples in that leaf, and n_F is the number of fluvial training samples in that leaf (Breiman *et al.*, 1984; Pedregosa *et al.*, 2011). The fluvial prediction probability is calculated identically except n_F is in the numerator. For example, if the segment of interest in a particular decision tree lands in a leaf node which had 9 tidal training samples and 1 fluvial training sample, the prediction probability for that segment in that leaf would be $p_{tidal} = 0.9;\ p_{fluvial} = 0.1$, where p_{tidal} and $p_{fluvial}$ are the tidal and fluvial prediction probabilities, respectively. Across a random forest of T trees, the output MCS of the model is the average of the per-tree model prediction probabilities shown mathematically as $MCS_{forest}(k|x) = \frac{1}{T}\sum_{t=1}^{T} p_t(k|x)$, where $MCS_{forest}(k|x)$ is the output class (k) MCS for a given sample (x), T is the total number of trees in the forest, t is the index for an individual tree, and $p_t(k|x)$ is the output prediction probability of tree t for a given class (k) and sample (x) (Breiman, 2001; Pedregosa *et al.*, 2011). The MCS assigned by the whole random forest and the prediction probability from an individual tree to a segment must sum to one, therefore a segment with a 0.9 tidal MCS score would have corresponding fluvial MCS score of 0.1, and vice-versa. The classification of a given segment is determined by the model consensus scores with a threshold score of 0.5 (i.e. $MCS_{tidal} = 0.51$ yields a tidal classification for that segment). Conversely a segment with $MCS_{tidal} = 0.49$ would be classified as fluvial. Preliminary classification of entire relict channel reaches uses a simple majority (>50%) threshold, where the segment type assigned by the random forest that makes up >50% of all segments in the reach determines the reach-scale classification. These classifications are further considered in the context of all three classification thresholds (>50%, >66%, and >75%) by comparing the percentage of total segments within a reach that make up the dominant segment type to these threshold levels. Reach-scale classifications of modern mixed-energy channels are computed identically. However, binary classification of mixed-energy channels has limited use because these channels are neither wholly tidal nor fluvial. The value of mixed-energy channels comes from their model consensus score distributions and comparing them to those of relict channels. Spatial autocorrelation cannot be removed, as adjacent channel segments have a greater degree of autocorrelation than distant channel segments. Because we do not rely upon the classification of individual segments for spatial analysis and instead focus on dominant segment type for a reach, the effects are less prominent.

Model consensus score distributions

The distributions of paired tidal and fluvial model consensus scores for each segment provide additional context for the reach-scale classification. In this study we plot the histograms as probability densities (bin size = $\Delta MCS = 0.05$) of tidal model consensus scores for all segments in a given reach. Y-axes are independently scaled per-reach to emphasize the shape of the distribution within a reach. Each segment has a tidal model consensus score, and for each reach, we plot the tidal model consensus scores for all segments within the reach. A segment with a tidal MCS of 0.9 in the distribution has a corresponding numerically dependent ($MCS_{fluvial} = 1 - MCS_{tidal}$) fluvial MCS of 0.1. In this case, there is strong agreement between trees that the segment is tidal. In a case where a segment has a tidal MCS of 0.1, there is high consensus between trees that the segment is not tidal and is fluvial. A segment with a tidal MCS between 0.4-0.6 indicates there is disagreement between trees regarding the classification of the segment and is thus considered low consensus. For each channel reach, the distribution of tidal model consensus scores of all the segments within that reach reflects how consistently a model differentiates segments within that reach as either tidal or fluvial in the training space. A channel with a distribution of many high-consensus model consensus scores (e.g., 0.9 tidal or 0.1 tidal), and few low-consensus model consensus scores (e.g., 0.4-0.6 tidal) would appear as distributions with the mass of the data clustering around MCS of 0 or 1 indicating strong model consensus that the channel is fluvial or tidal, respectively. This indicates that individual trees had high consensus on the classification of segments, and minimal between tree disagreement across all segments. This suggests that the reach-scale classification is robust with respect to high model consensus levels. Conversely a channel with many low-consensus scores (0.4-0.6) and few high-consensus scores would have an MCS distribution with the bulk of the distribution close to 0.5 and would indicate that the classification of segments within that reach had widespread disagreement between trees. We plot the model consensus score distributions for each of the relict channels to evaluate the robustness of the reach-scale classification and provide additional context through corresponding model consensus score plots of modern tidal, fluvial, and mixed-energy channels.

Results

Classification of relict channels

Figure 10 is a color-coded bar graph of the 14 relict channels analyzed in this study, where the colors of the bar (red = fluvial; blue = tidal) are determined by the baseline classification, and bar heights represent the percentage of segments of that type within each reach. Within each classification group (tidal or fluvial) channels are ranked by decreasing percentage of the majority segment type. Horizontal lines represent the >50%, >66%, and >75% classification thresholds (displayed here in decimal form). Baseline reach-scale classification of relict channels is determined by the simple majority segment type within the reach. If a relict reach has >50% fluvial segments it is classified as fluvial, and the same for tidal.

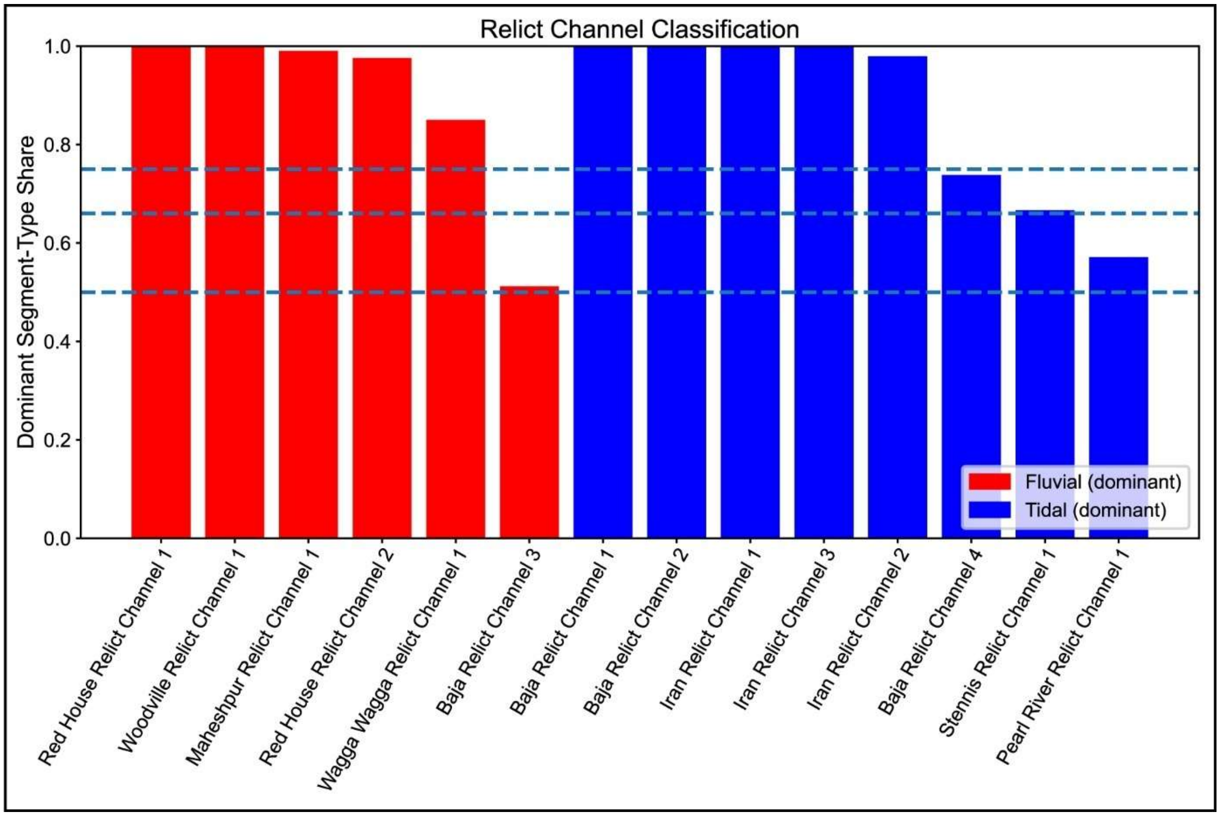

Figure 10. Bar plot showing the share of segments for each relict channel that match the dominant segment-type for a given reach. Eight reaches were classified as tidal and six reaches were classified as fluvial. Ten relict channels had >80% of segments classified as as either tidal or fluvial, while four relict channels had considerably lower dominant segment-type shares, suggesting lower confidence in these channels.

Of 14 relict channels analyzed, 6 were classified as fluvial and 8 were tidal (Fig. 10). Relict channels considered to be likely fluvial (Red House 1, Red House 2, Wagga Wagga, Maheshpur, and Woodville) were all classified as fluvial above the >75% classification threshold. 98–100% of segments in the Red House 1, Red House 2, Woodville, and Maheshpur relict channels were classified as fluvial. Baja relict channel 3, considered to be of unknown origin, was classified as fluvial with only 51% of segments matching that classification. Other relict channels considered to be of unknown origin (Baja 1, 2, and 4; Iran 1, 2, 3) were all classified as tidal, and relict channels considered likely fluvial or potentially tidal (Stennis and Pearl River) were also classified as tidal (Fig.

10). 100% of segments in Baja relict channels 1 and 2, and Iran relict channels 1 and 3, were classified as tidal, while 98% of segments in Iran relict channel 2 were classified as tidal. Baja relict channel 4 had 74% of segments classified as tidal. Stennis relict channel 1 had 67% of its segments classified as tidal, and Pearl River relict channel 1 had 57% of segments classified as tidal.

Ten relict channels (5 fluvial, 5 tidal) exceeded the >75% classification threshold, with up to 100% their segments having a classification that matches the reach-scale classification. Four channels (1 fluvial, 3 tidal) fell below the >75% classification threshold. These four channels have considerably fewer segments that match their reach-scale classification compared to the 10 high-percentage channels.

While the dominant segment-type reach-scale classification of relict channels is the principal metric used to assign an origin to the studied reaches, there are important variations in the dominant segment type among the studied reaches. This indicates that some reaches are composed almost entirely of segments with geometries consistent with the dominant segment type, while other reaches have considerably fewer consistent segments. The classification bar plot in Figure 10 shows that for 10 of 14 relict channels, a significant portion of segments (>80%) match the dominant segment type. Despite surpassing the >50% classification threshold for their given classifications, Baja relict channels 3 and 4, the Pearl River relict channel, and Stennis relict channel all had considerably fewer segments that matched the dominant segment type. It is notable that even with the effects of spatial autocorrelation, the classification is robust and channels demonstrate variability in the dominant segment type within a reach. To better understand the reach-scale classification and sources of uncertainty, it is helpful to characterize the model consensus scores of segment-scale data for each reach.

Model consensus score (MCS) distributions of relict channels

Figure 11 shows the density distributions of tidal model consensus scores (MCS) for the 14 relict channels analyzed in this study relative to the consensus score classification threshold (0.5). A low model consensus zone is defined as consensus scores between 0.4 and 0.6, and each segment contributes a tidal MCS. The MCS distributions can be broadly grouped into three categories: (1) High consensus scores (~0 or 1) with minimal to no low consensus scores (0.4-0.6); (2) Moderate consensus (0-0.4, 0.6-1) with a greater density of low-consensus MCS (0.4-0.6); and (3) distributions with a center of mass near low-consensus MCS (0.4-0.6) and few to no high-consensus scores (0 or 1). Table 1 shows the relict channels that fall into each distribution category, and the percentage of segments in each reach that match the dominant-segment type for that reach.

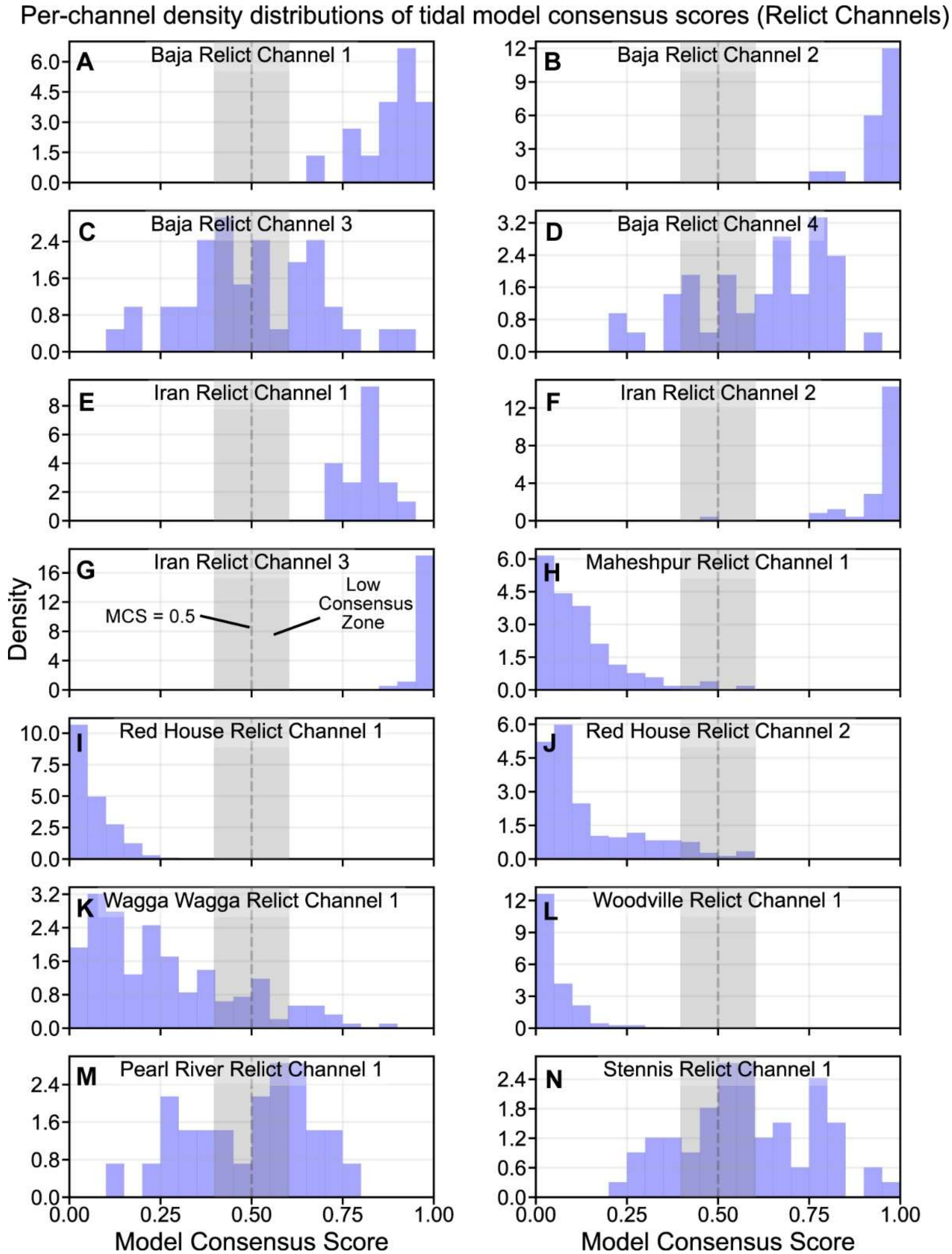

Figure 11. Density distributions of tidal model consensus scores (MCS) for each segment, by channel. A,B) Baja Relict Channels 1/2 showing clear distribution centered on high tidal consensus scores; C) Baja Relict Channel 3 showing a distribution with mass centered near low-consensus scores (~0.5) and a tidal classficiation; D) Baja Relict Channel 4 showing distribution centered around moderate tidal consensus scores with considerable density in the low-consensus score range; E-G) Iran Relict Channels 1-3 displaying distributions centered around high tidal consensus scores; H,I,J) Maheshpur Relict Channel 1, and Red House Relict Channels 1-2 displaying distributions centered around tidal consensus scores near 0, indicating strong fluvial consensus; K) Wagga Wagga Relict Channel 1 showing high fluvial consensus, with minor ambiguous-consensus scores (~0.5); L) Woodville Relict Channel 1 showing high fluvial consensus. M,N) Pearl River and Stennis Relict Channels showing distributions centered around low-consensus scores, with distributions weakly favoring a tidal classification.

Table 1: List of relict channels within each distribution category, including the percentage of segments that match the dominant type in parentheses

1: Abundant high-consensus scores (~0 or 1), minimal to no low consensus scores (0.4-0.6)	2: Abundant moderate-consensus scores (0-0.4; 0.6-1); with increased low-consensus scores (0.4-0.6)	3: Abundant low-consensus scores (0.4-0.6) and little to no high-consensus scores (~0, 1)
Baja Relict Channel 1 (100%)	Baja Relict Channel 4 (74%)	Baja Relict Channel 3 (51%)
Baja Relict Channel 2 (100%)		Pearl River Relict Channel 1 (57%)
Iran Relict Channel 1 (100%)		Stennis Relict Channel 1 (67%)
Iran Relict Channel 2 (98%)		
Iran Relict Channel 3 (100%)		
Maheshpur Relict Channel 1 (99%)		
Red House Relict Channel 1 (100%)		
Red House Relict Channel 2 (98%)		
Wagga Wagga Relict Channel 1 (85%)		
Woodville Relict Channel 1 (100%)		

Channels with dominant segment-type shares >75% all have distributions that fall into category 1. These channels display pronounced consensus with MCS grouping near 0 or 1, indicating that the random forest classifier produced high model consensus for these reaches and their assigned classifications. Within category 1 distributions, the MCS typically display few to no low consensus scores (0.4-0.6). The exception to this is Wagga Wagga relict channel 1 (Fig. 11K), which had a dominant segment type share of 85%. The Wagga Wagga relict channel displays the greatest density of scores around 0.4-0.6 in the category-1 channels. The channels with high-consensus scores and minimal low-consensus scores appear to retain the geometric characteristics of their modern class-type equivalents and have clear model consensus across all segments. In such cases, we consider the reach-scale classification of these relict channels to be robust.

All remaining relict channels have dominant segment-type shares below 75% and MCS distributions that place them in categories 2 and 3. Baja Relict Channel 4, with a dominant segment-type share of 74%, is the only channel in category 2 (Fig. 11D). The distribution of MCS for this channel forms a cluster that is neither ambiguous (0.4-0.6) nor robust (0 and 1), but the ambiguous MCS values are not sufficient to mask the overall moderate consensus. In this case, the random forest classifier may have had disagreements between decision trees that arrived at different classifications or landed on terminal leaf nodes that had a mixture of tidal or fluvial training samples with a greater abundance of tidal training samples. In either explanation, the geometric characteristics of this channel produced moderate MCS values in favor of a tidal classification despite ambiguity in some segments. The reach-scale classification is still considered valid, but additional field data would be needed to validate this classification.

Relict channels with lower dominant segment-type shares fall into MCS category 3, with a distribution that has central tendency in the range of ambiguous scores (0.4-0.6) (Fig. 11). These channels have a high density around low-consensus MCS, and few or no high MCS values. This suggests that a significant portion of segments in these reaches have geometries that yield widespread between-tree disagreements or landed on terminal leaf nodes with a high proportion of both tidal and fluvial training samples (low differentiability). The trained random forest classifier of Gardner and Dorsey (2025) produced dominant segment-type shares that, when used with a >50% classification threshold, accurately classified 100% of modern tidal and fluvial reaches that were tested. Following this classification approach, the reach-scale classifications of relict channels with low dominant segment-type shares may be considered valid. However, consideration must be given to possible causes for ambiguous consensus scores, and in these cases additional field evidence would be needed to test and verify the classification.

Discussion

MCS distributions of modern channels

The model consensus scores for relict channels (Fig. 11) indicate that in cases where a relict reach has a dominant segment-type share >75%, the trained random forest classifier produces high model consensus scores (~0 or 1) for a majority of segments. In contrast, for reaches with lower dominant segment-type shares, the random forest classifier produces numerous low-consensus MCS that reveal ambiguous geometric characteristics. It is important to evaluate the controls on this pattern. Comparing MCS distributions of relict channels with those from modern tidal, fluvial, and mixed-energy channels allows us to assess whether distributions for relict channels are: (1) potentially unique to the relict domain, (2) a product of natural geometric non-uniqueness between tidal and fluvial channels, (3) the product of mixed-energy processes during formation, or (4) represent an intermediate step during active modification of a channel planform from one domain to another (prior to channel abandonment). To test these hypotheses, we plot the density distributions of tidal model consensus scores for two modern mixed-energy channels and four modern tidal and fluvial channels (Fig. 12), where each segment contributes a single MCS.

Figures 12A and 12B show the distributions of model consensus scores for two modern mixed-energy estuary channels, one each at the mouths of the Coquille and Siuslaw Rivers in western Oregon, USA. The Coquille River channel displays a clear distribution with most data clustered near high-consensus MCS values in support of a fluvial classification (e.g MCS ≈ 0). There is a distinct zone of low-consensus MCS and infrequent moderate-consensus tidal segments. The Siuslaw River (Figure 12B) displays a less pronounced consensus. The data cluster around moderate-consensus MCS values in favor of a tidal classification, but with considerable density of low-consensus and high-consensus fluvial segments. Thus, it appears that modern mixed-energy channels produce low-consensus MCS overlaps similar to those observed in some of relict channels (e.g., Figs. 11 C, D), suggesting a possible mixed-energy control on the formation of some relict channels. The clustering of data around low-consensus scores may reflect non-unique channel geometries due to simultaneous shaping by tidal and fluvial processes.

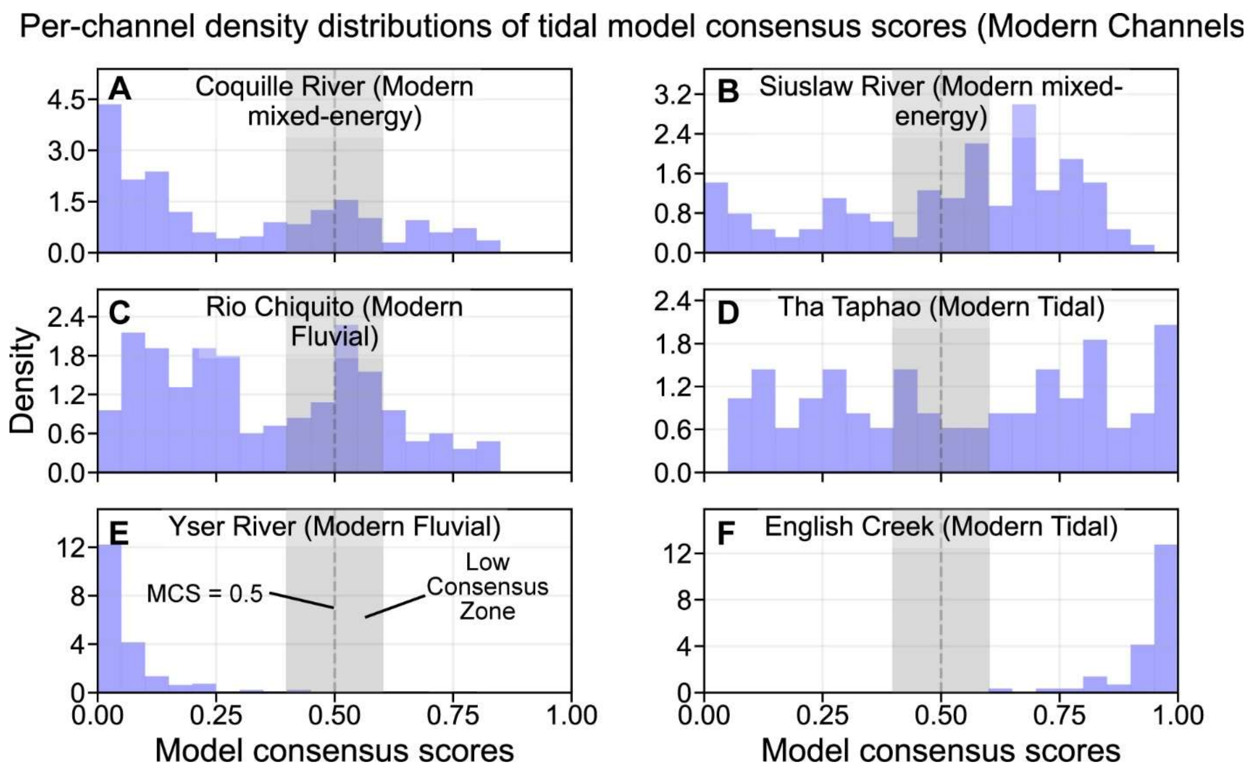

Figure 12. Tidal and fluvial model consensus score (MCS) density distributions for example modern mixed-energy, tidal, and fluvial channels. A,B) Coquille and Siuslaw River mixed-energy channels with moderate to high consensus scores, and some low-consensus scores due to mixed-energy processes; C, D) Rio Chiquito and Tha Taphao, modern fluvial and tidal channels that retain high-consensus scores for their respective domain, but with significant low-consensus MCS values from natural non-uniqueness of channels; E,F) Yser River and English Creek, modern tidal and fluvial channels with high-consensus MCS distributions, suggesting unique geometries and high model consensus across the reach.

Figure 12C shows the MCS distribution for the Rio Chiquito modern fluvial channel in Nicaragua. Like the Coquille River, Rio Chiquito displays clear high-consensus scores in favor of a fluvial classification, considerable overlap of moderate-consensus tidally classified segments, and significant clustering of data around low-consensus. The MCS distribution for the Tha Taphao modern tidal channel (Fig. 12D) displays a nearly uniform distribution of tidal MCS with the majority of the mass centered around moderate to high-consensus scores in favor of a tidal classification. Because Rio Chiquito was shaped entirely by fluvial processes and Tha Taphao was shaped entirely by tidal processes, the abundance of low-consensus scores (0.4-0.6) likely reflects naturally occurring non-uniqueness of tidal and fluvial channel geometries, rather than mixed-energy processes. This offers another potential explanation for the observed overlap in some relict channels (Fig. 11). Figures 12E and 12F show MCS distributions for the modern Yser River fluvial channel and modern English Creek tidal channel. These channels display concentration of high-consensus scores in favor of their respective true channel types (~0 = fluvial; ~1 = tidal), with no no low-consensus scores. These are cases where the modern channels geometries are unique to their respective domains. Reach scale classification of relict channels with similar high-consensus scores is equally straightforward.

Evolution of relict channel geometries

When channels are abandoned, the processes that originally formed them cease to be the dominant process shaping the channel. Previous studies use the term "terrestrialization" to characterize the transformation of river channels after they are abandoned, which is controlled by the rate of sediment infilling, lowering water levels, and frequency of re-flooding (Saucier, 1994; Dieras, 2013; Dépret *et al.*, 2017; Alam *et al.*, 2025). Post-abandonment changes in surface area, width, and length for the aquatic portion of abandoned channels has been documented in naturally and artificially abandoned channels (Dépret *et al.*, 2017). For a period of time after abandonment, a decrease in discharge leads to narrowing of the channel by lateral accretion, and abandoned channels may experience episodic flow from underfit streams that can meander within the course of the larger abandoned channel, thus masking the original full-flow configuration of the abandoned channel (Saucier, 1994). A study of Holocene climate changes based on relict channels showed that channel and floodplain configurations were stable when flooding magnitude was small, and floodplain stability decreased with increased flooding frequency or magnitude (Knox, 1985). Subsurface flow such as seepage, sapping, and pipe flow have been attributed to erosion both in hillslopes and on stream banks, acting as another mechanism for planform modification of abandoned channels (Fox & Wilson, 2010)

The post-abandonment evolution of tide-dominated channels is poorly understood. Recent advances have shown that, unlike fluvial channels, Holocene tide-dominated channels are abandoned by upstream sediment accumulation that results in rapid infilling (Gugliotta *et al.*, 2021). Tide-dominated channels in delta environments alternate between sediment accumulation and erosion on a seasonal basis (Wu *et al.*, 2020). More work is needed to better understand the post-abandonment evolution of tidal channels. While rapid infilling may help to preserve relict tidal channels, the loci of infilling and erosion during alternating seasonal phases has the potential to alter the planform geometries of abandoned tidal channels from their original configuration. Additionally, abandoned tidal channels may be subject to some of the same processes and planform alterations as abandoned fluvial channels, adding another potential source of non-tidal and non-fluvial geometries.

Although post-abandonment processes are part of active fluvial and tidal systems, they are not the principal processes that shape modern active channels in each domain. Post-abandonment processes can produce changes in width and length of relict channels, which are critical components for describing the geometry of these channels. If the observed relict channel geometries have been significantly altered from their original configuration the subsequent geometries, as seen through the lens of a classifier trained on modern fluvial and tidal channels, they may appear to be unlike both tidal and fluvial channels. For a classifier trained on modern channels that applies a binary classification, relict channels that have undergone planform alteration during the post-abandonment phase could produce ambiguous, low-consensus model consensus scores. As a result, relict channels with model consensus score distributions centered around low-consensus scores (0.4-0.6) may represent channels with geometries that reflect neither tidal nor fluvial processes due to post-abandonment planform alteration.

Long-term uplift of tidal channels presents the potential for a unique type of planform evolution in cases where the channel remains active during the transition from one type to the other. When uplift first starts, tidal channels can be expected to retain planform geometries characteristic of the tidal domain. With continued uplift, the channel emerges out of the tidal realm and enters the fluvial domain. With sufficient precipitation and runoff, flow in the former tidal channel may behave like flow in a river channel. Over time, fluvial processes acting on an uplifted tidal channel may reshape the planform and eventually produce fully fluvial geometries once the planform equilibrates to the fluvial domain, prior to abandonment. Intermediate planforms analyzed at timesteps between initial uplift and full planform re-equilibration could lead to a spectrum of intermediate tidal and fluvial geometries. A similar process may occur in reverse for fluvial channels that experience a rise of relative sea level that forces the channel to transition from the fluvial domain to the tidal domain. Studies related to this domain change are primarily focused on the fluvial-to-tidal transition in modern estuaries (a lateral transition), and the transition from fluvial to estuarine conditions as seen in the stratigraphic record (e.g., Dalrymple et al., 2015; Greb & Martino, 2009).

When discussing changes to the channel planform that occur during a domain shift, we use the term reshaping. This is a broad term that covers a number of mechanisms that could potentially modify channel planforms, including erosion and deposition. Comparisons of meander asymmetry between unidirectional and bi-directional flow conditions have demonstrated that fluvial channels (i.e. unidirectional flow) tend to produce meanders with maximum curvatures that are upstream skewed, while tidal channels (i.e. bi-directional flow) tend to produce more symmetrical meanders (Fagherazzi *et al.*, 2004; Finotello *et al.*, 2020). Maximum curvatures have been shown to play a significant role in river meandering (Sylvester *et al.*, 2019). Upstream- or downstream-directed changes in the location of maximum curvature driven by changing flow directionality could alter the loci of erosion and deposition within a channel undergoing a domain shift and thus change the morphology of meanders.

Channel planforms may also be modified by changes in bank strength during a domain shift. The degree and type of vegetation on the banks and cohesion of bank sediment play a critical role in the erosive resistance of banks, and changes to bank strength have been demonstrated to produce changes in channel width by a factor of three (Huang & Nanson, 1998). A domain shift may produce changes in the type and amount of vegetation present on channel banks, or it may result in a period of minimal vegetation as freshwater vegetation or marine vegetation dies due to ecological changes. These changes may bolster or weaken bank strength, in turn influencing the resistance of channel banks to erosion and associated changes to channel planform. Tidal environments and distal fluvio-deltaic systems typically have large proportions of cohesive fine-grained sediments such as mud (Bhattacharya, 1992; Hughes, 2012). Because cohesive muds increase bank strength, fluvio-deltaic channels and tidal channels undergoing domain shift may be resistant to planform change by erosion during early stages of the domain shift. For channels with smaller proportions of mud such as those in fan deltas and braid deltas (McPherson *et al.*, 1987), weaker banks may be expected to undergo planform changes at a faster rate.

Changes in flow regime during a domain shift may also play a role in planform modification. Bedforms produced by subcritical flow ($Fr < 1$) are well-studied and easily identified in tidal and fluvial environments in modern settings and in the depositional record (Allen, 1982; Hughes, 2012).

In recent years, greater attention has been given to stable and unstable bedforms produced by supercritical flow (Cartigny *et al.*, 2014; Ono *et al.*, 2021; Slootman *et al.*, 2021). Studies have recognized supercritical flow structures forming under unidirectional flow conditions in flumes, variable-discharge fluvial systems, Gilbert-type deltas, carbonate ramps, deep-water marine settings, and even in glacial environments (Cartigny *et al.*, 2014; Dietrich *et al.*, 2016; Covault *et al.*, 2017; Lang *et al.*, 2017; Fielding *et al.*, 2018; Slootman *et al.*, 2019; Ono *et al.*, 2021). Bedforms indicative of supercritical flow conditions have been documented in the intertidal zone, but are attributed to wave backwash and wave-wave interaction rather than to bi-directional tidal flow conditions (Vaucher *et al.*, 2017). River discharge is considerably more stochastic and variable compared to the predictable and periodic changes to the volume of the tidal prism (Kvale *et al.*, 1995). Supercritical conditions are common in variable-discharge rivers, but not tidal settings (Fielding *et al.*, 2018). A channel that has undergone a domain shift may thus experience increased (tidal-to-fluvial) or decreased (fluvial-to-tidal) frequency of supercritical flow conditions. The formative conditions that affect sediment transport would be significantly altered from the original domain, which will lead to a change the type of bedforms expected in the channel. These mechanisms have the potential to drive changes to the channel planform during a domain shift.

Figure 13 illustrates a conceptual model for the potential effect of tidal-to-fluvial or fluvial-to-tidal domain shifts on the distribution of model consensus scores for a channel planform analyzed and classified at different time steps. At initial formation of a channel in its original domain, the distributions are predicted to have distributions centered around high-consensus scores for that domain. At subsequent time-steps following the active domain shift, MCS distributions display decreased model consensus, evolving to a mid-point where the distribution is centered around low-consensus scores (0.4-0.6).

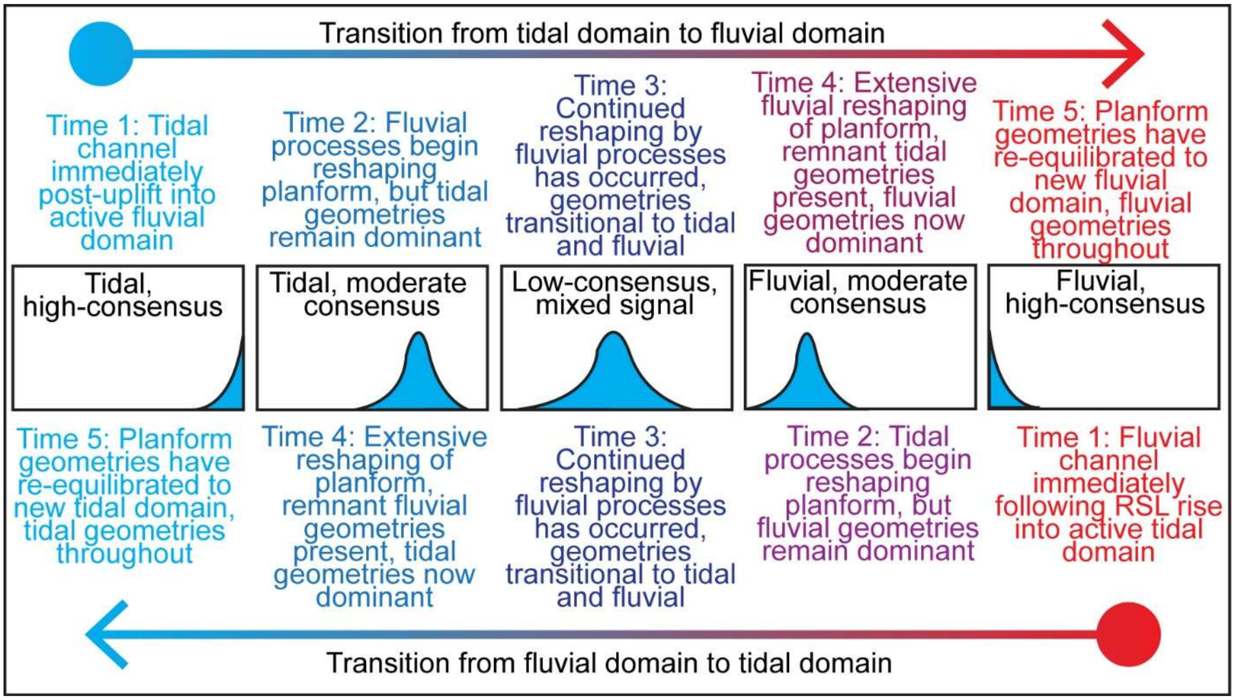

Figure 13. Conceptual diagram of possible model consensus score distributions for relict channel geometries analyzed at end-member and intermediate time-steps due to progressive re-shaping of initial channel geometries during a tidal-to-fluvial or fluvial-to-tidal domain shift prior to abandonment.

Subsequently, with continued re-shaping in the new domain, consensus score distributions display increasing bimodality with less low-consensus overlap. When the planform reaches full equilibrium with its new domain, the consensus score distribution would again have clear bimodality and high-consensus scores consistent with the new domain. If a channel is abandoned at any time-step in this sequence, and in the absence of post-abandonment modification or non-unique geometries, the MCS distributions of a relict channel may resemble configurations in Figure 13. This scenario has not been previously documented, and testing of this conceptual model would require data and analyses beyond the scope of this study. However, a tidal-to-fluvial or fluvial-to-tidal domain shift offers another potential explanation for moderate to low consensus distributions (Fig. 11). Low-consensus MCS values in this model would be the product of both fluvial and tidal influences occurring at different times, which is distinct from mixed-energy settings where fluvial and tidal processes occur simultaneously.

In summary, we suggest that the low-consensus score distributions observed in four of 14 relict channels analyzed in this study (Fig. 11) may result from one or more of the following factors: (1) non-unique geometries due to shaping of the channel planform by simultaneous fluvial and tidal processes (e.g., mixed-energy systems); (2) non-unique geometries from the naturally occurring geometric overlap between the two channel types; (3) modification of the channel planform by post-abandonment processes that yield geometries unlike modern tidal or fluvial channels; or (4) non-unique geometries produced during a tidal-to-fluvial or fluvial-to-tidal domain shift driven by changes in relative sea level while the channel is still active.

Paleo-sea level reconstructions

This study was motivated in part by the potential to use relict tidal channels as paleo-sea level markers. Because tidal channels form at or near sea level, recognition of a relict tidal channel above sea level requires a post-abandonment fall in relative sea level due to either crustal uplift or a fall in global sea level (Fig. 1). The height of the sea surface is known to vary up to 20 km relative to a reference sphere in response to variations in earth's gravitational field, gravitational effects of ice sheets, vertical crustal movements from flexural loading and unloading, local subsidence, and earth's rotation (de Boer *et al.*, 2017; Le Bars *et al.*, 2019; Kurtze, 2022; Brandes *et al.*, 2025). Nonetheless, a robust general model exists for global sea level change over the past ~800 ky based on marine isotopes, inverse ice sheet modeling, and Mediterranean relative sea level records (Bintanja *et al.*, 2005; Lisiecki & Raymo, 2005; Sosdian & Rosenthal, 2009; Elderfield *et al.*, 2012; Rohling *et al.*, 2014; Shakun *et al.*, 2015; Spratt & Lisiecki, 2016). We use results from Spratt & Lisiecki (2016), who performed a principal component analysis that calculates the average of five sea level records to derive a single combined global sea level curve, or "stack", and the 95% confidence interval for the signal (Fig. 14).

Elevations of relict tidal channels can be compared to the record of global sea level change through time to evaluate local changes in relative sea level. To do this, we need relict channels that have been assigned a tidal origin (we use the >50% threshold) and have a known reliable age or age range of formation. The reach-scale classification derived from the trained random forest classifier assigned a tidal origin to 8 of the 14 relict channels analyzed in this study, with estimated ages ranging from 112 ka to 798 ka based on U-Th geochronology, Amino Acid Racemization (AAR), faunal assemblages, O^{18} isotopes, thermoluminescence dates (Ortlieb, 1991; Otvos, 2005), and as inferred from regional average uplift rates (Berberian, 1995). The elevation of the Iran Relict channels (55 m) and average regional uplift rate (1mm/yr; Berberian, 1995) suggest they were at or near modern sea level around 55 ka. However, these channels are not included in the following analysis because there are no published independent age estimates for them. For the other relict tidal channels, we calculate a range of possible values for post-abandonment uplift or subsidence by subtracting using minimum and maximum elevation differences between the elevation of the relict channel and the upper and lower bounds, respectively, of the 95% confidence interval for the sea level curve at the time-steps where the difference is minimized and maximized (Fig. 14).

Figure 14 shows the elevation and age range for five relict channels (this study) compared to changes in global sea level over the past ca. 800 ky (Spratt & Lisiecki, 2016) (Table 2). Yellow boxes bracket the range of implied vertical crustal motion (red arrows) from the time of channel formation to the present. The wide range of possible vertical displacements illustrates the strong dependence on channel age, age uncertainty, and large variations in global sea level through time. Because modern sea level is near the highest level recorded over the past 800,000 years, most relict channels preserved above sea level require post-abandonment uplift. The Stennis and Pearl River sites in the Gulf coast region permit some scenarios for large uplift (100 – 150 m) since channel abandonment. However, based on records of glacially modulated forebulge migration and Holocene regional

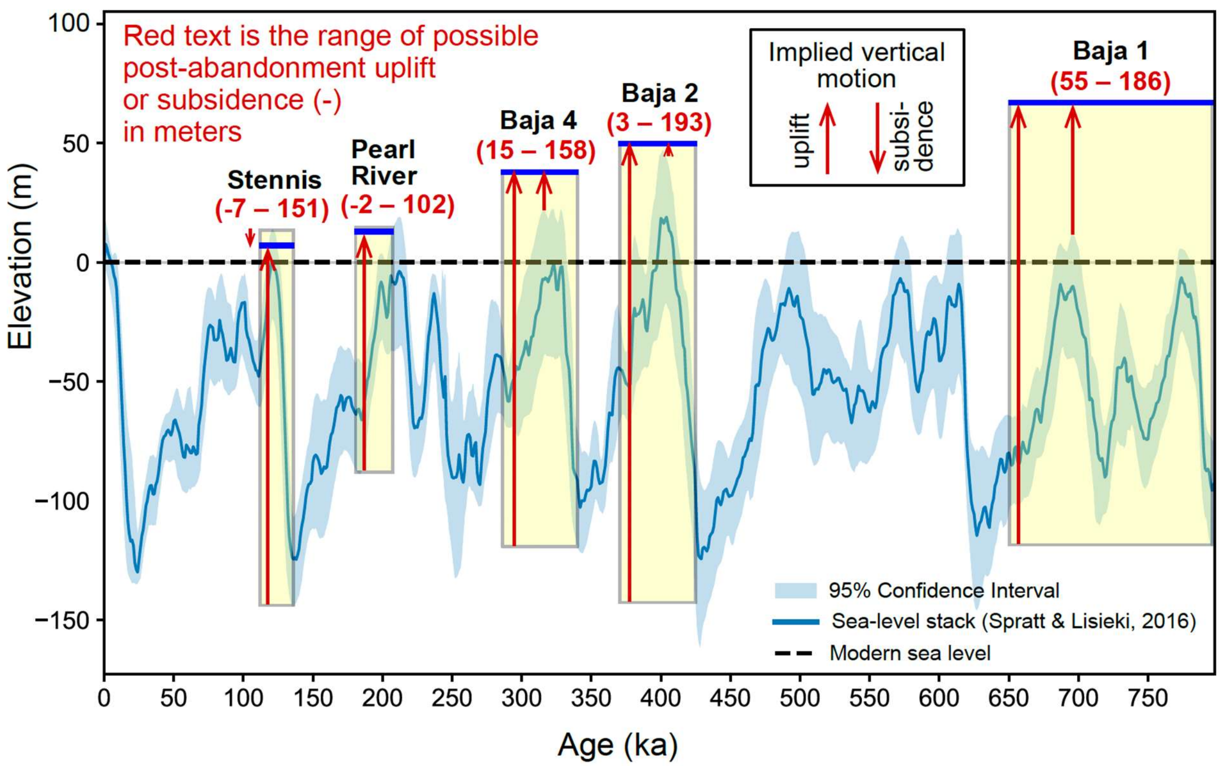

Figure 14. Sea level curve of Spratt & Lisiecki (2016) showing elevation, ages, and implied post-abandonment uplift (or subsidence) for relict channels assigned a tidal origin in this study. Iran relict channels are excluded due to lack of independent age control. Blue horizontal bars show the likely age range for each relict channel (see text for details) placed at their present-day elevation. Yellow shaded boxes are used to bracket the range of implied vertical crustal motion (red arrows) from the time of channel formation to the present. Because modern sea level is near the highest level recorded over the past 800,000 years, most relict channels preserved above sea level today require post-abandonment uplift. The Stennis and Pearl River sites include some scenarios for minor subsidence or no change. The wide range of possible vertical displacements illustrates the strong dependence on channel age, age uncertainty, and large variations in global sea level through time.

subsidence (e.g., Blum & Roberts, 2009; Brandes et al., 2025), we favor interpretations that involve minor vertical motion or no change in this region (Fig 14).

Calculated uplift values for the three Baja relict channels generally increases with increasing age, with large uncertainty, which is expected in this region where slow uplift has been documented for middle to late Pleistocene time (Ortlieb, 1991). However, the wide range of plausible paleo-sea levels associated with the range of ages for the Baja relict channels limits our ability to calculate meaningful uplift rates or changes in rate through time.

Table 2. Relict channel names, present-day elevation, assigned age ranges, minimum and maximum elevation differences between the relict channel elevation and the upper and lower bounds, respectively, of the 95% confidence interval for the sea level curve, and corresponding ages for each of the five relict channels in Figure 14. Ages for Baja relict channels are derived from ages of equivalent elevation terraces in Punto Abreojos, Baja California Sur, Mexico dated using combined U-Th, AAR, faunal assemblages and O^{18} isotopes (Ortlieb, 1991). Min. elev. diff = minimum elevation difference; max. elev. diff. = maximum elevation difference; OSL = Optically Stimulated Luminescence; Allofm. = Alloformation; P. Ab. = Punto Abrejos; MM = Multi-Method

Relict Tidal Channel Name	Elevation (m asl)	Age Range (ka)	Min. elev. diff. (m) and age (ka)	Max elev. diff. (m) and age (ka)	Age Range Source
Stennis Relict Channel 1	7	112-136	-7 m (121 ka)	151 m (136 ka)	Otvos (2005) OSL Hammond Allofm.
Pearl River Relict Channel 1	13	180-208	-2 m (208 ka)	102 m (184 ka)	Otvos (2005) OSL Gum Bayou Allofm.
Baja Relict Channel 4	38	285-340	15 m (316 ka)	158 m (340 ka)	Ortlieb (1991) MM P. Ab. Terraces
Baja Relict Channel 2	50	370-425	3 m (402 ka)	193 m (425 ka)	Ortlieb (1991) MM P. Ab. Terraces
Baja Relict Channel 1	67	650-798	55 m (695 ka)	186 m (796 ka)	Ortlieb (1991) MM P. Ab. Terraces

The Stennis and Pearl River relict channels have negative values for minimum elevation difference (relict channel elevation minus upper bound of 95% confidence interval where difference is lowest) which means that the channels fall within the 95% confidence interval of the global sea level curve and no uplift or subsidence is needed to explain their present elevation. Maximum elevation differences (relict channel elevation minus lower bound of the 95% confidence interval where the difference is greatest) for the Stennis and Pearl River relict channels are 151 m and 102 m, respectively, which means that if these channels formed at sea level during global sea level lows within their age ranges, they may have experienced 151 m and 102 m of uplift after abandonment. Baja relict channels 1, 2, and 4 have positive minimum elevation differences ranging from 3-55 m. This means that global sea level fluctuations alone cannot place these channels within the 95%

confidence interval at their present elevation, and therefore at least 3 m of uplift must have occurred since channel formation.

Maximum elevation differences for Baja relict channels 1, 2, and 4 correspond to global sea level lowstands overlapping with their formation age range. If these channels formed during sea level lowstands, 158-193 m of uplift would be implied to explain their present elevations. The maximum uplift estimates for relict tidal channels analyzed here represent plausible end-member cases in which the channels formed during global sea level lowstands. The range of potential relative sea level change for each channel is shown in Table 3

Table 3. Estimates of Relative Sea Level (R.S.L.) fall for relict tidal channels using elevation differences between present-day elevation and the 95% confidence interval bounds for the sea level curve of Spratt & Lisiecki (2016). Negative values imply subsidence or no change needed to form at sea level and reach present elevation.

	Stennis Relict Channel 1	**Pearl River Relict Channel 1**	**Baja Relict Channel 4**	**Baja Relict Channel 2**	**Baja Relict Channel 1**
Range of Relative Sea Level Change (m)	-2 –102	-7 – 151 m	15 – 158 m	3-193 m	55 – 186 m

The values of relative sea level change calculated for relict channels should only be considered as estimates. Channel age ranges span 10's of thousands of years, over which global sea level typically varies by 100+ m, thus introducing large uncertainty into estimates of post-abandonment crustal uplift. In some cases where high-precision age controls are not available, the range of possible solutions requires at least some post- abandonment uplift (i.e. all three Baja relict channels; Fig. 14). This provides useful information because it allows us to establish a minimum magnitude of uplift over a range of time. Estimates of mean relative sea-level change and vertical motions for relict tidal channels are difficult to interpret for age ranges that span large changes in global sea level. Such estimates can be improved with high-precision dating of channel-filling sediments, which would reduce the uncertainty in estimated of relative sea-level change.

Broader applications of random forest classifiers to geometric classification

This study has demonstrated the effectiveness of random forest classifiers to geometry-based classification of channel planforms. Although we focused on differentiation of tidal and fluvial relict channels, there are potential applications for the geometric classification of channels on extraterrestrial planetary bodies, subsurface channels, relict fluvial channels that form in different climatic regimes, and for fluvial channels that exhibit geometries outside of the single-channel meandering-dominant types documented in this study.

Sinuous channelized planforms have long been recognized on the Moon, Titan, Io, Venus and Mars created by flows of various fluids ranging from lava, water, CO2, and various hydrocarbons (Komatsu, 2007). However, due to the great distance of these planetary bodies and limited data available to planetary geologists and astronomers (other than remotely sensed surficial mapping), study of these channels is largely limited to analysis of channel planform morphology. For planetary bodies that orbit larger bodies or those that are orbited by moons, there is the potential for gravitational tidal forces to act upon the fluids that flow within and form the channels. In such cases, bi-directional flow driven by tidal forces may affect channel planforms similarly to those on Earth, and they may share some of the key geometric characteristics. This hypothesis has not been tested, and consideration must be given to the flow characteristics of the fluids in question, the substrate over which the fluid flows, and the gravity of the specific planetary body. Nonetheless, if planetary channels are assigned a tidal classification using the classification method presented here, it may suggest geometric similarities between extraterrestrial channels and tidal channels on Earth. This could in turn imply the action of bi-directional currents and potentially suggest large oceanic bodies necessary to produce tidal bulges and amphidromic cells.

Geophysical studies have identified paleochannels in the subsurface, with sedimentary cores facilitating in the geological interpretation of these channels (Cockshell, 1980; El-Hussain *et al.*, 2000; Khan & Sinha, 2019). 3D seismic data ana analysis of 1000's of subsurface paleochannels coupled with deep learning has been used to enhance interpretation of seismic data (Wang *et al.*, 2025). 3D seismic data has the benefit of operating in three dimensions to assist in the interpretation of these paleochannels, although the studied channels have not been interpreted in the context of a tidal or fluvial origin. Analysis of a subsurface paleochannel planform using the random forest method (this study) may provide new insights into the origins of subsurface channels that existing methodologies cannot. Changes in depositional environments such as tidal, fluvio-deltaic, or submarine fans can have major impacts on reservoir quality and connectivity for hydrocarbons and water. Characterizing subsurface channel planforms using our methodology may provide researchers additional context with which they can interpret subsurface data.

It may be possible to use random forest classifiers to classify modern and relict fluvial channels characteristic of different climate regimes. By building a comprehensive dataset of modern channel planforms unique to or characteristic of distinct geomorphic conditions such as humid forested areas and grasslands, arid deserts, or thermokarst in the tundra, one could train a random forest classifier to recognize these planforms and classify relict channels to subsequently interpret paleoenvironmental conditions. One example would be the Sahara Desert where abundant relict channel planforms are readily visible in satellite imagery and in radar topography (Ghoneim *et al.*, 2007). The existence of channels in this arid region implies the past action of flowing water that may have been active during African Humid Periods (AHP), the most recent of which extend from 15-5 ka (Pausata *et al.*, 2020). If a random forest classifier trained on modern channels from different climatic conditions could classify these relict channel planforms as having arid-type or humid-type geometry, they could be used to reconstruct past paleoclimatic conditions. Similarly, beaded channels consisting of approximately elliptical pools (beads) connected by straighter segments are well documented in tundra thermokarst (Oswood *et al.*, 1989; Arp *et al.*, 2014; Harlan *et al.*, 2023). Inclusion of these channels in a training dataset for modern channels could enable their recognition in relict channels to reveal evidence for past thermokarst or tundra-like conditions. Such an approach could expand relict channel classification to paleoenvironmental interpretation.

The recent NASA Surface Water and Ocean Topography (SWOT) mission provides an excellent opportunity to employ random forest classifiers and other machine learning techniques to analyze large scale fluvial systems geometrically and hydrologically. The SWOT mission can capture fluvial systems >50-100 m and provide data in vector, raster, water mask pixels that enable measurements of water surface elevation, estimates of discharge, bed shear stress, and even identification of knickpoints (Biancamaria *et al.*, 2016; Stroud *et al.*, 2025). Compiling a dataset of geometric characteristics from the SWOT data products could potentially be used in conjunction with machine learning to identify key geometric changes along the length of a river. Similarly, using convolutional neural networks and SWOT binary water masks may also be used to subdivide and classify fluvial channels with different channel morphologies (i.e. multi-threaded, meandering, anabranching, and braided streams). In coastal regions, especially deltas and lagoons, the data provided by SWOT could facilitate analysis of various geometries and configurations of tidal and deltaic channel networks on a global scale that was not previously feasible.

Conclusions

In this study we applied a random forest classifier trained on a dataset of modern tidal and fluvial channels to 14 relict channels from various physiographic and climatic settings. Using a reach-scale classification threshold validated on modern tidal and fluvial channels, six relict channel reaches were classified as fluvial and eight were classified as tidal. Of the relict reaches assigned a fluvial origin, five were considered to have a high likelihood of a fluvial origin prior to classification based on their geographic locations, geologic history, and present elevation. 80-100% of segments in these five channels were classified as fluvial, indicating that the model is generalizable from the modern to the relict domain. Six relict channel reaches from Baja California Sur, Mexico, and Abdikhani, Iran, were assigned a tidal origin. These channels were considered unknown or potentially tidal prior to classification, and thus a tidal origin is consistent with existing observations of the channels. 98-100% of segments in five of the tidal relict channels were classified as tidal, while the remaining channel had 74% of segments classified as tidal. Two of the relict channels assigned a tidal origin in this study (Pearl River and Stennis relict channels) were previously interpreted as fluvial. However, these two channels formed on regional surfaces that record both marine and fluvial influence, so we considered these to be likely fluvial or potentially tidal.

Analysis of tidal model consensus scores (MCS) for segments in each reach reveals a clear pattern in the distribution that is roughly correlated with the dominant segment-type share for a given channel. Channels with high dominant segment-type shares (85-100%) display distributions with model consensus scores centered around high-consensus scores for the dominant segment-type (~0 = fluvial; ~1 = tidal), indicating strong model consensus on their classification. Channels with moderate to low dominant segment-type shares (<75%) produced MCS distributions with mass centered around moderate-consensus scores (0-0.4; 0.6-1) and greater density of low-consensus scores, or distributions centered around ambiguous, low-consensus scores (0.5). MCS distributions for modern-mixed energy, tidal, and fluvial channels reveal high-consensus distributions in both modern tidal and fluvial channels. Moderate- to low-consensus distributions can be explained by possible factors including: (1) non-unique geometries formed by simultaneous shaping by tidal and fluvial processes in a mixed energy setting; (2) non-unique geometries resulting from natural overlap of tidal and fluvial channel geometries; (3) post-abandonment modification of the channel planform such that the geometry appears neither tidal nor fluvial from the classifier; and (4) non-unique geometries produced by shaping of an active channel by tidal and fluvial process at different stages of a tidal-to-fluvial or fluvial-to-tidal domain shift.

Comparison of relict channels classified as tidal to a Pleistocene sea level curve demonstrates the potential for calculating post-abandonment changes in relative sea level and vertical crustal motions, in areas where the age of channel formation is known. We can use these comparisons to determine the minimum amount of uplift and whether uplift is required at all. In some cases (e.g., the Baja relict channels), the present-day elevation of relict channels requires some amount of post-abandonment uplift, though the existing uncertainty in channel ages introduces large uncertainty in the magnitude of implied uplift. These uncertainties can be reduced with improved, high precision age controls for the relict channels or surfaces on which they formed.

This study demonstrates the efficacy of machine-learning algorithms trained on modern data to classify relict inactive channels preserved on abandoned, low-relief surfaces. Distributions of model consensus scores can be used to assign confidence in reach-scale classification, which is useful for identifying relict tidal channels on uplifted surfaces. For channels with unimodal low-consensus distributions, external field-based evidence for the origin and/or consideration of possible sources of non-unique geometries can be implemented to bolster the analysis. Future work could include direct reach-scale classification using wavelet representation and convolutional neural networks, or analysis of relict channels of known tidal and fluvial origin to better calibrate probability scores. Further additional work might also include testing the reproducibility of results on these channels to examine the effects of digitization being performed by different individuals.

CHAPTER V: DISSERTATION SUMMARY

In this dissertation I presented the results of field surveys of Pliocene sedimentary rocks to test hypotheses for controls on biodiversity on the Baja California peninsula, and of geometric analyses of modern tidal, modern fluvial, and relict channels to develop methods for reconstructing paleo-sea level using relict channels.

In Chapter II I tested the trans-peninsular seaway hypothesis for observed genetic divergence between northern and southern populations of terrestrial plants and animals along the Baja California Peninsula, Mexico. I integrated sedimentary facies analysis, trace fossil assemblages, and stratigraphic and chronological analyses of calcic paleosols within the Pliocene San Regis beds to reconstruct depositional environments, paleoclimatic and ecological conditions, and to estimate the time frame of deposition. The results show that the San Regis beds accumulated over a time span of 397 $\pm$ 116 ky in a sandy braided fluvial system during which calcic paleosol development and trace fossil assemblages indicate a predominantly arid climate that transitioned to semi-arid climate during the later phases of deposition. These results unequivocally refute the trans-peninsular seaway hypothesis, leaving changes in seasonal rainfall and habitat quality/quantity as the principal drivers of biodiversity on the peninsula.

In Chapter III, after recognizing relict channels associated with marine terraces in central Baja California Peninsula, Mexico, for which no method existed for determining their origin based on their geometry, I performed a machine-learning based analysis of the planform geometries of modern tidal and fluvial channels, to develop a system for effectively classifying modern reaches according to their true channel type, to be later applied to relict channels. The results of this analysis revealed that simple classification methods such as linear discriminant analysis are not suitable for distinguishing tidal and fluvial channels. Through testing three machine-learning algorithms over 69 trials that included combinations of variables describing the channel geometries, I determined that a random forest classifier acting at the segment-scale using variables derived from normalized width and normalized radius of curvature can be used to successfully classify modern channels at the reach-scale using dominant segment-type thresholds. The analysis also determined that the most important geometric characteristics for differentiating between tidal and fluvial channels is the relationship between local channel width and the local radius of curvature, where fluvial channels exhibit a more complex relationship between the two metrics than tidal channels.

In Chapter IV, having developed a robust methodology for classifying modern tidal and fluvial channels in Chapter III, I return to the domain of relict channels and their potential for use as paleo-sea level indicators. I applied the classification methods of chapter III to a dataset of uplifted, abandoned relict channels in central Baja California and localities around the world that cover various climatic regimes. The dataset included channels that were of likely fluvial origin and those of unknown/potentially tidal origin to test the efficacy of the classification method. Channels of likely fluvial origin were correctly classified as fluvial, whereas channels of unknown/potentially tidal origin were all assigned a tidal classification with varying levels of confidence. Analysis of model consensus scores for both modern tidal, fluvial, and mixed-energy channels as well as relict channels showed that non-unique geometries arising from natural geometric overlap, simultaneous shaping by tidal and fluvial processes, post-abandonment modification of planform geometries, and asynchronous shaping by tidal and fluvial processes during domain shifts created by changes in relative sea level, can cause lower dominant-segment type shares during the channel classification process that can affect the robustness of these classifications. Comparison of the elevations of relict tidal channels to known global sea level curves demonstrate the potential efficacy of relict tidal channels to act as paleo-sea level indicators, in turn providing constraints for relative sea level change in these regions.

The three chapters presented in this dissertation demonstrate the scientific potential for using techniques that combine understanding of ancient and modern surface processes, soil development, and trace fossil assemblages to provide useful constraints on reconstructing paleo-depositional environments, paleoclimate, and ancient and recent changes in relative sea level. The results presented here resolve long-standing questions over the controls on biodiversity on the Baja California Peninsula, provide a test case for using calcic soil horizons to estimate duration and rate of sedimentation, identify key geometric variables that differentiate tidal and fluvial channels, and demonstrate the efficacy of using relict tidal channels to constrain changes in relative sea level in coastal regions. Future work could include additional field surveys to quantify the paleotopography between Miocene and Pliocene deposits in the central Baja California Peninsula to understand landscape changes in a low-accommodation environment undergoing changes in relative sea level, or using wavelet representations of tidal and fluvial channels with convolutional neural networks to permit direct classification of modern and relict channels at the reach-scale while preserving sub- and supra-meander architectures. In the future, similar analyses may also be performed on extraterrestrial bodies to better understand their surface evolution and reconstruct their histories similarly to how we have done here on Earth.

REFERENCES CITED

Alam, J., **Mandal, D.K.**, **Barman, S.** and **Singha, P.** (2025) Late Holocene rapid terrestrialization of abandoned channels and vulnerability in the Himalayan Foreland basin area in India. *J. Clean. Prod.*, **518**, 145821.

Allen, J.R.L. (1982) Sedimentary structures, their character and physical basis (Vol. 2). *Developments in Sedimentology 30B*, **2**, 645.

Alonso-Zarza, A.M. and **Silva, P.G.** (2002) Quaternary laminar calcretes with bee nests: evidences of small-scale climatic fluctuations, Eastern Canary Islands, Spain. *Palaeogeogr. Palaeoclimatol. Palaeoecol.*, **178**, 119–135.

Araya-Donoso, R., **Biddy, A.**, **Munguía-Vega, A.**, **Lira-Noriega, A.** and **Dolby, G.A.** (2024) Habitat quality or quantity? Niche marginality across 21 plants and animals suggests differential responses between highland and lowland species to past climatic changes. *Ecography*, **2024**, e07391.

Araya-Donoso, R., **San Juan, E.**, **Tamburrino, Í.**, **Lamborot, M.**, **Veloso, C.** and **Véliz, D.** (2022) Integrating genetics, physiology and morphology to study desert adaptation in a lizard species. *Journal of Animal Ecology*, **91**, 1148–1162.

Arp, C.D., **Whitman, M.S.**, **Jones, B.M.**, **Grosse, G.**, **Gaglioti, B. V.** and **Heim, K.C.** (2014) Beaded streams of Arctic permafrost landscapes. doi: 10.5194/bgd-11-11391-2014

Avellán, D.R., **Macías, J.L.**, **Arce, J.L.**, **Saucedo-Girón, R.**, **Garduño-Monroy, V.H.**, **Jiménez-Haro, A.**, **Sosa-Ceballos, G.**, **Cisneros, G.**, **Bernal, J.P.**, **Layer, P.W.**, **García-Sánchez, L.**, **Reyes-Agustín, G.**, **Rangel, E.**, **Navarrete, J.A.** and **López-Loera, H.** (2019) Geology of the late Pleistocene Tres Vírgenes Volcanic Complex, Baja California Sur (México). *J. Maps*, **15**, 227–237.

Barbour, E.H. (1897) Nature, Structure, and Phylogeny of Daemonelix. *Bulletin of the Geological Society of America*, **8**, 305–314.

Bennett, S.E.K., **Darin, M.H.**, **Dorsey, R.J.**, **Hausback, B.**, **Grandy, S.**, **Heizler, M.T.**, **Stelten, M.E.**, **Pecha, M.E.**, **Schmitt, A.** and **Dolby, G.A.** (2025) Neogene volcano-tectonic evolution of the central Baja California peninsula, México: transition from subduction to rifting and marine incursion. In: *Geological Society of America Abstracts with Programs Vol. 57, No. 4, Abstract 16-1*,

Bennett, S.E.K. and **Oskin, M.E.** (2014) Oblique rifting ruptures continents: Example from the Gulf of California shear zone. *Geology*, **42**, 215–218.

Bennett, S.E.K., **Oskin, M.E.**, **Dorsey, R.J.**, **Iriondo, A.** and **Kunk, M.J.** (2015) Stratigraphy and structural development of the southwest Isla Tiburón marine basin: Implications for latest Miocene tectonic opening and flooding of the northern Gulf of California. *Geosphere*, **11**, 977–1007.

Benoit, M., **Aguillón-Robles, A.**, **Calmus, T.**, **Maury, R.C.**, **Bellon, H.**, **Cotten, J.**, **Bourgois, J.** and **Michaud, F.** (2002) Geochemical Diversity of Late Miocene Volcanism in Southern Baja California, Mexico: Implication of Mantle and Crustal Sources during the Opening of an Asthenospheric Window. *J. Geol.*, **110**, 627–648.

Berberian, M. (1995) Master "blind" thrust faults hidden under the Zagros folds: active basement tectonics and surface morphotectonics. *Tectonophysics*, **241**, 193–224.

Bhattacharya, J.P. (1992) Deltas. In: *In: Facies Models (Ed. byR. G. Walker &N. P. James), pp. 157^ 177. Geological Association of*, *Citeseer*,

Bhattacharya, T., **Tierney, J.E.**, **Addison, J.A.** and **Murray, J.W.** (2018) Ice-sheet modulation of deglacial North American monsoon intensification. *Nature Geoscience 2018 11:11*, **11**, 848–852.

Biancamaria, S., **Lettenmaier, D.P.** and **Pavelsky, T.M.** (2016) The SWOT Mission and Its Capabilities for Land Hydrology. 117–147.

Bintanja, R., **Van De Wal, R.S.W.** and **Oerlemans, J.** (2005) Modelled atmospheric temperatures and global sea levels over the past million years. *Nature 2005 437:7055*, **437**, 125–128.

Birkeland, P.W. (1999) Soils and geomorphology. *Oxford University Press*, Oxford, 488 pp.

Blum, M.D. and **Roberts, H.H.** (2009) Drowning of the Mississippi Delta due to insufficient sediment supply and global sea-level rise. *Nature Geoscience 2009 2:7*, **2**, 488–491.

Bown, T.M., **Hasiotis, S.T.**, **Genise, J.F.** and **Maldonado, F.** (1997) Trace Fossils of Hymenoptera and Other Insects. *US Geological Survey Bulletin*, **2153**, 41.

Brady, N.C. and **Weil, R.R.** (2002) The Nature and Properties of Soils.(13th eds.).

Brandes, C., **Steffen, H.**, **Steffen, R.**, **Li, T.** and **Wu, P.** (2025) Effects of the Last Quaternary Glacial Forebulge on Vertical Land Movement, Sea-Level Change, and Lithospheric Stresses. Reviews of Geophysics. doi: 10.1029/2024RG000852

Breiman, L. (2001) Random forests. *Mach. Learn.*, **45**, 5–32.

Breiman, L., **Friedman, J.H.**, **Olshen, R.A.** and **Stone, C.J.** (1984) Classification And Regression Trees, 1st edn. *Routledge*, New York, 368 pp.

Bressan, T.S., **Kehl de Souza, M.**, **Girelli, T.J.** and **Junior, F.C.** (2020) Evaluation of machine learning methods for lithology classification using geophysical data. *Comput. Geosci.*, **139**, 104475.

Bromley, R.G. (1996) Trace fossils: Biology, Taphonomy, and Applications. *Chapman and Hall*, London, 361 pp.

Calmus, T., **Aguillón-Robles, A.**, **Maury, R.C.**, **Bellon, H.**, **Benoit, M.**, **Cotten, J.**, **Bourgois, J.** and **Michaud, F.** (2003) Spatial and temporal evolution of basalts and magnesian andesites ("bajaites") from Baja California, Mexico: the role of slab melts. *Lithos*, **66**, 77–105.

Cardonatto, M.C. and **Melchor, R.N.** (2018) Large mammal burrows in late Miocene calcic paleosols from central Argentina: Paleoenvironment, taphonomy and producers. *PeerJ*, **2018**, e4787.

Cardonatto, M.C., **Sostillo, R.**, **Visconti, G.** and **Melchor, R.N.** (2016) The Celliforma ichnofacies in calcareous paleosols: An example from the late Miocene Cerro Azul Formation, La Pampa, Argentina. *Palaeogeogr. Palaeoclimatol. Palaeoecol.*, **443**, 203–215.

Carreño, A.L. and **Smith, J.T.** (2007) Stratigraphy and correlation for the ancient Gulf of California and Baja California Peninsula, Mexico. *Paleontological Research Institution*.

Cartigny, M.J.B., **Ventra, D.**, **Postma, G.** and **van Den Berg, J.H.** (2014) Morphodynamics and sedimentary structures of bedforms under supercritical-flow conditions: New insights from flume experiments. *Sedimentology*, **61**, 712–748.

Cockshell, C.D. (1980) Exploration for Underground Gas Storage Targets in South Australia. *Exploration Geophysics*, **11**, 63–68.

Corbi, F., **Sandri, L.**, **Bedford, J.**, **Funiciello, F.**, **Brizzi, S.**, **Rosenau, M.** and **Lallemand, S.** (2019) Machine Learning Can Predict the Timing and Size of Analog Earthquakes. *Geophys. Res. Lett.*, **46**, 1303–1311.

Counts, J.W. and **Hasiotis, S.T.** (2014) Distribution, Paleoenvironmental Implications, and Stratigraphic Architecture of Paleosols In Lower Permian Continental Deposits of Western Kansas, U.S.A. *Journal of Sedimentary Research*, **84**, 144–167.

Covault, J.A., **Kostic, S.**, **Paull, C.K.**, **Sylvester, Z.** and **Fildani, A.** (2017) Cyclic steps and related supercritical bedforms: Building blocks of deep-water depositional systems, western North America. *Mar. Geol.*, **393**, 4–20.

Coyne, J.A. and **Orr, H.A.** (2004) Speciation Sinauer Associates. *Sunderland, MA*, **276**, 854.

Cracknell, M.J. and **Reading, A.M.** (2014) Geological mapping using remote sensing data: A comparison of five machine learning algorithms, their response to variations in the spatial distribution of training data and the use of explicit spatial information. *Comput. Geosci.*, **63**, 22–33.

Crews, S.C. and **Hedin, M.** (2006) Studies of morphological and molecular phylogenetic divergence in spiders (Araneae: Homalonychus) from the American southwest, including divergence along the Baja California Peninsula. *Mol. Phylogenet. Evol.*, **38**, 470–487.

Dalrymple, R.W., **Kurcinka, C.E.**, **Jablonski, B.V.J.**, **Ichaso, A.A.** and **Mackay, D.A.** (2015) Deciphering the relative importance of fluvial and tidal processes in the fluvial–marine transition. *Developments in Sedimentology*, **68**, 3–45.

Darin, M.H., **Bennett, S.E.K.**, **Dorsey, R.J.**, **Oskin, M.E.** and **Iriondo, A.** (2016) Late Miocene extension in coastal Sonora, México: Implications for the evolution of dextral shear in the proto-Gulf of California oblique rift. *Tectonophysics*, **693**, 378–408.

Darin, M.H., **Dorsey, R.J.**, **Niemi, T.M.**, **Salgado Muñoz, V.O.**, **Henry, M.W.** and **Pecha, M.E.** (2025) Depositional age of the Boleo Formation and marine flooding in the central Gulf of California Rift, Santa Rosalía basin, Baja California Sur, México. Special Paper of the Geological Society of America. doi: 10.1130/2025.2563(13)

Das, P. and **Pandey, V.** (2019) Use of logistic regression in land-cover classification with moderate-resolution multispectral data. *Journal of the Indian Society of Remote Sensing*, **47**, 1443–1454.

de Boer, B., **Stocchi, P.**, **Whitehouse, P.L.** and **van de Wal, R.S.W.** (2017) Current state and future perspectives on coupled ice-sheet – sea-level modelling. *Quat. Sci. Rev.*, **169**, 13–28.

Dépret, T., **Riquier, J.** and **Piégay, H.** (2017) Evolution of abandoned channels: Insights on controlling factors in a multi-pressure river system. *Geomorphology*, **294**, 99–118.

Dibog, L., **Eggleton, P.** and **Forzi, F.** (1998) Seasonality of soil termites in a humid tropical forest, Mbalmayo, southern Cameroon. *J. Trop. Ecol.*, **14**, 841–850.

Dieras, P.L. (2013) The persistence of oxbow lakes as aquatic habitats: An assessment of rates of change and patterns of alluviation. Cardiff University

Dietrich, P., **Ghienne, J.-F.**, **Normandeau, A.** and **Lajeunesse, P.** (2016) Upslope-Migrating Bedforms In A Proglacial Sandur Delta: Cyclic Steps From River-Derived Underflows? *Journal of Sedimentary Research*, **86**, 113–123.

Dolby, G.A., **Bennett, S.E.K.**, **Dorsey, R.J.**, **Stokes, M.F.**, **Riddle, B.R.**, **Lira-Noriega, A.**, **Munguia-Vega, A.** and **Wilder, B.T.** (2022) Integrating Earth–life systems: a geogenomic approach. *Trends Ecol. Evol.*, **37**, 371–384.

Dolby, G.A., **Bennett, S.E.K.**, **Lira-Noriega, A.**, **Wilder, B.T.** and **Munguía-Vega, A.** (2015) Assessing the Geological and Climatic Forcing of Biodiversity and Evolution Surrounding the Gulf of California. *J. Southwest*, **57**, 391–455.

Dolby, G.A., **Ellingson, R.A.**, **Findley, L.T.** and **Jacobs, D.K.** (2018) How sea level change mediates genetic divergence in coastal species across regions with varying tectonic and sediment processes. *Mol. Ecol.*, **27**, 994–1011.

Dolby, G.A., **Hechinger, R.**, **Ellingson, R.A.**, **Findley, L.T.**, **Lorda, J.** and **Jacobs, D.K.** (2016) Sea-level driven glacial-age refugia and post-glacial mixing on subtropical coasts, a palaeohabitat and genetic study. Proceedings of the Royal Society B: Biological Sciences. doi: 10.1098/RSPB.2016.1571

Doody, J.S., **James, H.**, **Colyvas, K.**, **Mchenry, C.R.** and **Clulow, S.** (2015) Deep nesting in a lizard, déjà vu devil's corkscrews: first helical reptile burrow and deepest vertebrate nest. *Biological Journal of the Linnean Society*, **116**, 13–26.

Doody, J.S., **Shukla, S.** and **Hasiotis, S.T.** (2024) Why animals construct helical burrows: Construction vs. post-construction benefits. *Ecol. Evol.*, **14**, e11181.

Dorsey, R.J., **Darin, M.H.**, **Bennett, S.E.K.**, **Hausback, B.P.**, **Gardner, K.K.**, **Niemi, T.M.**, **Busby, C.**, **Graettinger, A.**, **Salgado Muñoz, V.O.**, **Martinez Gutierrez, G.**, **Morebeck, C.**, **Usher, E.**, **Heizler, M.T.**, **Pecha, M.E.**, **Stelten, M.**, **Schmitt, A.** and **Dolby, G.A.** (2024) Miocene tectonic and stratigraphic evolution of the central Baja California peninsula and rapid marine flooding into the Gulf of California at ca. 6.3 Ma (Invited). In: *Geological Society of America Abstracts with Programs. Vol. 56, No. 5, Abstract 72-13.* ,

Eggleton, P. (2000) Global Patterns of Termite Diversity. In: *Termites: Evolution, Sociality, Symbioses, Ecology* (Ed. T. Abe, D.E. Bignell, and M. Higashi), *Springer Netherlands*, Dordrecht, 25–51.

El Fels, A.E.A. and **El Ghorfi, M.** (2022) Using remote sensing data for geological mapping in semi-arid environment: a machine learning approach. *Earth Sci. Inform.*, **15**, 485–496.

Elderfield, H., **Ferretti, P.**, **Greaves, M.**, **Crowhurst, S.**, **McCave, I.N.**, **Hodell, D.** and **Piotrowski, A.M.** (2012) Evolution of Ocean Temperature and Ice Volume Through the Mid-Pleistocene Climate Transition. *Science (1979).*, **337**, 704–709.

El-Hussain, I., **Holbrook, J.** and **Sneed, C.** (2000) Integrating Geophysical And Geological Methods To Delineate Buried Paleochannels In The New Madrid Seismic Zone Of Southeastern Missouri. In: *13th EEGS Symposium on the Application of Geophysics to Engineering and Environmental Problems*, *European Association of Geoscientists & Engineers*,

Erickson, R.L. and **Marsh, S.P.** (1974) Geologic map of the Iron Point quadrangle, Humboldt County, Nevada.

Evans, D.L., **Farr, T.G.**, **Ford, J.P.**, **Thompson, T.W.** and **Werner, C.L.** (1986) Multipolarization Radar Images for Geologic Mapping and Vegetation Discrimination. *IEEE Transactions on Geoscience and Remote Sensing*, **GE-24**, 246–257.

Fagherazzi, S., **Gabet, E.J.** and **Furbish, D.J.** (2004) The effect of bidirectional flow on tidal channel planforms. *Earth Surf. Process. Landf.*, **29**, 295–309.

Feng, R. (2021) Improving uncertainty analysis in well log classification by machine learning with a scaling algorithm. *J. Pet. Sci. Eng.*, **196**, 107995.

Fielding, C.R., **Alexander, J.** and **Allen, J.P.** (2018) The role of discharge variability in the formation and preservation of alluvial sediment bodies. *Sediment. Geol.*, **365**, 1–20.

Finotello, A., **D'Alpaos, A.**, **Bogoni, M.**, **Ghinassi, M.** and **Lanzoni, S.** (2020) Remotely-sensed planform morphologies reveal fluvial and tidal nature of meandering channels. *Scientific Reports 2020 10:1*, **10**, 1–13.

Finotello, A., **Ielpi, A.**, **Lapôtre, M.G.A.**, **Lazarus, E.D.**, **Ghinassi, M.**, **Carniello, L.**, **Favaro, S.**, **Tognin, D.** and **D'Alpaos, A.** (2024) Vegetation enhances curvature-driven dynamics in meandering rivers. *Nat. Commun.*, **15**, 1968.

Finotello, A., **Lanzoni, S.**, **Ghinassi, M.**, **Marani, M.**, **Rinaldo, A.** and **D'Alpaos, A.** (2018) Field migration rates of tidal meanders recapitulate fluvial morphodynamics. *Proceedings of the National Academy of Sciences*, **115**, 1463–1468.

Fischer, S.A. and **Hasiotis, S.T.** (2018) Stratigraphic changes in ichnopedofacies of the Upper Triassic Chinle Formation, Utah: implications to paleohydrology and paleoclimate. In: *Annales. Societatis Geologorum Poloniae*, 88, 127–162.

Fox, G.A. and **Wilson, G. V.** (2010) The Role of Subsurface Flow in Hillslope and Stream Bank Erosion: A Review. *Soil Science Society of America Journal*, **74**, 717–733.

Gao, C., **Lazarus, E.D.**, **D'Alpaos, A.**, **Ghinassi, M.**, **Ielpi, A.**, **Parker, G.**, **Rinaldo, A.**, **Gao, P.**, **Wang, Y.P.**, **Tognin, D.** and **Finotello, A.** (2024) Morphometry of Tidal Meander Cutoffs Indicates Similarity to Fluvial Morphodynamics. *Geophys. Res. Lett.*, **51**, e2023GL105893.

García Sánchez, L., **Macías, J.L.**, **Sulpizio, R.**, **Osorio-Ocampo, L.S.**, **Pellicioli, C.**, **Pola, A.**, **Avellan, D.R.**, **Cisneros, G.**, **García, F.**, **Ocampo-Díaz, Y.Z.E.**, **Lira-Beltran, R.M.**, **Saucedo, R.**, **Sánchez-Núñez, J.M.**, **Arce, J.L.**, **Corona-Chávez, P.**, **Reyes-Agustin, G.**, **Cardona, M.**, **Layer, P.W.**, **Benowitz, J.**, **Solari, L.** and **Groppelli, G.** (2019) Geology of La Reforma caldera complex, Baja California, Mexico. *J. Maps*, **15**, 487–498.

Gardner, K. and **Dorsey, R.J.** (2021) Mixed carbonate–siliciclastic sedimentation at the margin of a late Miocene tidal strait, lower Colorado River Valley, south-western USA. *Sedimentology*, sed.12834.

Gardner, K.K. and **Dorsey, R.J.** (2025) Planform geometric classification of fluvial and tidal channels via machine learning. Earth Surf Process Landf. doi: 10.1002/ESP.70010

Genise, J.F. (2000) The ichnofamily Celliformidae for Celliforma and allied ichnogenera. *Ichnos: An International Journal of Plant & Animal*, **7**, 267–282.

Genise, J.F. (2017) Paleosol Ichnofacies. *Springer, Cham*, 559–577.

Genise, J.F. and **Edwards, N.** (2003) Ichnotaxonomy, Origin, and Paleoenvironment of Quaternary Insect Cells from Fuerteventura, Canary Islands, Spain. *Source: Journal of the Kansas Entomological Society*, **76**, 320–327.

Genise, J.F., **Melchor, R.N.**, **Bellosi, E.S.** and **Verde, M.** (2010) Invertebrate and Vertebrate Trace Fossils from Continental Carbonates. In: *Developments in Sedimentology, Carbonates in Continental Settings* (Ed. A.J. Van Loon, A.M. Alonso-Zarza, and L.H. Tanner), *Elsevier*, 61, 319–369.

Geological Survey of India (1999) Geological & Mineral Map of West Bengal.

Ghoneim, E., **Robinson, C.** and **El-Baz, F.** (2007) Radar topography data reveal drainage relics in the eastern Sahara. *Int. J. Remote Sens.*, **28**, 1759–1772.

Ghorbani, M. (2013) A Summary of Geology of Iran. *Springer Geology*, 45–64.

Golly, A. and **Turowski, J.M.** (2017) Deriving principal channel metrics from bank and long-profile geometry with the R package cmgo. *Earth Surface Dynamics*, **5**, 557–570.

Goodbred, S.L. and **Kuehl, S.A.** (2000) The significance of large sediment supply, active tectonism, and eustasy on margin sequence development: Late Quaternary stratigraphy and evolution of the Ganges–Brahmaputra delta. *Sediment. Geol.*, **133**, 227–248.

Graham, M.R., **Bryson, R.W.** and **Riddle, B.R.** (2014) Late Pleistocene to Holocene distributional stasis in scorpions along the Baja California peninsula. *Biological Journal of the Linnean Society*, **111**, 450–461.

Greb, S.F. and **Martino, R.L.** (2009) Fluvial–estuarine transitions in fluvial-dominated successions: examples from the Lower Pennsylvanian of the Central Appalachian Basin. *Fluvial Sedimentology VII*, 425–451.

Gugliotta, M., **Saito, Y.**, **Ta, T.K.O.**, **Nguyen, V.L.**, **Tamura, T.**, **Wang, Z.**, **La Croix, A.D.** and **Nakashima, R.** (2021) Abandonment and rapid infilling of a tide-dominated distributary channel at 0.7 ka in the Mekong River Delta. *Scientific Reports 2021 11:1*, **11**, 11040-.

Hanneman, D.L., **Lofgren, D.**, **Hasiotis, S.T.** and **McIntosh, W.C.** (2022) Priabonian, late Eocene chronostratigraphy, depositional environment, and paleosol-trace fossil associations, Pipestone Springs, southwest Montana, USA. *Acta Palaeontol. Pol.*, **67**, 5–20.

Harlan, M.E., **Gleason, C.J.**, **Flores, J.A.**, **Langhorst, T.M.** and **Roy, S.** (2023) Mapping and characterizing Arctic beaded streams through high resolution satellite imagery. *Remote Sens. Environ.*, **285**, 113378.

Hasiotis, S.T. (2002) Continental trace fossils: sEPM short course notes, no. 51.

Hasiotis, S.T. (2004) Reconnaissance of Upper Jurassic Morrison Formation ichnofossils, Rocky Mountain Region, USA: paleoenvironmental, stratigraphic, and paleoclimatic significance of terrestrial and freshwater ichnocoenoses. *Sediment. Geol.*, **167**, 177–268.

Hasiotis, S.T. (2003) Complex ichnofossils of solitary and social soil organisms: understanding their evolution and roles in terrestrial paleoecosystems. *Palaeogeogr. Palaeoclimatol. Palaeoecol.*, **192**, 259–320.

Hasiotis, S.T. and **Dubiel, R.F.** (1995) Termite (Insecta: Isoptera) nest ichnofossils from the upper triassic chinle formation, petrified forest national park, Arizona. *Ichnos: An International Journal of Plant & Animal*, **4**, 119–130.

Hasiotis, S.T., **Kraus, M.J.** and **Demko, T.M.** (2007) Climatic Controls on Continental Trace Fossils. *Trace Fossils: Concepts, Problems, Prospects*, 172–195.

Hasiotis, S.T. and **Mitchell, C.E.** (1993) A comparison of crayfish burrow morphologies: Triassic and Holocene fossil, paleo- and neo-ichnological evidence, and the identification of their burrowing signatures. *Ichnos: An International Journal of Plant & Animal*, **2**, 291–314.

Hasiotis, S.T., **Parrish, J.T.** and **Chan, M.A.** (2025) Paleoecology of the Lower Jurassic Navajo Sandstone (colorado Plateau, Usa). *Palaios*, **40**, 141–170.

Hasiotis, S.T. and **Platt, B.F.** (2012) Exploring the sedimentary, pedogenic, and hydrologic factors that control the occurrence and role of bioturbation in soil formation and horizonation in continental deposits: an integrative approach. *The Sedimentary Record*, **10**, 4–9.

Hasiotis, S.T., **Wellner, R.W.**, **Martin, A.J.** and **Demko, T.M.** (2004) Vertebrate Burrows from Triassic and Jurassic Continental Deposits of North America and Antarctica: Their Paleoenvironmental and Paleoecological Significance. *Ichnos*, **11**, 103–124.

Hausback, B.P. (1984) Cenozoic Volcanic and Tectonic Evolution of Baja California Sur, Mexico. In: *Geology of the Baja California Peninsula* (Ed. V. Frizzel), *Pacific Section SEPM*, 219–236.

Heinrich, P. V (2006) Pleistocene and Holocene fluvial systems of the lower Pearl River, Mississippi and Louisiana, USA. *Gulf Coast Association of Geological Societies Transactions*, **56**, 267–278.

Hembree, D.I. and **Hasiotis, S.T.** (2008) Miocene vertebrate and invertebrate burrows defining compound paleosols in the Pawnee Creek Formation, Colorado, U.S.A. *Palaeogeogr. Palaeoclimatol. Palaeoecol.*, **270**, 349–365.

Hinton, G.E. (1990) Connectionist Learning Procedures. In: *Machine Learning* (Ed. Y. Kodratoff and R.S. Michalski), *Elsevier*, 555–610.

Hotz, P.E. and **Willden, R.** (1961) Preliminary geologic map and sections of the Osgood Mountains quadrangle, Humboldt County, Nevada.

Huang, H.Q. and **Nanson, G.C.** (1998) The influence of bank strength on channel geometry: an integrated analysis of some observations. *Earth Surf. Process. Landf.*, **23**, 865–876.

Hughes, Z.J. (2012) Principles of Tidal Sedimentology. *Springer Netherlands*, Dordrecht, 35–55 pp.

Ibrahim, A.A. (2002) Activity area, movement patterns, and habitat use of the desert monitor, varanus griseus, in the zaranik protected area, north Sinai, Egypt. *African Journal of Herpetology*, **51**, 35–45.

Johnston, P.A., **Eberth, D.A.** and **Anderson, P.K.** (1996) Alleged vertebrate eggs from Upper Cretaceous redbeds, Gobi Desert, are fossil insect (Coleoptera) pupal chambers: Fictovichnus new ichnogenus. *Can. J. Earth Sci.*, **33**, 511–525.

Keshtkar, H., **Voigt, W.** and **Alizadeh, E.** (2017) Land-cover classification and analysis of change using machine-learning classifiers and multi-temporal remote sensing imagery. *Arabian Journal of Geosciences*, **10**, 1–15.

Khan, I. and **Sinha, R.** (2019) Discovering 'buried' channels of the Palaeo-Yamuna river in NW India using geophysical evidence: Implications for major drainage reorganization and linkage to the Harappan Civilization. *J. Appl. Geophy.*, **167**, 128–139.

Kingma, D.P. and **Ba, J.** (2014) Adam: A method for stochastic optimization.

Klappa, C.F. (1980) Rhizoliths in terrestrial carbonates: classification, recognition, genesis and significance. *Sedimentology*, **27**, 613–629.

Knox, J.C. (1985) Responses of Floods to Holocene Climatic Change in the Upper Mississippi Valley. *Quat. Res.*, **23**, 287–300.

Komatsu, G. (2007) Rivers in the Solar System: Water Is Not the Only Fluid Flow on Planetary Bodies. *Geogr. Compass*, **1**, 480–502.

Kong, J.A., **Swartz, A.A.**, **Yueh, H.A.**, **Novak, L.M.** and **Shin, R.T.** (1988) Identification of terrain cover using the optimum polarimetric classifier. *J. Electromagn. Waves Appl.*, **2**, 171–194.

Kraus, M.J. and **Aslan, A.** (2009) Palaeosol Sequences in Floodplain Environments: A Hierarchical Approach. *Palaeoweathering, Palaeosurf aces and Related Continental Deposits*, 303–321.

Krummeck, W.D. and **Bordy, E.M.** (2018) Reniformichnus katikatii (New Ichnogenus and Ichnospecies): Continental Vertebrate Burrows from the Lower Triassic, Main Karoo Basin, South Africa. *Ichnos*, **25**, 138–149.

Kuehl, S.A., **Allison, M.A.**, **Goodbred, S.L.** and **Kudrass, H.** (2011) The Ganges–Brahmaputra Delta. In: *River Deltas-Concepts, Models, and Examples*, *SEPM (Society for Sedimentary Geology)*, 413–434.

Kuiper, K.F., **Deino, A.**, **Hilgen, F.J.**, **Krijgsman, W.**, **Renne, P.R.** and **Wijbrans, and J.R.** (2008) Synchronizing rock clocks of Earth history. *Science (1979).*, **320**, 500–504.

Kurtze, D.A. (2022) Gravitational effects of ice sheets on sea level. *Am. J. Phys.*, **90**, 351–358.

Kvale, E.P., **Cutright, J.**, **BIlodeau, D.**, **Archer, A.**, **Johnson, H.R.** and **Pickett, B.** (1995) Analysis of modern tides and implications for ancient tidalites. Cont Shelf Res. doi: 10.1016/0278-4343(95)00001-H

Lang, J., **Sievers, J.**, **Loewer, M.**, **Igel, J.** and **Winsemann, J.** (2017) 3D architecture of cyclic-step and antidune deposits in glacigenic subaqueous fan and delta settings: Integrating outcrop and ground-penetrating radar data. *Sediment. Geol.*, **362**, 83–100.

Lanzoni, S. and **D'Alpaos, A.** (2015) On funneling of tidal channels. *J. Geophys. Res. Earth Surf.*, **120**, 433–452.

Lanzoni, S. and **Seminara, G.** (1998) On tide propagation in convergent estuaries. *J. Geophys. Res. Oceans*, **103**, 30793–30812.

Laza, J.H. (2006) Dung-Beetle Fossil Brood Balls: The Ichnogenera Coprinisphaera Sauer and Quirogaichnus (Coprinisphaeridae). *Ichnos*, **13**, 217–235.

Le Bars, D., **De Vries, H.** and **Drijfhout, S.** (2019) Sea level rise and its spatial variations: Technical report 372. *KNMI technical report, 372*.

Lee, J.S., **Grunes, M.R.** and **Kwok, R.** (1994) Classification of multi-look polarimetric SAR imagery based on complex Wishart distribution. *Int. J. Remote Sens.*, **15**, 2299–2311.

Leopold, L.B. and **Wolman, M.G.** (1957) River channel patterns: braided, meandering, and straight. *US Government Printing Office*, Washington, D.C., 39–85 pp.

Leopold, L.B., **Wolman, M.G.** and **Miller, J.P.** (1964) Fluvial processes in geomorphology. *Dover Publications, Inc.*, New York, NY.

Lindell, J., **Ngo, A.** and **Murphy, R.W.** (2006) Deep genealogies and the mid-peninsular seaway of Baja California. *J. Biogeogr.*, **33**, 1327–1331.

Lisiecki, L.E. and **Raymo, M.E.** (2005) A Pliocene-Pleistocene stack of 57 globally distributed benthic δ^{18}O records. Paleoceanography. doi: 10.1029/2004PA001071

Longhitano, S.G. (2013) A facies-based depositional model for ancient and modern, tectonically-confined tidal straits. *Terra Nova*, **25**, 446–452.

Lopes, R.P., **Frank, H.T.**, **Buchmann, F.S. de C.** and **Caron, F.** (2017) Megaichnus igen. nov.: Giant Paleoburrows Attributed to Extinct Cenozoic Mammals from South America. *Ichnos*, **24**, 133–145.

Lutscher, F., **McCauley, E.** and **Lewis, M.A.** (2007) Spatial patterns and coexistence mechanisms in systems with unidirectional flow. *Theor. Popul. Biol.*, **71**, 267–277.

Marani, M., **Lanzoni, S.**, **Zandolin, D.**, **Seminara, G.** and **Rinaldo, A.** (2002) Tidal meanders. *Water Resour. Res.*, **38**, 7–14.

Martin, L.D. and **Bennett, D.K.** (1977) The burrows of the miocene beaver palaeocastor, Western Nebraska, U.S.A. *Palaeogeogr. Palaeoclimatol. Palaeoecol.*, **22**, 173–193.

McCullagh, P. (2019) Generalized linear models. *Routledge.*

McFall, C.C. (1968) Reconnaissance geology of the concepcion bay area, Baja California, Mexico.

McLean, H., **Hausback, B.P.**, **Knapp, J.H.** and **Survey, U.S.G.** (1985) Reconnaissance geologic map of part of the San Isidro Quadrangle, Baja California Sur, Mexico. Reston, VA.

McPherson, J.G., **Shanmugam, G.** and **Moiola, R.J.** (1987) Fan-deltas and braid deltas: Varieties of coarse-grained deltas. *Geol. Soc. Am. Bull.*, **99**, 331.

Menant, A., **Angiboust, S.**, **Gerya, T.**, **Lacassin, R.**, **Simoes, M.** and **Grandin, R.** (2020) Transient stripping of subducting slabs controls periodic forearc uplift. *Nat. Commun.*, **11**, 1823.

Miall, A.D. (2022) Facies Analysis. In: *Stratigraphy: A Modern Synthesis* (Ed. A.D. Miall), *Springer International Publishing*, Cham, 91–174.

Min, K., **Mundil, R.**, **Renne, P.R.** and **Ludwig, K.R.** (2000) A test for systematic errors in 40Ar/39Ar geochronology through comparison with U/Pb analysis of a 1.1-Ga rhyolite. *Geochim. Cosmochim. Acta*, **64**, 73–98.

Monger, H.C., **Gile, L.H.**, **Hawley, J.W.** and **Grossman, R.B.** (1972) The desert project - An analysis of aridland soil-geomorphic processes. *Bulletin 798* **•**, **New Mexico**, 1–66.

Morag, N., **Haviv, I.**, **Eyal, M.**, **Kohn, B.P.** and **Feinstein, S.** (2019) Early flank uplift along the Suez Rift: Implications for the role of mantle plumes and the onset of the Dead Sea Transform. *Earth Planet. Sci. Lett.*, **516**, 56–65.

Mukhopadhyay, B., **Mukherjee, P.K.**, **Bhattacharya, D.** and **Sengupta, S.** (2005) Delineation of arsenic-contaminated zones in Bengal Delta, India: a geographic information system and fractal approach. *Environmental Geology 2005 49:7*, **49**, 1009–1020.

Murti, M.A., **Junior, R.**, **Ahmed, A.N.** and **Elshafie, A.** (2022) Earthquake multi-classification detection based velocity and displacement data filtering using machine learning algorithms. *Scientific Reports 2022 12:1*, **12**, 1–12.

Nason, J.D., **Hamrick, J.L.** and **Fleming, T.H.** (2002) Historical vicariance and postglacial colonization effects on the evolution of genetic structure in Lophocereus, a Sonoran Desert columnar cactus. *Evolution (N. Y).*, **56**, 2214–2226.

Nathan, Y., **Chua, S.**, **Chong, A.**, **Chan, N.**, **Morgan, K.**, **Switzer, A.D.**, **Friess, D.A.** and **Horton, B.P.** (2025) Rapid mangrove sediment accretion in late-Holocene paleochannels of Singapore. *Holocene*, **35**, 259–270.

Niculescu-Mizil, A. and **Caruana, R.** (2005) Predicting good probabilities with supervised learning. In: *Proceedings of the 22nd international conference on Machine learning - ICML '05*, *ACM Press*, New York, New York, USA, 625–632.

Olariu, C., **Steel, R.J.**, **Dalrymple, R.W.** and **Gingras, M.K.** (2012) Tidal dunes versus tidal bars: The sedimentological and architectural characteristics of compound dunes in a tidal seaway, the lower Baronia Sandstone (Lower Eocene), Ager Basin, Spain. *Sediment. Geol.*, **279**, 134–155.

Ono, K., **Plink-Björklund, P.**, **Eggenhuisen, J.T.** and **Cartigny, M.J.B.** (2021) Froude supercritical flow processes and sedimentary structures: New insights from experiments with a wide range of grain sizes. *Sedimentology*, **68**, 1328–1357.

Ortlieb, L. (1991) Quaternary shorelines along the northeastern Gulf of California, geochronological data and neotectonic implications. *Geological Society of America. Special Paper*, **254**, 95–120.

Oskin, M. and **Stock, J.** (2003) Pacific – North America plate motion and opening of the Upper Delfı ´ n basin , northern Gulf of California , Mexico. 1173–1190.

Oswood, M.W., **Everett, K.R.** and **Schell, D.M.** (1989) Some physical and chemical characteristics of an arctic beaded stream. *Ecography*, **12**, 290–295.

Otvos, E.G. (2005) Numerical chronology of Pleistocene coastal plain and valley development; extensive aggradation during glacial low sea-levels. *Quaternary International*, **135**, 91–113.

Pallares, C., **Maury, R.C.**, **Bellon, H.**, **Royer, J.**, **Calmus, T.**, **Aguillón-Robles, A.**, **Cotten, J.**, **Benoit, M.**, **Michaud, F.** and **Bourgois, J.** (2007) Slab-tearing following ridge-trench collision: Evidence from Miocene volcanism in Baja California, México. *Journal of Volcanology and Geothermal Research*, **161**, 95–117.

Parikh, H., **Patel, S.** and **Patel, V.** (2020) Classification of SAR and PolSAR images using deep learning: a review. *Int. J. Image Data Fusion*, **11**, 1–32.

Pausata, F.S.R., **Gaetani, M.**, **Messori, G.**, **Berg, A.**, **Maia de Souza, D.**, **Sage, R.F.** and **deMenocal, P.B.** (2020) The Greening of the Sahara: Past Changes and Future Implications. *One Earth*, **2**, 235–250.

Pedregosa, F., **Varoquaux, G.**, **Gramfort, A.**, **Michel, V.**, **Thirion, B.**, **Grisel, O.**, **Blondel, M.**, **Prettenhofer, P.**, **Weiss, R.** and **Dubourg, V.** (2011) Scikit-learn: Machine learning in Python. *the Journal of machine Learning research*, **12**, 2825–2830.

Peñuelas, J., **Filella, I.**, **Zhang, X.**, **Llorens, L.**, **Ogaya, R.**, **Lloret, F.**, **Comas, P.**, **Estiarte, M.** and **Terradas, J.** (2004) Complex spatiotemporal phenological shifts as a response to rainfall changes. *New Phytologist*, **161**, 837–846.

Riddle, B.R., **Hafner, D.J.**, **Alexander, L.F.** and **Jaeger, J.R.** (2000) Cryptic vicariance in the historical assembly of a Baja California Peninsular Desert biota. *Proceedings of the National Academy of Sciences*, **97**, 14438–14443.

Rockwell, T.K., **Masana, E.**, **Sharp, W.D.**, **Štěpančíková, P.**, **Ferrater, M.** and **Mertz-Kraus, R.** (2019) Late Quaternary slip rates for the southern Elsinore fault in the Coyote Mountains, southern California from analysis of alluvial fan landforms and clast provenance, soils, and U-series ages of pedogenic carbonate. *Geomorphology*, **326**, 68–89.

Rohling, E.J., **Foster, G.L.**, **Grant, K.M.**, **Marino, G.**, **Roberts, A.P.**, **Tamisiea, M.E.** and **Williams, F.** (2014) Sea-level and deep-sea-temperature variability over the past 5.3 million years. *Nature 2014 508:7497*, **508**, 477–482.

Saucier, R.T. (1994) Geomorphology and Quaternary geologic history of the lower Mississippi Valley.

Sawlan, M.G. (1991) Magmatic Evolution of the Gulf of California Rift. In: *The Gulf and Peninsular Province of the Californias*, *American Association of Petroleum Geologists*, 301–369.

Sawlan, M.G. and **Smith, J.G.** (1984) Petrologic characteristics, age and tectonic setting of Neogene volcanic rocks in northern Baja California Sur, Mexico.

Schmitt, A.K., **Stockli, D.F.** and **Hausback, B.P.** (2006) Eruption and magma crystallization ages of Las Tres Vírgenes (Baja California) constrained by combined 230Th/238U and (U–Th)/He dating of zircon. *Journal of Volcanology and Geothermal Research*, **158**, 281–295.

Schmitt, A.K., **Stockli, D.F.**, **Niedermann, S.**, **Lovera, O.M.** and **Hausback, B.P.** (2010) Eruption ages of Las Tres Vírgenes volcano (Baja California): a tale of two helium isotopes. *Quat. Geochronol.*, **5**, 503–511.

Schorr, M.R., **Hartke, S.**, **Pugh, A.**, **Camacho, D.**, **Navarrete, G.M.**, **Tjarks, D.**, **Martínez Gutiérrez, G.**, **Niemi, T.M.** and **Antinao, J.L.** (2018) Preliminary geochronology of uplifted marine and fluvial terraces in the Santa Rosalia Basin, central Baja California, Mexico. In: *Geological Society of America Abstracts*, 50, 319319.

Shakun, J.D., **Lea, D.W.**, **Lisiecki, L.E.** and **Raymo, M.E.** (2015) An 800-kyr record of global surface ocean δ18O and implications for ice volume-temperature coupling. *Earth Planet. Sci. Lett.*, **426**, 58–68.

Shim, D., **Ko, J.H.**, **Kim, W.C.**, **Wang, Q.**, **Keathley, D.E.** and **Han, K.H.** (2014) A molecular framework for seasonal growth-dormancy regulation in perennial plants. *Hortic. Res.*, **1**, 1.

Singh, I.B. (1996) Geological Evolution of Ganga Plain - An Overview. *Journal of the Palaeontological Society of India*, **41**, 99–137.

Singh, L.P., **Parkash, B.** and **Singhvi, A.K.** (1998) Evolution of the Lower Gangetic Plain landforms and soils in West Bengal, India. *Catena (Amst).*, **33**, 75–104.

Slootman, A., **De Boer, P.L.**, **Cartigny, M.J.B.**, **Samankassou, E.** and **Moscariello, A.** (2019) Evolution of a carbonate delta generated by gateway-funnelling of episodic currents. *Sedimentology*, **66**, 1302–1340.

Slootman, A., **Ventra, D.**, **Cartigny, M.**, **Normandeau, A.** and **Hubbard, S.** (2021) Supercritical-flow processes and depositional products: Introduction to thematic issue. *Sedimentology*, **68**, 1289–1296.

Smith, J.J., **Hasiotis, S.T.**, **Kraus, M.J.** and **Woody, D.T.** (2008a) Naktodemasis bowni: New ichnogenus and ichnospecies for adhesive meniscate burrows (AMB), and paleoenvironmental implications, Paleogene Willwood Formation, Bighorn Basin, Wyoming. *J. Paleontol.*, **82**, 267–278.

Smith, J.J., **Hasiotis, S.T.**, **Woody, D.T.** and **Kraus, M.J.** (2008b) Paleoclimatic Implications of Crayfish-Mediated Prismatic Structures in Paleosols of the Paleogene Willwood Formation, Bighorn Basin, Wyoming, U.S.A. *Journal of Sedimentary Research*, **78**, 323–334.

Smith, J.J., **Platt, B.F.**, **Ludvigson, G.A.** and **Thomasson, J.R.** (2011) Ant-nest ichnofossils in honeycomb calcretes, Neogene Ogallala Formation, High Plains region of western Kansas, U.S.A. *Palaeogeogr. Palaeoclimatol. Palaeoecol.*, **308**, 383–394.

Smith, R.M.H. (1990) Alluvial Paleosols and pedofacies sequences in the Permian Lower Beaufort of the southwestern Karoo Basin, South Africa. *Journal of Sedimentary Research*, **60**, 258–276.

Soil Survey Staff (1999) Soil taxonomy: A basic system of soil classification for making and interpreting soil surveys. *Agriculture handbook*, **436**, 336–337.

Sosdian, S. and **Rosenthal, Y.** (2009) Deep-Sea Temperature and Ice Volume Changes Across the Pliocene-Pleistocene Climate Transitions. *Science (1979).*, **325**, 306–310.

Spratt, R.M. and **Lisiecki, L.E.** (2016) A Late Pleistocene sea level stack. *Climate of the Past*, **12**, 1079–1092.

Steel, R.J., **Plink-Bjorklund, P.** and **Aschoff, J.** (2010) Tidal deposits of the Campanian Western Interior Seaway, Wyoming, Utah and Colorado, USA. In: *Principles of Tidal Sedimentology*, *Springer Netherlands*, 437–471.

Stock, J.M. and **Hodges, V.K.** (1989) America was partitioned into separate regimes of strike-slip. *Tectonics*, **8**, 99–115.

Stroud, M., **Allen, G.**, **Minear, J.T.**, **Cisneros, J.** and **Smith, L.** (2025) SWOT Satellite: A New Tool for Fluvial Geomorphology. *GSA Today*, **35**, 4–9.

Sylvester, Z., **Durkin, P.** and **Covault, J.A.** (2019) High curvatures drive river meandering. *Geology*, **47**, 263–266.

Tambroni, N., **Luchi, R.** and **Seminara, G.** (2017) Can tide dominance be inferred from the point bar pattern of tidal meandering channels? *J. Geophys. Res. Earth Surf.*, **122**, 492–512.

Tandon, S., **Sinha, R.**, **Gibling, M.** and **Dasgupta, A.** (2008) Late Quaternary Evolution of the Ganga Plains: Myths and Misconceptions, Recent Developments and Future Directions. *Golden Jubilee Memoir of the Geological Society of India*, **66**, 259–99.

Taylor, J.R. (1982) An introduction to error analysis: the study of uncertainties in physical measurements. *Univ. Science Books*, Mill Valley, California, 270 pp.

Tena, A., **Piégay, H.**, **Seignemartin, G.**, **Barra, A.**, **Berger, J.F.**, **Mourier, B.** and **Winiarski, T.** (2020) Cumulative effects of channel correction and regulation on floodplain terrestrialisation patterns and connectivity. *Geomorphology*, **354**, 107034.

Thomassen, H.A., **Freedman, A.H.**, **Brown, D.M.**, **Buermann, W.** and **Jacobs, D.K.** (2013) Regional Differences in Seasonal Timing of Rainfall Discriminate between Genetically Distinct East African Giraffe Taxa. *PLoS One*, **8**, e77191.

Umhoefer, P.J., **Darin, M.H.**, **Bennett, S.E.K.**, **Skinner, L.A.**, **Dorsey, R.J.** and **Oskin, M.E.** (2018) Breaching of strike-slip faults and successive flooding of pull-apart basins to form the Gulf of California seaway from ca. 8–6 Ma. *Geology*, **46**, 695–698.

Umhoefer, P.J., **Dorsey, R.J.**, **Willsey, S.**, **Mayer, L.** and **Renne, P.** (2001) Stratigraphy and geochronology of the Comondú Group near Loreto, Baja California sur, Mexico. *Sediment. Geol.*, **144**, 125–147.

Upton, D.E. and **Murphy, R.W.** (1997) Phylogeny of the Side-Blotched Lizards (Phrynosomatidae:Uta) Based on mtDNA Sequences: Support for a Midpeninsular Seaway in Baja California. *Mol. Phylogenet. Evol.*, **8**, 104–113.

Vaidyanadhan, R. and **Ramakrishnan, M.** (2010) Geology of India. *Geological Society of India Bangalore*, 557–994 pp.

Valdivia-Carrillo, T., **García-De León, F.J.**, **Blázquez, M.C.**, **Gutiérrez-Flores, C.** and **Zamorano, P.G.** (2017) Phylogeography and Ecological Niche Modeling of the Desert Iguana (Dipsosaurus dorsalis, Baird & Girard 1852) in the Baja California Peninsula. *Journal of Heredity*, **108**, 640–649.

Vaucher, R., **Pittet, B.**, **Humbert, T.** and **Ferry, S.** (2017) Large-scale bedforms induced by supercritical flows and wave–wave interference in the intertidal zone (Cap Ferret, France). *Geo-Marine Letters 2017 38:3*, **38**, 287–305.

Vayssière, A., **Castanet, C.**, **Gautier, E.**, **Virmoux, C.**, **Dépret, T.**, **Gandouin, E.**, **Develle, A.L.**, **Mokadem, F.**, **Saulnier-Copard, S.**, **Sabatier, P.** and **Carcaud, N.** (2020) Readjustments of a sinuous river during the last 6000 years in northwestern Europe (Cher River, France): from an active meandering river to a stable river course under human forcing. *Geomorphology*, **370**, 107395.

Vermeulen, B., **Hoitink, A.J.F.**, **Zolezzi, G.**, **Abad, J.D.** and **Aalto, R.** (2016) Multiscale structure of meanders. *Geophys. Res. Lett.*, **43**, 3288–3297.

Wang, G., **Wu, X.** and **Zhang, W.** (2025) cigChannel: a large-scale 3D seismic dataset with labeled paleochannels for advancing deep learning in seismic interpretation. *Earth Syst. Sci. Data*, **17**, 3447–3471.

Wang, W., **Xue, C.**, **Zhao, J.**, **Yuan, C.** and **Tang, J.** (2024) Machine learning-based field geological mapping: A new exploration of geological survey data acquisition strategy. *Ore Geol. Rev.*, **166**, 105959.

Wilder, B.T., **Betancourt, J.L.**, **Epps, C.W.**, **Crowhurst, R.S.**, **Mead, J.I.** and **Ezcurra, E.** (2014) Local Extinction and Unintentional Rewilding of Bighorn Sheep (Ovis canadensis) on a Desert Island. *PLoS One*, **9**, e91358.

Wood, D.A., **Fisher, R.N.** and **Reeder, T.W.** (2008) Novel patterns of historical isolation, dispersal, and secondary contact across Baja California in the Rosy Boa (Lichanura trivirgata). *Mol. Phylogenet. Evol.*, **46**, 484–502.

Wood, T.G. (1988) Termites and the soil environment. *Biol. Fertil. Soils*, **6**, 228–236.

Woodroffe, C.D., **Rogers, K.**, **McKee, K.L.**, **Lovelock, C.E.**, **Mendelssohn, I.A.** and **Saintilan, N.** (2016) Mangrove Sedimentation and Response to Relative Sea-Level Rise. *Ann. Rev. Mar. Sci.*, **8**, 243–266.

Wu, X., **Wang, H.**, **Bi, N.**, **Nittrouer, J.A.**, **Xu, J.**, **Cong, S.**, **Carlson, B.**, **Lu, T.** and **Li, Z.** (2020) Evolution of a tide-dominated abandoned channel: A case of the abandoned Qingshuigou course, Yellow River. *Mar. Geol.*, **422**, 106116.

Wynn, D.W. (1977) Narrandera 1:250 000 Geological Sheet SI/55-10. Sidney.

York, D. (1968) Least squares fitting of a straight line with correlated errors. *Earth Planet. Sci. Lett.*, **5**, 320–324.